Ratio of Pion-Kaon Production in Proton Carbon Interactions

A thesis presented

by

Andrey V Lebedev

to

The Department of Physics

in partial fulfillment of the requirements

for the degree of

Doctor of Philosophy

in the subject of

Physics

Harvard University

Cambridge, Massachusetts

May 2007

©2007 - Andrey V Lebedev

All rights reserved.

Thesis advisor
Gary Feldman

Author
Andrey V Lebedev

Ratio of Pion-Kaon Production in Proton Carbon Interactions

Abstract

The ratio of pion-kaon production by 120 GeV/c protons incident on carbon target is presented. The data was recorded with the Main Injector Particle Production experiment at Fermi National Accelerator Facility. Production ratios of K^+/π^+, K^-/π^-, K^-/K^+, and π^-/π^+ are measured in 24 bins in longitudinal momentum from 20 to 90 GeV/c and transverse momentum up to 2 GeV/c . The measurement is compared to existing data sets, particle production Monte Carlo results from FLUKA-06, and parametrization of proton-beryllium data at 450 GeV/c .

Contents

Title Page i
Abstract iii
Table of Contents iv
List of Figures viii
List of Tables xi
Acknowledgments xii
Dedication xiii

1 Introduction **1**

2 MIPP Detectors **5**
2.1 Tracking 5
2.1.1 Drift Chambers 8
2.1.2 Proportional Chambers 8
2.1.3 Time Projection Chamber 8
2.2 Particle Identification 10
2.2.1 Beam Cherenkov 10
2.2.2 Threshold Cherenkov 11
2.2.3 Beam Time of Flight 11
2.2.4 Time of Flight Wall 13
2.2.5 Ring Imaging Cherenkov 13
2.2.6 Electromagnetic Calorimeter 15
2.2.7 Hadron Calorimeter 15
2.3 Analysis Magnets 18

3 MIPP Trigger **20**
3.1 Particle Identification 20
3.1.1 Momentum Above 20 GeV/c 20
3.1.2 5GeV/c Momentum 21
3.2 Beam Cherenkov Operation 21
3.3 Interaction Trigger 23
3.3.1 DC1 Trigger 24
3.3.2 Scintillator Interaction Trigger 24
3.4 End of Spill and Calibration Triggers 25

3.5 Veto Counter . . . 25
3.6 NuMI Trigger . . . 26

4 Data Acquisition System 28
4.1 VME and CAMAC Interfaces . . . 30
4.1.1 Linux on PowerPC . . . 30
4.1.2 Handling interrupts in the kernel . . . 31
4.1.3 CBD 8210 . . . 32
4.1.4 VME Interrupt Generator . . . 32
4.2 Online Software . . . 33
4.2.1 MippIo . . . 33
4.2.2 Run Control and Message Passing System . . . 33
4.2.3 Event Builder . . . 36
4.2.4 MIPP DAQ Daemon . . . 36
4.2.5 Detector Processes . . . 38
4.2.6 Database Logger . . . 38
4.2.7 Online Monitoring . . . 38
4.2.8 Software Release System . . . 38
4.3 Slow Controls . . . 39
4.3.1 iFix . . . 39
4.3.2 ACNET . . . 39
4.3.3 High Voltage . . . 40

5 Beamline 41
5.1 Accelerator . . . 41
5.2 Primary Beam . . . 43
5.3 Secondary Beam . . . 43
5.3.1 Optimizing Beam Quality . . . 44

6 Event Reconstruction 50
6.1 Track Fitting . . . 50
6.1.1 Straight Line Fitting . . . 50
6.1.2 Template Track Fitting . . . 52
6.1.3 Fail Safe Fitting . . . 53
6.2 Wire Chambers . . . 54
6.2.1 Wire Clusters . . . 54
6.2.2 Wire Crosses . . . 55
6.2.3 Track Segments . . . 56
6.2.4 Chamber Track Candidates . . . 57
6.3 Time Projection Chamber . . . 59
6.4 Global Tracking . . . 60
6.4.1 Refitting TPC tracks . . . 60
6.4.2 Cleaning up TPC Tracks . . . 61
6.4.3 Merging Tracks . . . 61
6.4.4 Matching TPC Tracks to Chambers . . . 61

6.4.5 Tracks in the Event Stream . . . 62
6.5 Vertex Reconstruction . . . 63
6.5.1 Vertex Finding . . . 63
6.5.2 Vertex Constrained Fitting . . . 64
6.5.3 Fixing Track Momentum in Vertex Fit . . . 66
6.5.4 Limitations of Vertex Fitting . . . 67
6.6 Particle Identification . . . 68
6.6.1 Particle Identification Methods . . . 68
6.6.2 Fitting Ring Radius . . . 69
6.6.3 Choosing σ_{max} . . . 71
6.6.4 Incorrectly Fit Rings . . . 72
6.6.5 Corrections to Ring Radius . . . 73
6.6.6 Particle Identification from Ring Radius . . . 74

7 Detector Calibration and Alignment 78
7.1 Event Time . . . 78
7.2 Drift Chamber Time Offsets . . . 81
7.2.1 Event Selection . . . 83
7.2.2 Fitting . . . 84
7.3 Chamber Alignment . . . 84
7.3.1 Aligning Chamber Planes . . . 84
7.3.2 Z-alignment and Rotations . . . 86
7.4 Tuning Magnetic Field . . . 89
7.4.1 B_x/B_y Rotation . . . 89
7.4.2 B_y/B_z Rotation . . . 92
7.4.3 B_x/B_z Rotation . . . 93
7.5 TPC Electron Drift . . . 94
7.5.1 Measuring v_0 . . . 94
7.5.2 Distortion Corrections . . . 100
7.6 RICH R_0 . . . 102

8 Monte Carlo Simulation 104
8.1 Time Projection Chamber Digitization . . . 104
8.1.1 Generating Digits . . . 105
8.1.2 Generating Noise . . . 106
8.2 Wire Chamber Digitization . . . 106
8.3 RICH Hits and Digitis . . . 107

9 Data Analysis 108
9.1 Data Binning . . . 108
9.1.1 Geometric acceptance . . . 108
9.1.2 Bin Selection . . . 110
9.2 Pileup Removal . . . 111
9.3 Primary Vertex Selection . . . 114
9.4 Interaction Trigger Efficiency . . . 117

9.5 Particle ID Variable 117
9.6 Corrections from Monte Carlo Simulation 123
9.6.1 Need for Corrections 123
9.6.2 Background Modeling 123

10 Results **130**
10.1 Corrections and Errors 130
10.2 Production Ratios 134
10.3 Comparison to Existing Data 140
10.4 Discussion and Outlook 140

Bibliography **143**

List of Figures

1.1 Summary of hadronic production data available in 2001 2
1.2 Uncertainties in neutrino flux prediction 3
1.3 MINOS muon neutrino (left) and electron neutrino (right) fluxes and the fraction of neutrinos produced in kaon decays. 3

2.1 Schematic of the MIPP spectrometer 6
2.2 Schematic view of the TPC volume and pad plane 9
2.3 Schematic of T00 and T01 construction 12
2.4 Schematic of RICH electronics setup. 14
2.5 Electromagnetic calorimeter front view. 16
2.6 Hadron calorimeter front view 17
2.7 Projections of the JGG field map 18
2.8 Projections of the Rosie field map 19

3.1 Time of flight difference from $\beta = 1$ particle in T00 and T01 counters . . . 22
3.2 Summary of upstream beam Cherenkov pressure curves with nitrogen . . . 23
3.3 Trigger particle tag purity as measured by the RICH 24
3.4 NuMI trigger logic 26

4.1 Schematic of data acquisition setup 29

5.1 Schematic of the FNAL accelerator complex 42
5.2 Analysis of the initial beamline setup 45
5.3 Simulation of tracking of particles through initial beamline setup 46
5.4 Solution for reversed beamline setup 48
5.5 Simulation of tracking of particles using reversed-beam solution 49

6.1 Sketch of wire plane geometry. 51
6.2 Matching of DC123 and DC4/PWC56 segments in the center of Rosie . . . 58
6.3 Distribution of χ^2 per degree of freedom and number of clusters in chamber track candidates 58
6.4 Selection of tracks for `TMiniut` fitter and resulting track momenta 60
6.5 Matching of TPC tracks to chamber track candidates 62
6.6 Matching of tracks at the six chambers 63

6.7 Deterministic annealing filter weight functions for vertex finder 64
6.8 Number of z scans required for a vertex constrained fit 67
6.9 Vertex resolution in z 68
6.10 Mean RICH ring radii and RMS of light distribution 70
6.11 CO_2 refractive index and Hamamatsu PMT efficiency versus light wavelength 70
6.12 Effect of signal region on RICH ring fits 72
6.13 RICH ring shift from prediction 73
6.14 Ripples in RICH ring radius 74
6.15 Dependence of amplitude of RICH ring radius ripples 75
6.16 A 10% improvement in radius width of high momentum pions is obtained by removing ripple corrections through parametrized equations. 76
6.17 Distribution of fitted RICH ring radii and computed mass squared 77

7.1 Time of flight difference from $\beta = 1$ particle for a straight line particle from the target to time of flight wall. 79
7.2 Cable delay drift in T0 counters 80
7.3 Time slewing due to charge on the T0 PMT's 82
7.4 Comparison of time difference resolution with and without time slewing correction 83
7.5 Chamber residuals before alignment 85
7.6 Chamber residuals after alignment 86
7.7 DC123 z-alignment results 87
7.8 DC123 alignment results with corrected DC3 angle 88
7.9 Dependence of DC123 alignment constants on beam momentum 90
7.10 Dependence of DC4 and PWC56 alignment constants on beam momentum 91
7.11 B_x/B_z rotation using chambers 92
7.12 Ratios of B_x/B_y and B_z/B_y in the magnets 92
7.13 Alignment summary versus run with geometry and magnetic field corrections 93
7.14 Alignment summary versus beam momentm with geometry and magnetic field corrections 94
7.15 Dependence of TPC x-residual versus z slope on B_x/B_z rotation 95
7.16 B_x/B_z ratio in the magnets before and after correction 96
7.17 P10 drift velocity measurements 97
7.18 Measured TPC trigger time offset versus run number 98
7.19 Measured TPC drift velocity versus run number 99
7.20 Projections of 120 GeV/c track hits 101
7.21 Angle between the vertical and horizontal field component in the JGG . . . 101
7.22 RICH ring radius dependence on CO_2 density 103

9.1 RICH geometric acceptance 109
9.2 Shown are charged hadron fluxes with longtitudinal momentum above 20 GeV/c per incident proton as simulated by FLUKA-06 on 2% carbon target. 109

9.3 Expected number of π^+ events in the bins selected for the ratio measurement. Bin boundaries in p_z are 20, 24, 31, 42, 60, 90 GeV/c , and in p_T 0.2, 0.4, 0.6, 1 GeV/c . The largest p_T bin stretches to 2 GeV/c or 0.05 of the lower bin boundary, which corresponds to 50% geometric acceptance. 112
9.4 Momentum and dE/dx in the TPC of uninteracted protons 113
9.5 Distribution of variables that help distinguish pileup events from clean events. Solid yellow histograms are filled with information from single-track candidates, and red histograms from pileup candidate events.The histograms are scaled by the total number ($5.7 \cdot 10^5$) of proton tracks selected for the pileup study. 115
9.6 Shown on the left is fraction of events containing out of time secondary tracks in single proton candidate and pileup candidate events. On the right is distribution of times for the two classes of events. The peak at 0 ns corresponds to tracks that have no information from the drift chambers. . . 116
9.7 Effect of pileup clean up on TPC dE/dx and calorimeter energy 116
9.8 Vertex z of 2% carbon and target out data 117
9.9 Interaction trigger efficiency 118
9.10 Combined carbon, beryllium, and target out momentum spectrum enhancement under the assumptions of the most efficient and the most inefficient trigger. 119
9.11 Computed mass squared versus p_z in different p_t bins 120
9.12 Computed Monte Carlo mass squared versus p_z in different p_t bins 121
9.13 Data-Monte Carlo comparison of particle ID variable α for positives 124
9.14 Data – Monte Carlo comparison of particle ID variable α for negatives . . . 125
9.15 Monte Carlo signal and background in bin (0, 0) 126
9.16 Occupancy of positive pions and kaons in Monte Carlo 127
9.17 Occupancy of negative pions and kaons in Monte Carlo 128

10.1 Shown are ratios of reconstructed Monte Carlo ratios and true Monte Carlo ratios. The error bars come from propagation of statistical errors on the ratios, which are correlated between the reconstructed and true ratios. . . . 131
10.2 Effect on the ratios from poor knowledge of interaction trigger efficiency . . 132
10.3 Effect on the ratio from 5% change in target out scale factor 133
10.4 Systematic error from background subtraction 134
10.5 Measured ratios compared to particle production simulated with FLUKA-06 on 2% carbon target 135
10.6 Comparison to existing measurements 141
10.7 Comparison to existing measurements 142

List of Tables

2.1 Summary of multi-wire chamber parameters 7
2.2 Summary of chamber operation conditions 7

4.1 Message classes implemented in run control. 34

9.1 Coefficients for conversion from m^2 into particle ID variable α. 122

10.1 π^-/π^+ production ratio and errors 136
10.2 K^-/K^+ production ratio and errors 137
10.3 K^+/π^+ production ratio and errors 138
10.4 K^-/π^- production ratio and errors 139

Acknowledgments

Chapter 1

Introduction

Particle production is one of the classic phenomena studied by many experiments over the twentieth century. While many experiments focused on production of exotic particles, there were few high statistics measurements of inclusive production of pions, kaons, and protons. While some cross sections were measured with bubble chambers, most high statistics measurements were done with single arm spectrometers [1, 7, 16], and therefore cannot provide complete coverage of space in longitudinal and transverse momentum (see Figure 1.1. As a result, hadronic production models like MARS[30] and FLUKA[22, 23] have limited data to be tuned with, and in some cases give significantly different results.

Scarcity of hadronic production data affects every neutrino experiment[12, 29] since accelerator made and atmospheric neutrinos come from decay of pions and kaons produced in interactions of protons with matter. In the case of NuMI[1]/MINOS[2] experiment, 120 GeV/c protons are incident on carbon target which is two interaction lengths long. The uncertainties in particle production models largely cancel in comparison of the near and far detector data, but calculation of neutrino flux with various hadronic production models differ by up to 30% (Figure 1.2). degree, they do not cancel completely, so near/far detector comparison depends on the hadronic production model.

Recently, NA49 experiment at CERN published results of the measurement of charged pion production in proton-carbon collisions at 158 GeV/c [11], which is close to NuMI proton beam of 120 GeV/c . However, secondary and tertiary particle production in the NuMI target is significant, so if one is to tune Monte Carlo models to better predict

[1]Neutrinos at the Main Injector
[2]Main Injector Neutrino Oscillation Search

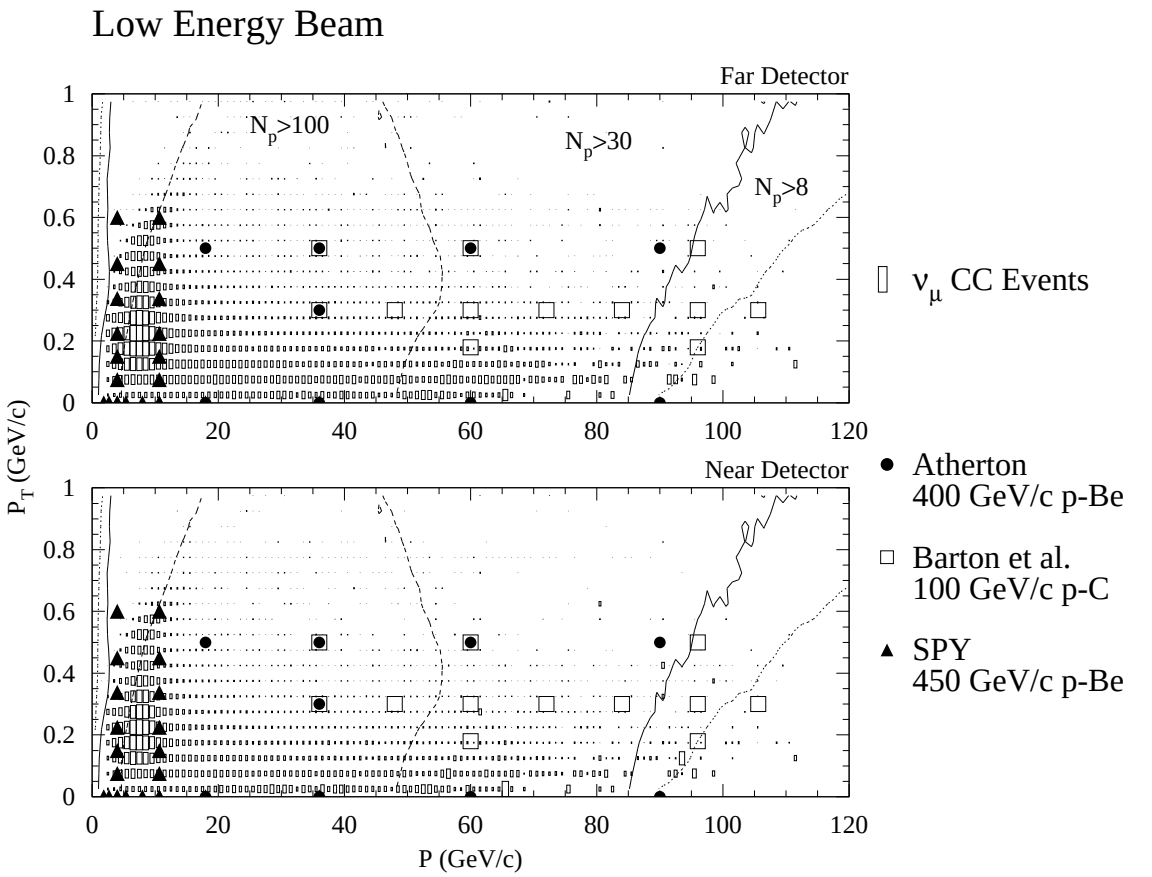

Figure 1.1: The plot from [21] shows the spectrum of pions which produce neutrinos in the MINOS far and near detectors. Superimposed are appropriately scaled data from single-arm spectrometers.

neutrino flux, it is essential to have data of hadronic production of pions, kaons, and protons on carbon at lower momenta. Moreover, large fraction of high energy neutrinos come from decay of charged kaons (see Figure 1.3), so knowledge of kaon flux is necessary as well.

The Main Injector Particle Production (MIPP) experiment was designed to measure total charged particle production of $\pi^{\pm}, K^{\pm}, p$, and $\bar{p}$ by tagged beam of pions, kaons, and protons on nuclear targets. Experiment is capable of selecting beam momentum from 5 to 85 GeV/c , or run with 120 GeV/c proton beam from the Main Injector at Fermilab. A time projection chamber (TPC) provides nearly complete coverage for forward-going particles, and multi-wire chambers allow measurement of momentum up to 120 GeV/c . Particle identification can be done for nearly all momenta of particles produced on the target using energy loss in the TPC, time of flight, threshold Cherenkov, and ring imaging Cherenkov

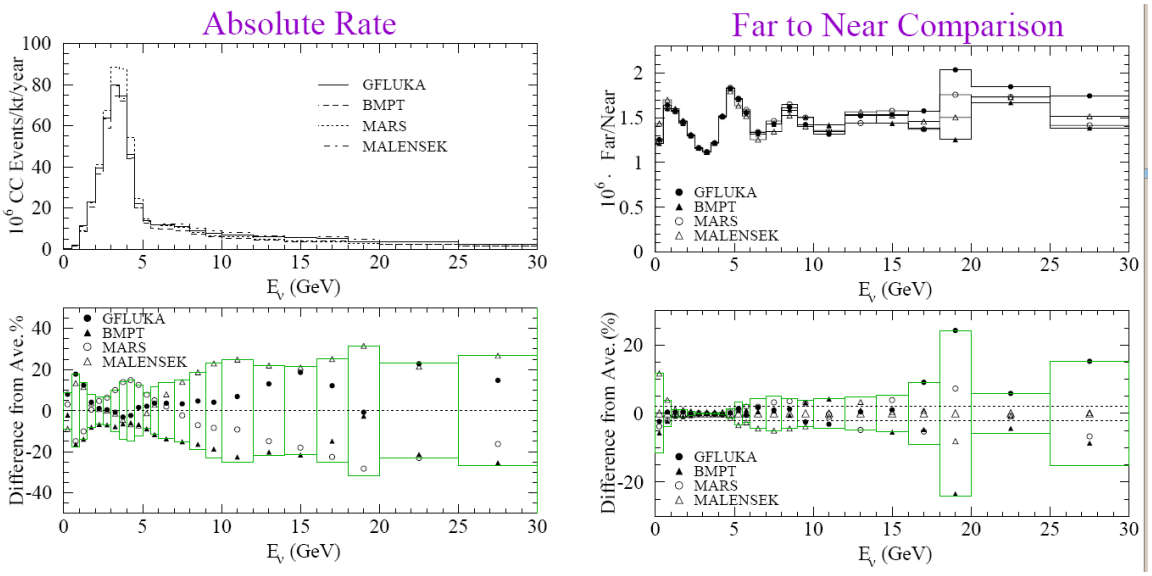

Figure 1.2: Uncertainties in neutrino flux calculation in NuMI beam. Since the MINOS near detector sees a line source of neutrino and far detector sees a point source, these uncertainties do not cancel for all momenta of interest, and having better understanding of hadronic production minimizes systematic error due to neutrino flux prediction.

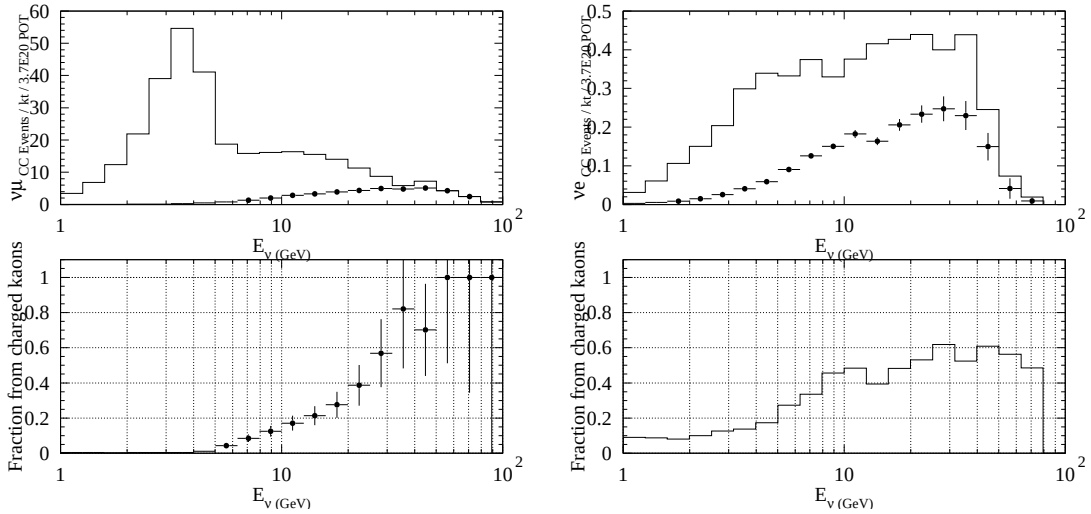

Figure 1.3: MINOS muon neutrino (left) and electron neutrino (right) fluxes and the fraction of neutrinos produced in kaon decays.

counters.

In addition to taking data on thin nuclear target, MIPP experiment directly measured particle production on a replica of NuMI target. Thus it is possible to cross check the understanding of NuMI hadron flux by comparing the spectrum from the actual target to the model of secondary production by using proton-carbon data at 120 GeV/c and hadron-carbon data at lower momenta. This improved understanding of hadronic flux will be welcome by the MINOS collaboration when in a few years systematic error from particle production will be comparable to the statistical error.

Measurement of the pion/kaon production ratio with $p_z > 20$ GeV/c presented here is the first step towards better understanding of NuMI hadron flux using MIPP data.

Chapter 2

MIPP Detectors

The MIPP spectrometer, shown in Figure 2.1 consists of a number of subsystems designed to provide tracking and identification of charged particles. Experimental target is located within a few centimeters of the front of the TPC. The chamber allows to reconstruct tracks in three dimensions and measure momentum of low momentum tracks. Two magnets, Jolly Green Giant (JGG) and Rosie, have vertical magnetic fields in opposite directions. The net effect of the two magnets is a transverse displacement of the track from the straight line in the xz-plane. Position measurement in the four drift chambers (DC) and two proportional wire chambers (PWC) make it possible to measure track momentum of high-momentum tracks. Charged particle identification is done by different detectors – TPC, time of flight wall (TOF), threshold Cherenkov (Ckov), and ring imaging Cherenkov (RICH) counters, depending on momentum of particles. Finally, electromagnetic and hadron calorimeters make it possible to identify electrons, gamma rays, and neutral particles. All subsystems are described in detail below.

2.1 Tracking

The spectrometer provides data to reconstruct incoming beam particle and secondary particles from interactions on the target. Three small drift chambers upstream of the target (BCs) are able to reconstruct the incident particle trajectory (track). TPC, four DCs, and two PWCs can reconstruct tracks coming out of an interaction. A summary of all wire chamber physical properties is given in Table 2.1 and operational conditions in Table 2.2.

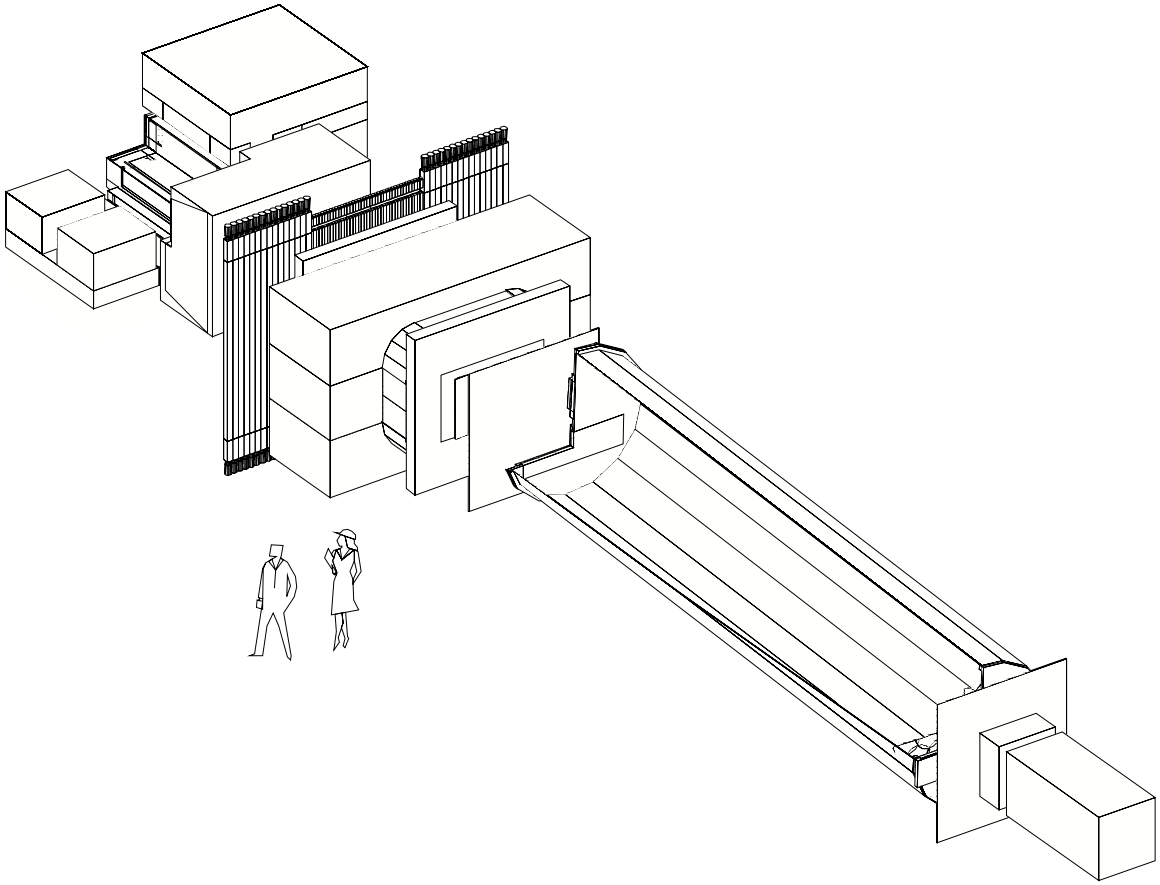

Figure 2.1: View of the MIPP spectrometer. From upper left-hand corner shown are TPC inside the JGG magnet, threshold Cherenkov, time of flight wall, Rosie magnet, DC4, PWC5, RICH, PWC6, electromagnetic calorimeter, and hadron calorimeter.

	Wire spacing (mm)	Active area (cm)	Number of wires	Wire orientation with respect to vertical	z in MIPP geometry (cm)
BC1	1.016	15.24×10.16	160	$\pm 21.60°$, $\pm 7.93°$	-4821.04
BC2	1.016	15.24×10.16	160	$\pm 21.60°$, $\pm 7.93°$	-2465.86
BC3	1.016	15.24×10.16	160	$\pm 21.60°$, $\pm 7.93°$	-1176.31
DC1	3.4925	182.88×121.92	512	$\pm 21.60°$, $\pm 7.93°$	-586.83
DC2	3.175	152.40×101.60	512 (448)	$\pm 21.60°$, $\pm 7.93°$	-427.99
DC3	3.175	152.40×101.60	512 (448)	$\pm 21.60°$, $\pm 7.93°$	-352.62
DC4	3.175	152.40×101.60	512 (448)	$\pm 21.60°$, $\pm 7.93°$	63.38
PWC5	3.000	200.00×200.00	640	$0°$, $90°$, $\pm 28.07°$	132.99
PWC6	3.000	200.00×200.00	640	$0°$, $90°$, $\pm 28.07°$	1415.92

Table 2.1: Summary of multi-wire chambers parameters. DC2-4 have 448 wires in the wide-angle planes and 512 in narrow-angle planes. Position along the beam axis is given in offline geometry coordinates. $z = 0$ is inside the Rosie volume, and the target is located at $z = -829\ cm$.

	Cathode voltage (kV)	Gas
Beam chambers	1.4	82 : 15 : 3 Ar/C_4H_{10}/methylal
Drift chambers	$1.85 - 2.05$	69 : 28 : 3 Ar/C_4H_{10}/methylal
Proportional chambers	3.0	76.5 : 8.5 : 15 $Ar/CH_4/CF_4$

Table 2.2: Summary of chamber operation conditions

2.1.1 Drift Chambers

BCs and DCs were used by FNAL E690 experiment and beam chambers are described in great detail in [13]. Beam chambers span a distance of 37 m and thus provide 150 μm resolution of position and 5 μrad resolution of angle of the incoming particle when multiple scattering is negligible. Moreover, 1 mm wire spacing allows to distinguish multiple particles and 1 μs range of the TDC allows one to measure the time of the track with respect to the trigger signal.

Chamber electronics consists of preamplifiers, Nevis discriminators, and LeCroy 4290 CAMAC TDC system to measure drift time with 1 ns resolution. LeCroy 4290 system consists of 32-channel TDC CAMAC modules, organized in a total of 15 CAMAC crates with 20-22 modules per crate. Each crate was read out by a dedicated CAMAC crate controller. When triggered, controllers zero suppress the data and send them out to a module located in a normal CAMAC crate.

2.1.2 Proportional Chambers

The two PWCs straddling the RICH counter were used in the NA24 experiment at CERN and later at the SELEX experiment at FNAL. Chamber construction is documented in detail in [9].

These chambers are readout with RMH electronics[28] designed at CERN in the 1970's. Preamplified signals from all 8 planes, were discriminated and latched during 500 ns gate in 8 crates, each filled with 20 32-channel cards. Zero-suppressed readout consisted of up to 4000 16-bit words indicating which channel of which module fired.

Unfortunately, only two of four planes in PWC5 could hold high voltage, which made the chamber less efficient and made it impossible to reduce combinatorial combinations of hit positions. However, these problems had a small effect on track reconstruction.

2.1.3 Time Projection Chamber

The TPC is the centerpiece of the MIPP spectrometer. With particle position measured at tens of points, the TPC is an excellent detector for pattern recognition of the entire event. The chamber was constructed in 1990 at the Lawrence Berkeley Laboratory BEVALAC facility for EOS experiment[3, 20, 14, 25, 31, 38, 15]. Prior to being used by MIPP, it served BNL E895 and E910 experiments.

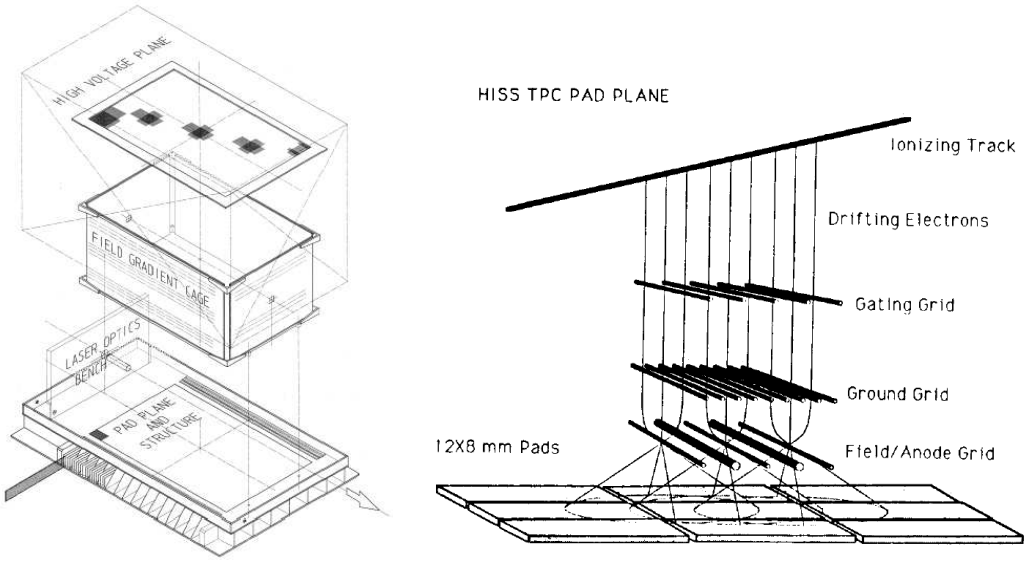

Figure 2.2: Schematic view of the TPC volume and pad plane with anode and ground wires, taken from [14].

Electrons ionized in the $96 \times 162 \times 81$ cm^3 gas volume by charged particles drift down in uniform vertical electric field of 125 V/cm. At the bottom of the drift volume (see Figure 2.2), in the region between ground and anode wires, an avalanche is created by strong electric field (> 3 kV/cm) near anode wires, achieving gas gain of 3000. The image charge on the pad plane 4 mm below the anode wires is recorded by the electronics.

The pad plane is divided into 128 padrows with 120 0.8×1.2 cm pads per row. Padrows record a slice ionization energy in z. Each pad is digitized by 12-bit flash ADC at 10 MHz. With drift velocity of ≈ 5 cm/μs, this gives 5 mm sampling along the vertical. A typical minimum ionizing track would leave signal on about 3 pads in a given row, with amplified signal spread over seven 100 ns time buckets. The large number of measurement points (up to 128 per track), yields sub-millimeter position resolution on the track position.

The TPC is readout through dedicated VME boards organized into four crates. Fiber optics links connected VME boards to pre-amplifier/shaper "sticks" located underneath the pad plane. A stick covers two half padrows.

2.2 Particle Identification

The spectrometer allows to identify the incident particle and secondary particles. Incident particles are identified using two differential Cherenkov counters (one for π/K and one for K/p separation). Secondary particles are identified by different detectors depending on their momentum. From low to high momentum the detectors are the TPC (< 1 GeV/c), the TOF wall (< 3 GeV/c), Ckov (< 17 GeV/c), and the RICH for particles with higher momenta.

2.2.1 Beam Cherenkov

Each beam Cherenkov counter consists of a long cylindrical radiator volume and a head at the downstream end. Radiator volume lengths are 22.9 m and 12.2 m so that statistically the same number of photo-electrons hit inner PMT's on both counters. The head contains a focusing mirror which reflects the light onto a photomultiplier tube (PMT) covered by a second mirror with a hole. The aperture of the hole is chosen in such a way that Cherenkov light emitted at angles below the cutoff would hit the PMT behind the second mirror (inner PMT) whereas light emitted at larger angles is reflected onto the outer PMT. The cutoff Cherenkov angles for the chambers were 5 and 7 mrad respectively.

Density in the upstream counter is set to achieve the kaon Cherenkov angle of 7 mrad – focusing its light onto the inner PMT. Pions with identical momentum radiate light at larger angle, missing the inner PMT and hitting the outer PMT. At the momenta of interest, protons do not radiate at all.

Similarly, the pressure in the downstream counter is set so that proton Cherenkov light hits the inner PMT, but not the outer PMT. The outer PMT collects light emitted at angles up to 30 mrad. This is important since for momenta below ≈ 31 GeV/c the pion Cherenkov angle is so large that the photons emitted by pions are no longer collected on the outer PMT. This property is independent of the gas that fills the radiator volume.

One of the challenges for identification of incident particle is the large span of momenta (5-90 GeV/c). The chambers are tuned to different beam momentum by establishing desired gas density in each counter. The cylinders can only be pressurized to ≈ 1.3 atm, therefore at low momentum (below 30 GeV/c) a heavy non-flammable gas has to be used in order to obtain a positive tag on protons and kaons. MIPP used C_4F_8O for this purpose. Nitrogen at different densities was used for all higher momenta. However, at 5 GeV/c even

the heavy gas is not dense enough for kaons or protons to radiate. But at that momentum we can take advantage of the measurable difference in time of flight of the three particle species between the front of the beamline and experimental target.

2.2.2 Threshold Cherenkov

The threshold Cherenkov consists of 96 toroidal mirrors at the downstream wall of the chamber filled with heavy gas. Each mirror is positioned to focus Cherenkov light onto one of the 96 PMT's positioned at the top and bottom of the chamber. The mirrors are positioned in such a way that each mirror reflects Cherenkov light onto one and only one PMT if the particle emanates from the target. In some instances, of course, light is shared by 2 or 3 mirrors, which can be taken into account once track trajectory is known. PMT windows are coated with wavelength shifter to make them sensitive to ultraviolet light. Charge off the PMTs is digitized with LeCroy 4300 ADC modules and discriminated signals are recorded with LeCroy 3377 multi-hit TDCs.

Historically, the chamber was operated with Freon, but due to modern environmental regulations, we had to use a much more expensive alternative C_4F_{10}. At atmospheric pressure, this gas has pion threshold at 2.6 GeV/c , kaon threshold at 8 GeV/c and proton threshold at 17 GeV/c .

2.2.3 Beam Time of Flight

Three scintillator counters are placed in the beamline: T01 about 3 m upstream of the target, TBD about 20 cm upstream of BC1, and T00 another 20 m upstream, almost immediately after the secondary beamline collimator. These detectors had to satisfy the following objectives:

1. Form a beam trigger signal,
2. Provide a reference start time for the TOF wall,
3. Resolve pileup,
4. Identify incoming beam particles at momentum of 5 GeV/c .

Each counter consists of a square piece of scintillator and four Hamamatsu R5900U PMT's, one on each side of the scintillator. Figure 2.3 shows schematic of the inside of the

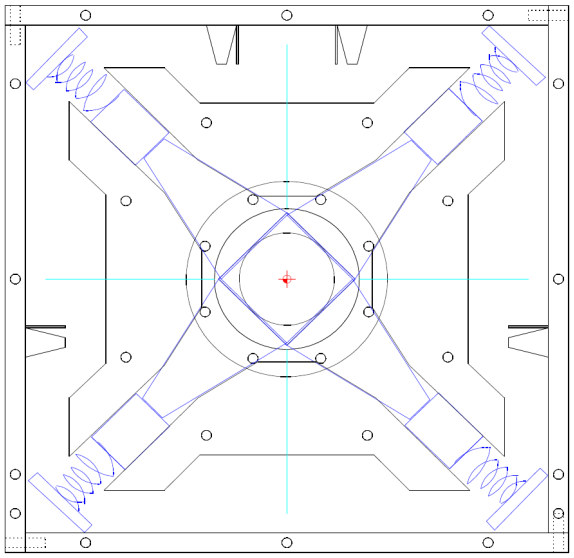

Figure 2.3: Schematic of T00 and T01 construction. Light from the scintillator is collected onto four PMT's by light guides. Phototubes are held in place by springs. TBD assembly is similar, except no light guides are used.

counters. The initial two counters T00 and T01 are equipped with light guides, which improve timing resolution. TBD counter, which was added at a later time to help form beam trigger does not have the light guides, as we were not planning on using it to measure time of flight of beam particles. In practice, degradation of timing resolution is dominated by delay cables, so resolution of TBD is comparable to T01 counter, and exceeded that of T00 counter. Resolution of TBD-T01 time difference for 120 GeV/c protons was 120 ps σ.

Each PMT signal is split with 90% of the charge to a discriminator and TDC, and 10% to an ADC. Knowing the amount of charge on a given PMT allowed for offline hit time correction.

Temporal coincidence of TBD and T01 3/4 signals is used to form a beam trigger. Further discussion of trigger formation can be found in Chapter 3.

Two sets of CAMAC TDCs measured PMT hit times with respect to experimental trigger time:

- LeCroy 3377 with 0.5 ns resolution and up to 16 hits in 512 ns window,
- LeCroy 2229 with 30 ns resolution, but only 1 hit in 60 ns window.

Thus, the first set of TDCs helps to determine presence of pileup (further help came from beam chambers), while the second set of TDCs was used to reconstruct particle flight time and reference time for the time of flight wall.

2.2.4 Time of Flight Wall

Conceptually the time of flight wall is straightforward: 54 3-m long vertical scintillator bars form a solid wall 3.5 m wide. The central 2 m are covered by 40 5×5 cm bars and the wings are covered by 10×10 cm bars. Both ends of each bar are capped with Winston cones to collect light onto Hamamatsu R5900U PMT's (identical tubes used in the beam counters).

Reference time of the incident particle is measured by beam counters (Section 2.2.3), and time of arrival of resulting particles is measured on both ends of each scintillator bar. The segmentation of the wall is such that the probability of two particles hitting the same bar is small.

2.2.5 Ring Imaging Cherenkov

Ring Imaging Cherenkov (RICH) was built for the SELEX experiment [17, 19, 18] in the 1990's. We filled the 10 m long radiator volume with carbon dioxide to a total pressure of ≈ 1.03 atm. In the course of the run, the volume was slowly leaking, so CO_2 was added on a weekly basis keeping the pressure constant within 1%. The level of oxygen contamination in the vessel was less than 1000 ppm.

Sixteen hexagonal spherical focusing mirrors mounted at the downstream end reflect Cherenkov light onto an array of 1 inch PMTs located on the upstream flange of the cylinder above the beam window. The mirrors cover an area of approximately 2×1 m. The average focal radius of mirrors is 19.8 m with RMS spread of less than 3 cm. Prior to the run, mirrors were aligned with laser so that their foci were at the center of the PMT array.

A holder plate supports the PMT's in a hexagonally close-packed array of 89×32 tubes. The plate separates the array from radiator volume with 2848 individually glued quartz windows and holds aluminized mylar cones for each phototube, thus essentially 100% of reflected Cherenkov light that reaches the front of the vessel gets to the phototubes.

Light is detected with two different types of phototubes:

- Hamamatsu R-760 with quartz windows and response down to 170 nm.

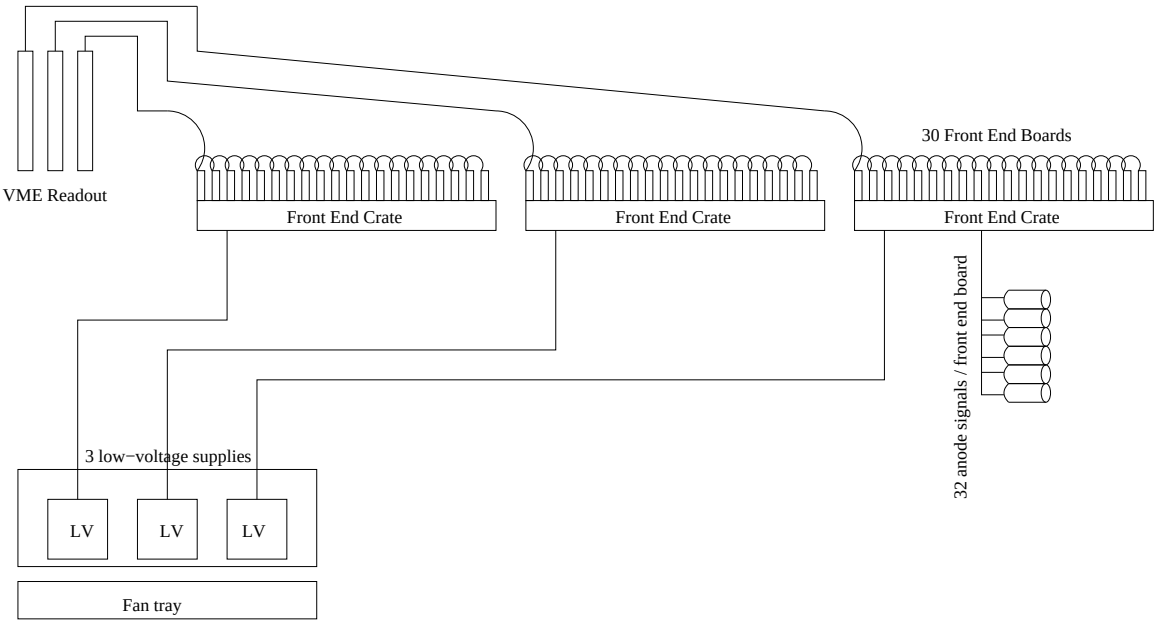

Figure 2.4: Schematic of RICH electronics setup.

- FEU-60 with glass window covered by wave-shifter so as to reach same wavelength range as Hamamatsu. These PMTs are about 42% as efficient, but they are 10 times as cheap.

Unfortunately, in March 2004 one of the FEU-60 PMT bases caught fire, resulting in 30% loss in the number of PMT's. Fortunately, this accident had a negligible impact on the PID capability of the device because of the high index of refraction of CO_2 – radius of $\beta = 1$ ring is 29.5 cm and typical number of hit tubes per ring is over 20.

All photomultiplier tubes are powered with 6 high voltage supplies, each capable of delivering 200 mA at 3 kV. 32 PMT's with similar nominal high voltage were grouped together, and a number of different voltages in steps of 20 V created with 6 Zener diode chains.

The signal is read out with custom electronics designed at FNAL, built and tested at Harvard University. The setup is shown schematically in Figure 2.4. 89 front-end cards are arranged into 3 crates (30, 30, and 29 cards), each crate controlled by one VME controller board.

Each of the 32 channels on front-end cards contains a differential amplifier with a gain of ≈ 20 and an analog comparator. The threshold is programmable for each channel

in steps of 0.8 mV. Discriminated signal is continuously pushed into a pipeline memory. When a controller board is triggered, the trigger is forwarded to front-end cards and the data that falls within the strobe gate is latched. RICH electronics can be strobed multiple times before a readout command must be issued, thus allowing for a multi-level experiment trigger. Pipeline delay is programmable for each front-end board and can be set as large as 128 clock ticks (2.4 μs with 53 MHz clock). Programmable delay facilitated adjusting the timing of PMT signals to the trigger. Since the instantaneous rate at MIPP was quite low, we latched the signal with a fairly wide strobe gate of 100 ns. The electronics is capable of using gates as short as two clock cycles.

2.2.6 Electromagnetic Calorimeter

The primary purpose of electromagnetic calorimeter is to measure the production of forward high energy photons. It consists of 10 planes of alternating horizontal and vertical wire planes sandwiched between 15 mm thick lead plates. Each active plane is comprised of eight 8 inch wide, 1 inch thick chambers with 8 wires per chamber. Front view of the system is shown in Figure 2.5.

Detector was readout with custom ADC CAMAC units built by the University of Michigan group. Because 1970's ADC chips were used, the calorimeter was the second slowest detector after TPC in terms of readout speed.

2.2.7 Hadron Calorimeter

Hadron calorimeter is the last detector on the experiment, located directly behind electromagnetic calorimeter. Its purpose is to measure the production of forward-going neutrons. It was previously used by the HyperCP experiment. The active volume consists of four scintillator plates sandwiched between lead sheets. It is meant to determine the energy of hadrons by summing energy deposition of the resulting hadronic shower initiated in the lead sheets that comprise the majority of the interaction lengths of the detector. Scintillator plates are segmented into two readout cells symmetric about the beam axis (with a total of eight cells). Each cell is read out by one photomultiplier tube. The calorimeter also serves as the experiment's beam dump

Calorimeter is readout through custom built electronics designed at the University of Virginia. PMT signal passes through ADC driver module and the amplified charge is

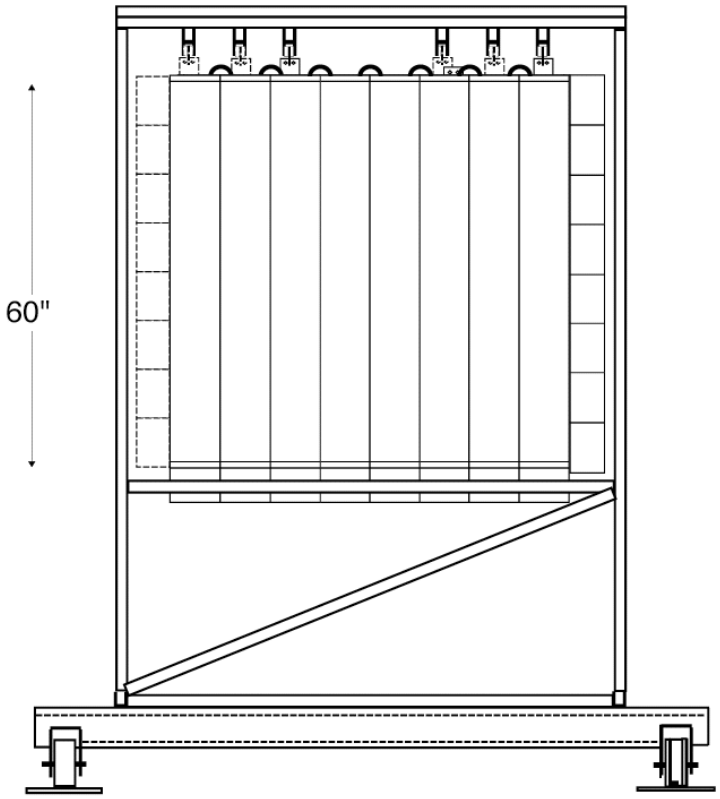

Figure 2.5: Electromagnetic calorimeter front view.

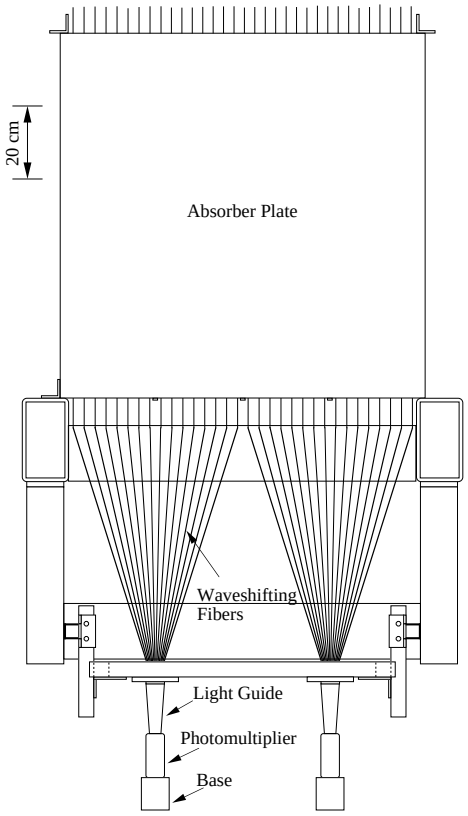

Figure 2.6: Schematic of hadron calorimeter front view. One can see the two cells, the light from each cell is collected onto its respective phototube.

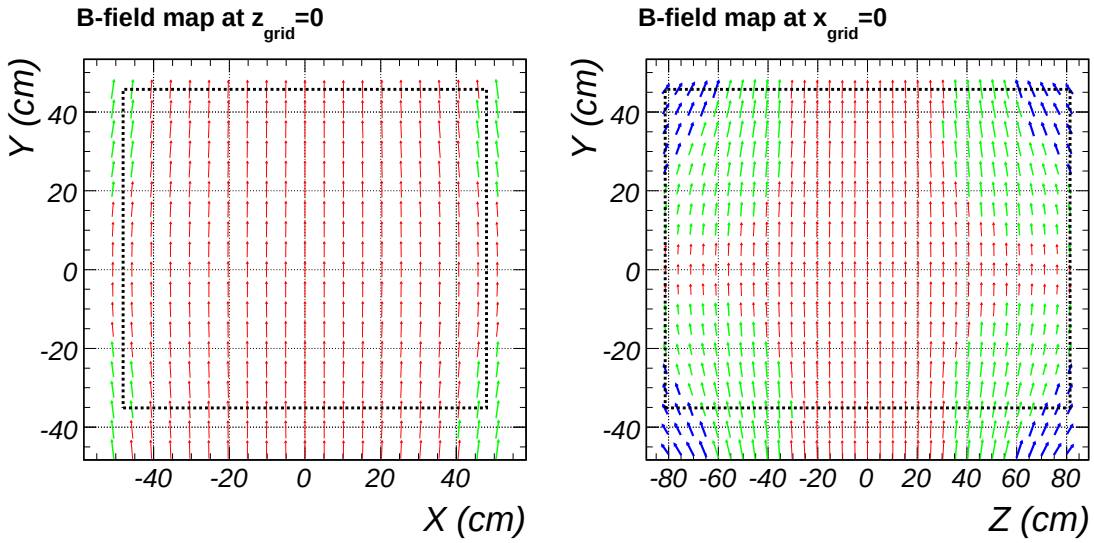

Figure 2.7: Projections of the JGG field map in slices along the center of the magnet. Regions of non-uniform field are highlighted with thicker green arrows where $B_i/B_y > 0.1$ and thickest blue arrows where $B_i/B_y > 0.5$. The dashed line shows the boundary of the TPC drift volume.

then digitized by a 16-bit CAMAC ADC. With pedestal widths of $2-3$ ADC counts, each cell has dynamic range of about 5000!

2.3 Analysis Magnets

MIPP used two magnets for momentum measurement: Jolly Green Giant and Rosie. For safety, magnetic fields were set so that kick angles were about equal and opposite ($\int B_y dl \approx 1$ Tm). This way regardless of momentum, beam was absorbed by the beam dump.

While the experimental hall was still empty, all three magnet field components were mapped onto 2-inch three dimensional grid using Ziptrack field measuring device. The device consists of three Hall probes, one for each component of the magnetic field. As the probe holder glides along the track, the field is sampled every 2 inches, with the three components sampled in the same point at slightly different times. Complete field maps are used to compute trajectories of particles in the non-uniform field and to compute trajectory of electron drift in the TPC.

The Jolly Green Giant magnet was originally built at Harvard in the 1960's. Its

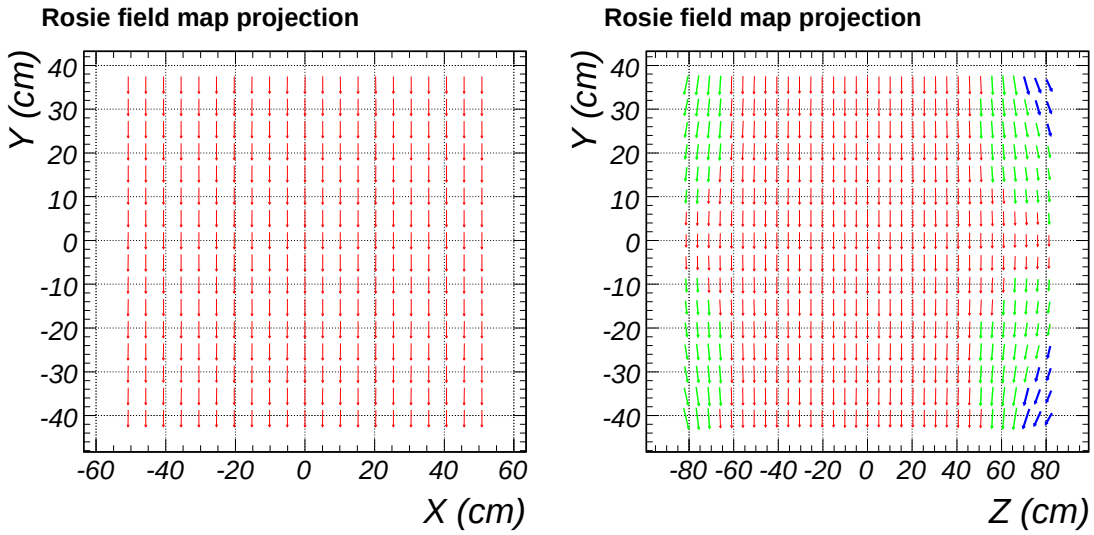

Figure 2.8: Projections of Rosie field map in the same volume as those in Figure 2.7, using the same color scheme for arrows.

aperture is sufficiently large for the TPC to fit, but its magnetic field is non-uniform towards the edges of the TPC drift volume, hence corrections of up to 7 cm in TPC hit positions have to be made. Rosie magnetic field is much more uniform, but unfortunately, its aperture is a few centimeters too small for the TPC to fit.

One of the coils in Jolly Green Giant was damaged and had been repaired prior to magnet being installed. In the course of the run, two coils shorted out, so the experiment ended up having 3 distinct field maps. Computer models of the magnetic field showed that the differences in field components due to different coil combination are small and could be neglected.

Chapter 3

MIPP Trigger

Experimental single-level trigger is fairly simple: the first stage of the trigger decides on the species of the particle and the second stage on whether or not the particle interacted in the target. Thus, 7 physics trigger bits are typically in use: untagged beam, three particle species, and three particle species with interaction. Different trigger bits are scaled down before a global OR is formed in order to achieve about 20% minimum bias and 80% interaction trigger mix. Unless prohibitively high scale down factors are required, the factors are chosen to record an even mix of protons, kaons, and pions.

Since the trigger has only one level and does not provide a fast clear, decision has to be made in the shortest time possible so as not to degrade the resolution of the TOF system. In the final implementation, the trigger is formed about 250 ns after the incident particle passes through the target.

3.1 Particle Identification

3.1.1 Momentum Above 20 GeV/c

As described in Section 2.2.1, at 20 GeV/c and above, the pressure in beam Cherenkov counters can be tuned so that all charged particles radiate light. The four PMTs are abbreviated as UI for upstream inner, UO for upstream outer, DI for downstream inner, and DO for downstream outer. Under these operating conditions, the particle trigger bits are defined as:

- $\pi : \overline{UI} \cdot UO$

- K: $UI \cdot \overline{UO}$
- p: $DI \cdot \overline{DO}$

At 35 GeV/c and above, pion and kaon Cherenkov angle in the downstream counter is below 30 mrad, so under those conditions, a more stringent trigger could be formed, based on all four PMTs:

- $\pi : \overline{UI} \cdot UO \cdot \overline{DI} \cdot DO$
- K: $UI \cdot \overline{UO} \cdot \overline{DI} \cdot DO$
- p: $\overline{UI} \cdot \overline{UO} \cdot DI \cdot \overline{DO}$

In the interest of saving trigger time, this momentum-dependent trigger was not implemented.

3.1.2 5GeV/c Momentum

Using beam Cherenkov counters, it is not possible to tag protons with momentum below about 20 GeV/c , and kaons cannot be tagged when momentum is below 11 GeV/c , as a sufficiently high gas density could not be obtained. Even if it were possible to do that, the gas density would be so large that multiple scattering in the counters would degrade the knowledge of position and direction of the incoming particle. Instead, at 5 GeV/c , we rely on particle time of flight to distinguish kaons and protons offline. Figure 3.1 shows that the task is easily achieved at such a low momentum.

For the purpose of the trigger, both beam Cherenkov densities were tuned to radiate on pions, muons, and electrons. Then proton plus kaon trigger was the absence of signal in all beam Cherenkov PMTs. Both negative and positive beams of this momentum are primarily ($\approx 90\%$) composed of pions, with similar fractions of proton and kaon, so it was acceptable to accumulate equal fractions of protons and kaons, as long as they could be distinguished offline.

3.2 Beam Cherenkov Operation

Pressure scans were done in order to find the optimal operating gas densities of the beam Cherenkov counters. A stand-alone executable read out latched discriminated

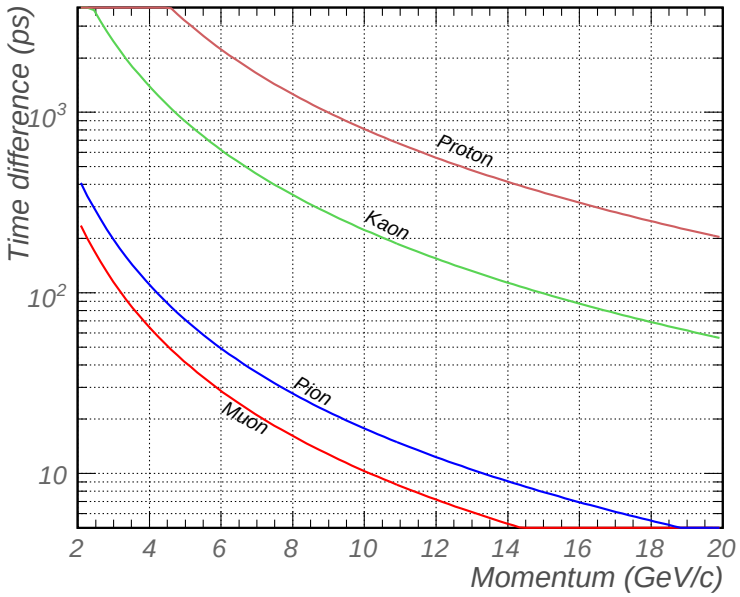

Figure 3.1: Time of flight difference from $\beta = 1$ particle for muons, pions, kaons, and protons between T00 and T01 counters. With time resolution of 200 ps, it is possible to do proton/kaon separation below 11 GeV/c , and kaon/pion separation below 6 GeV/c .

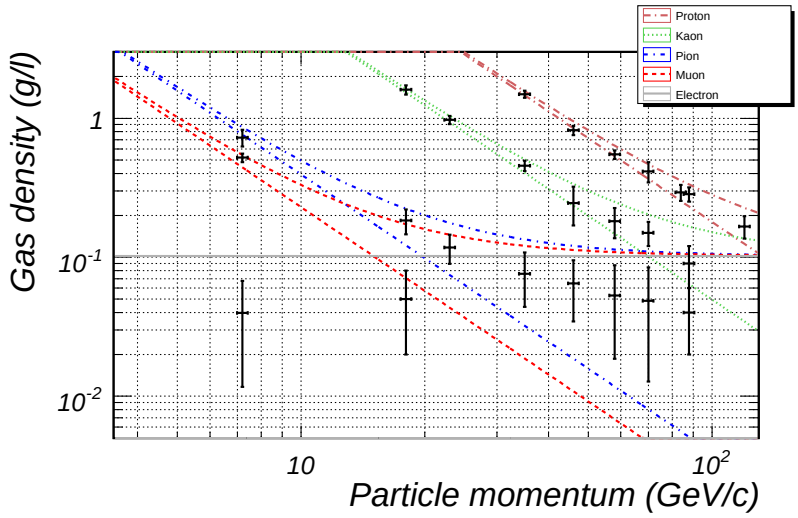

Figure 3.2: Summary of upstream beam Cherenkov pressure curves with nitrogen. The two curves for each particle species are threshold density and density at which Cherenkov angle is 5mrad. Superimposed data are centers of peaks of $UI \cdot \overline{UO}$ in pressure curves.

PMT signals at different pressures, recording 10000 triggers per pressure point. From the frequency of occurrence of different PMT combinations, one can find the peaks corresponding to different particle species. Figure 3.2 shows the summary of all pressure curve data in nitrogen.

For momenta 20 GeV/c and above, RICH rings can be used to measure trigger purity. In 20 GeV/c beam, we can identify protons by lack of signal, but at 35 GeV/c and above, all 3 particles radiate, so purity measurements shown in Figure 3.3 are more reliable. Still, in most cases, trigger purity is above 70%, and as one would expect, is above 99% for majority particle.

3.3 Interaction Trigger

Initial MIPP interaction trigger was based on multiplicity of DC1, requiring 2 or more wire clusters in at least three of the four planes. This trigger has the following problems associated with it:

a) Large chamber area made it highly susceptible to poor beam conditions,

b) Chamber is sometimes noisy because of low discriminator thresholds,

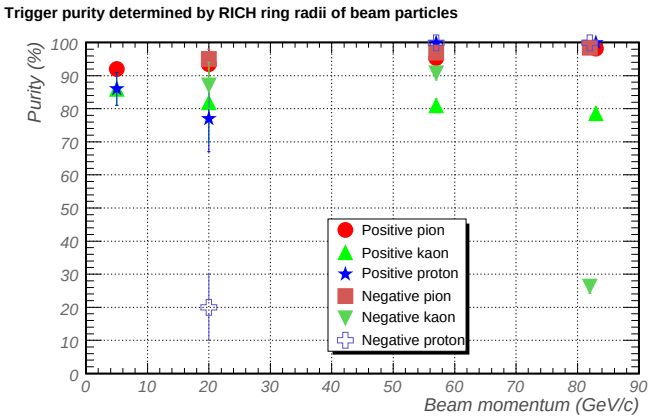

Figure 3.3: Trigger particle tag purity as measured by the RICH.

c) Small efficiency for two-particle final states where one particle is soft.

To address the problems of DC1 interaction trigger, a scintillator interaction trigger was built. Both triggers were used in order to measure systematic effects of each interaction trigger.

3.3.1 DC1 Trigger

Drift chamber preamplifier cards, each serving 8 wires, are mounted on the chamber. Four preamplifier cards are connected to one discriminator. Each discriminator output 32 ECL signals, one per wire, and 4 ECL OR signals, one for each cluster of 8 wires. The cluster OR signals are sent to majority logic units (LeCroy 4532 CAMAC module) to create a multiplicity interaction trigger, called iDC. The trigger fires if at least 2 different clusters fire in at least 3 out of 4 planes.

3.3.2 Scintillator Interaction Trigger

The scintillator interaction trigger (Scint)[5] is much simpler than the iDC. A 3.175 mm thick 5.40×7.62 cm piece of scintillator is placed ≈ 1.5 cm after the target. The scintillator has interaction length of 81.9 g/cm^2 and density of 1.032 g/cm^3, so its thickness is about 0.4% interaction length. Clear fibers collect light from the two shorter sides of the scintillator. The other ends of fibers are closely packed onto the face of Burle 83054H PMT.

By safety rules, in order to operate the trigger with hydrogen target, all high voltages (i.e. PMT) had to be at least 3 m away from the target, hence calling for rather long fibers. Even with 3 m of fiber, the counter gets about 73 photo-electrons per minimum ionizing particle (mip).

PMT charge is amplified with LeCroy 612 AM PMT amplifier module, creating two copies of the signal. One copy goes directly to an ADC, second copy goes to an analog splitter. The outputs of the splitter are discriminated with two different thresholds, creating `SciHi` (≈ 3 mip) and `SciLo` (≈ 1.5 mip) digital signals.

The problem with `SciLo` signal is that Landau tail of single-particle energy deposition dominates the count rate from 1% interaction length target. At the threshold level of `SciHi`, only $\approx$1% of single-particle states deposit enough energy to create the trigger signal, thus yielding trigger purity of $\approx$50%

3.4 End of Spill and Calibration Triggers

Each accelerator beam spill was followed by an end of spill trigger and a few pulser calibration triggers.

Upon receipt of end of spill trigger, detectors were not triggered, only the following actions were taken:

1. Scalers for the entire spill were read out and cleared;
2. A record was written to the database with the number of different triggers recorded in the spill;
3. Buffered data was transferred from PowerPCs to the DAQ server.

On calibration triggers, detectors were triggered by a pulse generator. These triggers were used to calculate pedestals and to identify hot channels.

3.5 Veto Counter

In order to limit the effect of beam halo coming from the primary target in secondary beam configuration, a 35 cm $\times$ 40 cm scintillator paddle with a 4.32 cm diameter hole is mounted on a plate of aluminum 140 cm upstream of the target. Two PMTs are

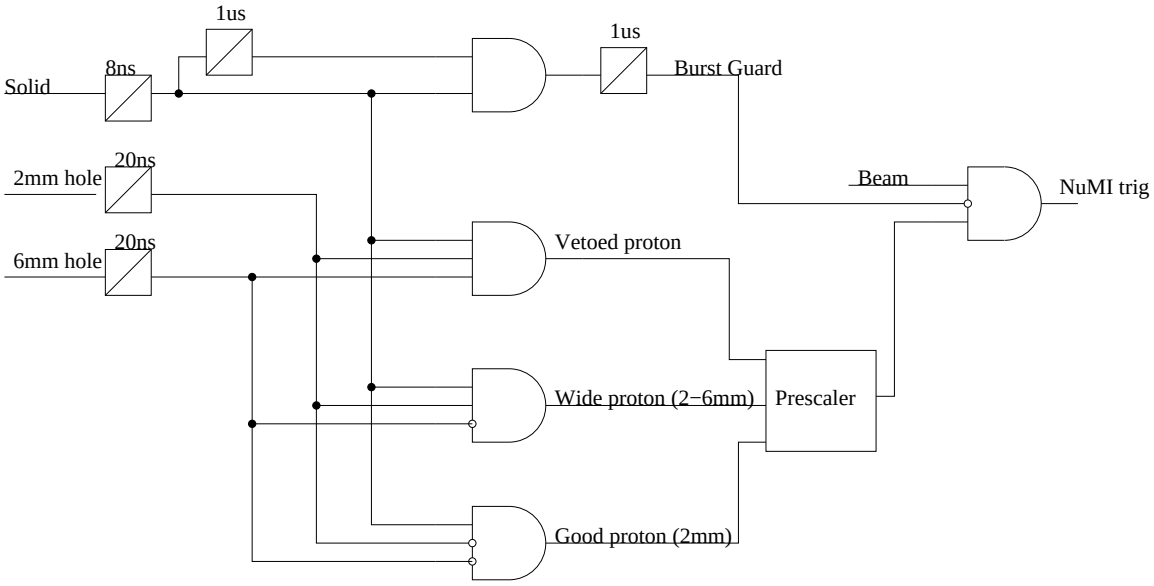

Figure 3.4: Logic for NuMI trigger. Trigger rate in each of 3 different regions could be scaled down, so that even with poorly tuned beam, we could ensure that most triggers were taken with protons on target.

attached to the sides of the veto scintillator through light guides, and the logical AND of the two PMTs formed an 80 ns veto signal to reject events with particles outside of the hole.

3.6 NuMI Trigger

When data was taken with the MINOS target, no interaction trigger was required since the target is 2 interaction lengths. However, the beam in MC7 was larger than the NuMI beam, so a dedicated trigger counter was built in order to make beam phase space at MIPP similar to NuMI beam. The counter consisted of three pieces of scintillator: solid, with 2 mm diameter hole in the center, and with 6 mm hole. The paddles with holes were used to veto particles that were too far from the beam center, thus ensuring that most data is taken under conditions resembling the NuMI proton beam. The logic for this trigger is shown in Figure 3.4

In addition to vetoing wide particles, the trigger had a 1 μs "burst guard" which prevented the trigger from firing if two protons were separated by less than 1 μs. Burst

guard was necessary in order to prevent pileup. Since almost all protons interact in the target with fairly large multiplicities, two events one on top of one another would be very hard to reconstruct in the TPC.

Chapter 4

Data Acquisition System

MIPP data acquisition system (DAQ) was designed for rather modest requirements. Trigger rate was limited to about 60 Hz due to the time it took to zero suppress TPC data. Around 90% of the data came from the size of the TPC event, 100 kB on average. Initial design specifications were to read out all of the detectors in a mode where beam was delivered in 1 s spills, 20 spills per minute, or 2 MB/s. MIPP DAQ was able to keep up with the data rate, which did not exceed fifteen 600 ms spills per minute (see Chapter 5).

Figure 4.1 shows the overall schematic of the data acquisition system. Computers which made the experiment work included

- DAQ server which had 2 network cards, was connected to the public net and to the private subnet.
- Six VME PowerPC's (PPC), connected to the DAQ server through 100 Mbit network were able to access VME and CAMAC readout electronics and send data to the server.
- Online monitoring machine enabled monitoring of data in real time.
- High Voltage machine was used to control and monitor all PMT and TPC high voltages (wire chamber high voltages were manually controlled).
- Database server which ran PostgreSQL database where all online information was stored.

This chapter describes all the online software that was running on all of these machines.

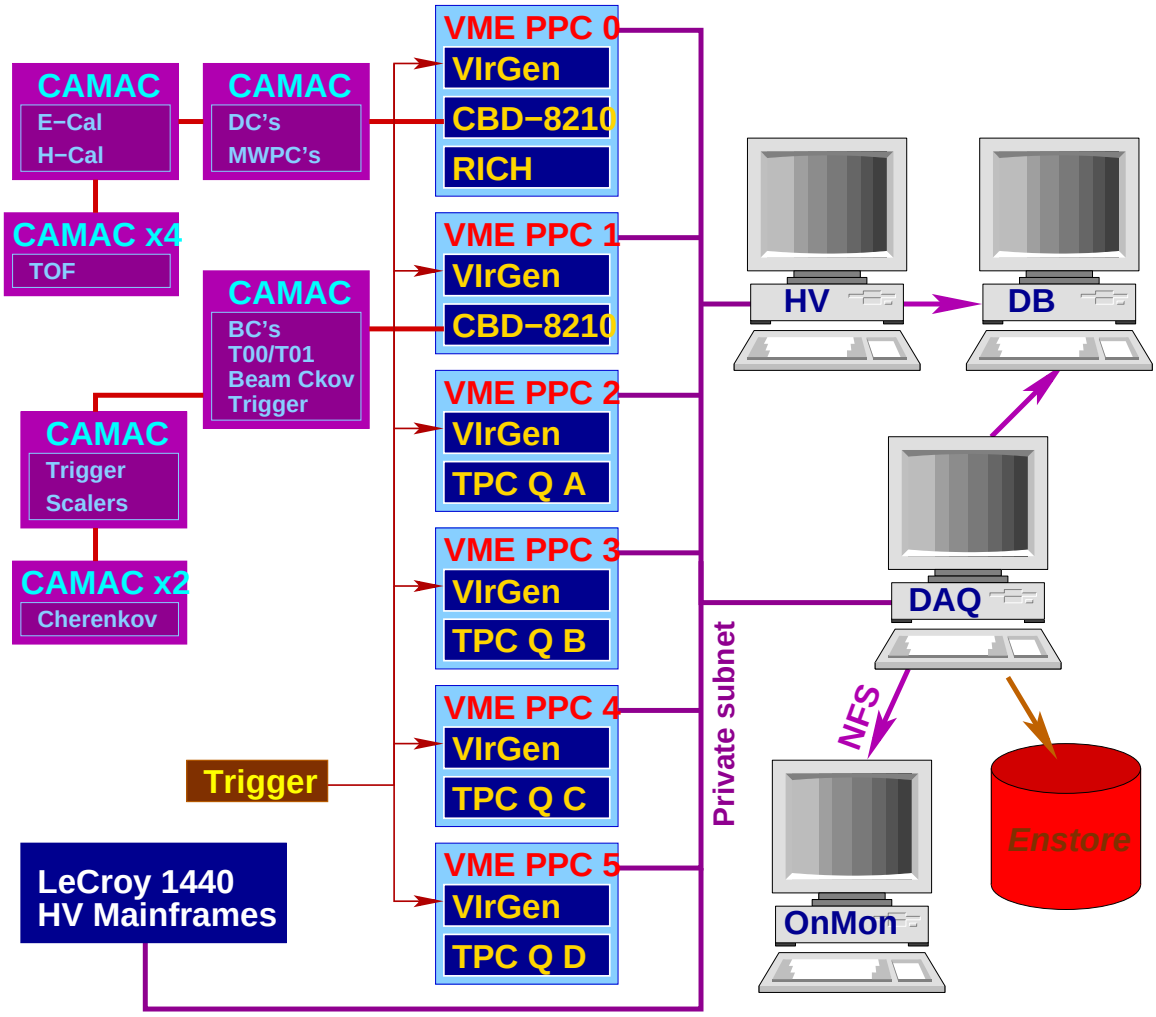

Figure 4.1: Schematic of data acquisition setup. Of the six VME PowerPCs, four were dedicated to control and read out of the TPC quadrants, and the other two read out the rest of the detectors, mainly CAMAC electronics. Readout processes were triggered through VME interrupts delivered by `VIrGen` boards. High voltage mainframes connected to private subnet as well, were controlled and monitored by HV machine. Detector data were written out to dedicated files, and online monitoring data were stored in PostgreSQL database. Online monitoring was done by exporting data disks through NFS. Finally, data were regularly shipped to FNAL robot tape storage (Enstore).

4.1 VME and CAMAC Interfaces

At the time when MIPP DAQ was designed, one of the most affordable ways to access VME bus was to run Linux on VME PowerPC's made by Motorola. MIPP required 6 MVME 2432 computers: 4 dedicated to TPC readout and 2 more to read out all other detectors. Those machines had 350 MHz processors and 256 MB of memory. They were placed into 6U VME crates so as to have direct access to the VME bus. On-board Tundra Universe II chip provided access to the VME bus. MIPP used a small subset of its capabilities for VME transactions: A24/D16, A16/D16, A32/D32 data transfers, and interrupt handling.

Most detectors were configured and readout through CAMAC electronics. Two CBD 8210 CAMAC branch drivers made by Creative Electronics Systems S.A. were used to drive two CAMAC branches with a total of 12 crates.

4.1.1 Linux on PowerPC

PowerPC's have two links to the outer world: 9600-baud debug port and 100-baseT ethernet connection. Having no hard drive, the computer had to be booted from a remote machine. The kernel, loaded through `tftp` protocol, would know the location of the file system mounted through NFS. On-board flash memory could be programmed to select the server and location of the kernel file on the server.

Linux kernel 2.2.12 and the file system based on glibc-2.2.5 was compiled from scratch using gcc-2.95.3. We inherited a file system compiled for kernel 2.1.24 with egcs. Since the compiler and kernel had significant changes and improvements, it was necessary to upgrade the operating system. I followed Linux From Scratch[24, 2] recipe to rebuild the file system.

At the time the file system was built, it seemed that having RedHat Package Manager (RPM) on the operating system would be necessary to facilitate system administration. However, since PowerPC's were on the private sub-net, security was not an issue, and system maintenance was much simpler than for computers exposed to the internet. The system had to be supported on 6 computers only, so most packages compiled from source were not re-installed or incorporated into RPM database.

Even though the number of packages is not nearly as large as on most modern operating systems, having to serve 6 systems from the DAQ server required a significant

amount of disk space. To reduce the total size of the systems, debugging symbols were stripped from executables and system libraries. Furthermore, unlike system binaries and libraries, one common `/usr/share` directory was exported to the PPC's and MIPP online software resided in `/usr/local`, common to all 6 computers.

4.1.2 Handling interrupts in the kernel

Kernel module to drive Tundra II chip written by Gabriel Paubert could handle I/O, but could not deliver interrupts into user space. In order to simplify debugging, we wanted to write all online software in user space. Performance loss due to this inefficiency could be tolerated because TPC electronics rather than VME readout was the bottleneck. In order to deliver interrupt into user space, a modification to the module was necessary.

Final design was implemented using semaphores. User's program would increment the value of the semaphore, release `VIrGen` busy (see Section 4.1.4), and then block until the semaphore value was reset to zero by the kernel. This design avoided race condition where the program would miss an interrupt, but as we found out, had a different flaw. Since Linux is not a real-time operating system, in rare instances when the kernel was busy, it would fail to unblock the program through the semaphore. To circumvent this problem, `mdd` (see Section 4.2.4) had a dedicated thread which checked the status of the hardware busy for that VME crate and would signal the blocked thread if the kernel failed to unblock it. However, sustained trigger rates of multiple kHz would cause kernel panic and crash the PowerPC. For lack of need and shortage of time, that problem had not been resolved since production data acquisition rates did not exceed 100 triggers per second.

If time and manpower permitted, interrupt handling would be re-done through `poll()` system call rather than through semaphores. We are quite certain that a significant improvement in kernel stability could be achieved that way.

The DAQ system was configured to expect two interrupt types:

- Data trigger on VME interrupt 2;
- End of spill trigger on VME interrupt 3.

The difference between the two interrupts was that on end of spill trigger only scalers were read out in the trigger process and all other processes sent empty data messages.

4.1.3 CBD 8210

CBD 8210 is a double height VME card allowing a parallel CAMAC branch with up to 7 crates to be driven through VME. Presently, the boards are quite difficult to find, and MIPP was able to obtain only 3: two for active use and one spare. The board characteristics include

- 16 and 24-bit CAMAC transfers,
- Two external VME interrupts,
- Comprehensive LAM (look at me) handling,
- Addition of a DMA module.

Our primary objective of 16 and 24-bit transfers was easily accomplished as it is well documented in the manual [8]. Before `VIrGen` boards were ready, we were also using the two interrupts to trigger readout. Unfortunately, we were not able to get DMA transfers to work, although the primary reason was the lack of need to boost CAMAC transfer performance: TPC was limiting data readout rates and it was readout directly through VME.

4.1.4 VME Interrupt Generator

`VIrGen` (**V**ME **I**nte**r**rumpt **Gen**erator) boards were developed at Harvard to

1. Convert trigger NIM signal into VME interrupt,
2. Time stamp each trigger to ensure that event pieces recorded on different PowerPC's corresponded to one physical event,
3. Ensure that Linux kernel does not miss an interrupt,
4. Hold off further triggers until a process on the PPC signals that readout is complete.

The board was outfitted with four inputs for four different VME interrupts (1-4). All decisions were made by XILINX FPGA.

The first objective was accomplished by feeding the NIM signal into a comparator, its output connected to FPGA input. If that interrupt channel was not holding busy, then

VME interrupt on corresponding channel was initiated and handshake was completed with the PowerPC. All boards were running off the accelerator RF clock and 32-bit time stamp was recorded on the clock cycle that fired the interrupt. Synchronization of timestamps across the 6 boards was achieved by resetting time stamp to 0 at the beginning of every run.

One of the issues that we encountered with Linux interrupts was that occasionally (apparently when the load was high), an interrupt would be missed. In order to solve that problem, `VIrGen` would keep resending VME interrupt until a process on the PowerPC would acknowledge receipt of the interrupt by writing to a register on the board. Frequency of repeating interrupts could be controlled through a register.

In order to synchronize all VME crates, once an interrupt was received, `VIrGen` set the corresponding TTL busy output high. Once readout was complete, a process on the PowerPC had to clear the busy. Externally formed logical OR of all busy signals inhibited further experimental triggers.

4.2 Online Software

4.2.1 MippIo

From the start, it was decided that offline analysis would be done in ROOT, but it was suspected that ROOT I/O would not be fast enough to cope with TPC data volume, so a dedicated I/O library was written.

MippIo was designed to write data in a structured byte-packing format organized into blocks. Each block had a 12-byte header containing block ID, version, and total block size. MIPP raw data file consisted of a file header block followed by any number of event blocks and concluded with an end of file block. In turn, each event block consisted of a number of detector blocks. Each detector block contained data as it was read from VME or CAMAC, without any pre-processing done on the PowerPC's or in the event builder.

4.2.2 Run Control and Message Passing System

Central part of the data acquisition system was Run Control Daemon (`rcd`). The process had to perform the following tasks

- Maintain the overall state of the DAQ system;

Class name	**Senders**	**Receivers**	**Description**
RCMsgConnect	All	All	Message sent by a client to request new connection and response by `rcd` to acknowledge new connection
RCMsgControl	All	Detectors, event builder, `rcd`	Generic message sent to start and stop runs, and the primary way for GUI to make `rcd` to act
RCMsgDataDir	`rcd`	GUI	List of directories to choose from for writing data
RCMsgEvBStatus	Event builder	`rcd`	Update `rcd` of event builder status
RCMsgMddStatus	`mdd`	`rcd`	Update `rcd` of `mdd` status
RCMsgPrescaleList	GUI, `rcd`	GUI, `rcd`	Changes and updates of prescale settings
RCMsgProcRel	Detectors, event builder, `mdd`	`rcd`	Inform `rcd` of the release used to compile a given binary
RCMsgRunConfig	GUI, `rcd`		Run configuration, including prescale settings, target, enabled detectors
RCMsgStatus	`rcd`	GUI	Update GUI of current status of the DAQ
RCMsgTarget	`rcd`	GUI	Pass a list of available targets to `rcd`

Table 4.1: Message classes implemented in run control.

- Process operator requests to start and stop data acquisition;
- Respond to exceptions and errors in the system.

These objectives were achieved by passing messages between different processes across the network.

Message passing system was implemented through stream sockets, allowing maximal flexibility and expansion of the DAQ system. A number of different messages were implemented (see Table 4.1), each having a 20-byte header containing message id, its number, size, second, and microsecond when the message was packed.

Upon start-up, `rcd` would open a socket to listen to incoming connections and would go into an infinite loop which polled all known sockets for activity. Once an event occurred on a socket, it would be processed by `rcd`. New connections were classified as event

builder, `mdd`, GUI, or detector process, and messages were processed sequentially. Since the number of connections was small (typically 8) and response time to nearly all messages did not involve much CPU time, this simple architecture worked very well.

Once all the software on all machines was up and running in idle state, it was up to the operator to set the run conditions (trigger prescales, set of detectors, etc) through GUI and start a run. GUI would send run configuration to `rcd` and follow it up with control message to start a run. At that point, `rcd` would

1. Figure out the current target and beam momentum by reading slow control devices;
2. Save run conditions to the database;
3. Send a start run message to event builder;
4. Wait for event builder to respond that the run has been started;
5. Send a start and pause run message to `mdd`'s;
6. Wait for every `mdd` to start up its detector processes;
7. Send a start run message to all `mdd`'s.

If any of the steps failed, run was terminated. In this process, only the first step would block the cycle of listening to incoming messages.

Requests to stop a run were processed in reverse:

1. Send a stop run message to all `mdd`'s;
2. Wait for all `mdd`'s to terminate child processes;
3. Send a stop run message to event builder;
4. Wait for event builder to finish writing data to disk;
5. Save run statistics to the database.

Unlike requests to start a run, any process could send a request to stop a run if it encountered an error. Alternatively, if any of the processes involved in the run would stop responding, run would be terminated by `rcd`.

4.2.3 Event Builder

Event builder is a FNAL Computing Division product that MIPP customized to our needs. It has to be able to receive parts of events (called subevents) from different sources, assemble them into an entire event, and write it to disk. At the beginning of the run, the process would be configured to expect a certain number of connections: one for each detector and one for each `mdd` involved. In order to synchronize parts of an event, each process had to be triggered to send a message to event builder even if there was no data read out. Events were assembled once all subevents were received.

Additional task of the event builder was to cut long runs into shorter subruns. A MIPP run was defined as a set of data with one system configuration (trigger scale down factors, high voltage, etc). A subrun was defined as a file with size less than 1 GB or not more than 30 minutes in duration if it contains at least 5000 events. Having multiple shorter files rather than one gigantic file facilitated data handling and expedited analysis on the batch farm.

4.2.4 MIPP DAQ Daemon

On each PowerPC, one process was

- Responding to `rcd` messages;
- Starting and stopping detector processes;
- Receiving and handling interrupts;
- Handling exceptions and errors during data taking.

It was named `mdd` because initially the DAQ was expected to rely on a different message passing system, and this would be the only "daemon" running. In a way, its functionality was similar to `rcd`: at the beginning of the run, all necessary processes were started, monitored during the run and terminated at the end of a run. The difference was that it responded to `rcd` and was not aware of the state of the entire DAQ system.

`mdd` was a multi-threaded program: one thread handled control messages and two "trigger" threads were handling interrupts on the two interrupt channels. As mentioned earlier, VME interrupts were handled by kernel and passed to user processes through semaphores. Once a trigger thread received an interrupt, it would lock a mutex, and one by

one get each of the detector processes to read data. Inter-process communication was also implemented through semaphores. It was necessary to have only one detector reading data at any given time because CAMAC operations were not done atomically: one VME operation transferred the data and a second operation read back the status of the last transfer. Hence if all detectors were read out simultaneously, a race condition was possible where a process would find out the status of a wrong data transfer.

An alternative design would be to link all detector libraries into `mdd` and avoid context switching. This approach was not pursued because we thought that better stability would be achieved if readout was done in a separate processes.

Trigger handling was done differently on the TPC crates than on the other two crates. The reason is that TPC events were interleaved, i.e. a trigger could proceed forward **before** the event was read out. Thus, on the TPC crates triggers were handled with the following sequence of events:

1. When triggered, `VIrGen` board would set a busy and hold it;
2. Kernel would set respective semaphore to zero;
3. `mdd` would wake up and wake up TPC process;
4. TPC process would wait for the data to be ready for readout, switch the buffer where next event was written;
5. TPC process would increment semaphore value, release `VIrGen` busy and then read data out.

The other two crates had a slightly different sequence of events: `mdd` would cycle through all detectors, increment semaphore, and then reset `VIrGen` busy. These sequences were safe against race conditions.

One of the features we found very useful was measuring readout time of every detector. This helped us to identify bottlenecks in the beginning and at a later stage was a useful debugging tool: if detector was taking much more or much less time than usual to read its data, it typically indicated a problem with the electronics, high voltage, or low voltage supplies.

4.2.5 Detector Processes

Detector processes had to fulfill a very specific role: connect to event builder, configure detector at the beginning of a run, read and buffer data for every trigger, send data to event builder on every end of spill trigger. Each process had two threads, one for each interrupt type.

4.2.6 Database Logger

In order to avoid building Postgres libraries on the PowerPC and most importantly to be able to host database on a dedicated computer rather than the DAQ server, `dbLogger` interface was written so that executables running on the PowerPC's could add and modify entries in the database. Logger daemon was running on the DAQ server, it listened to incoming connections from the PowerPC's and passed SQL commands to the Postgres server without parsing them.

The main use for `dbLogger` was to store the number of spills and triggers recorded in a given run.

4.2.7 Online Monitoring

An integral part of the data acquisition system, online monitoring was essential debugging tool and gave shifters ability to verify in nearly real time that the data written to disk was meaningful. Having the program was also essential to debug issues in MippIo and detector readout code.

Monitoring was running on a dedicated computer which had the data disks mounted through NFS. The program was constantly scanning the disks for new data files and kept updating a number of histograms for all detectors. The executable was written using ROOT for both histograms and graphical user interface. Important part of online monitoring was writing files out at the end of each run so that histograms from different runs could be quickly compared at a later time.

4.2.8 Software Release System

Entire experiment depended on the DAQ system, therefore some order was brought into software development cycle by compiling frozen releases. Rigorous testing was done before a release was made, and at any point in time, the most recent and the previous stable

releases were available to operators. Release of every DAQ executable for every run was stored in the database so that at a later time potential detector or data integrity problems could be easily linked to software release.

4.3 Slow Controls

Environment in the experimental hall as well as settings and readbacks of devices were controlled and continually monitored by computer. These included gas pressures, temperatures, magnet current settings, and high voltage settings.

4.3.1 iFix

Intellusion iFix system was used as a front-end for APACS control. It was used to

1. Read air and gas pressures, multiple temperature sensors, humidity sensor;
2. Control the pressure in beam Cherenkov counters;
3. Control the flow of gas through threshold Cherenkov counter;
4. Act as an interlock on the RICH cooling system;
5. Monitor chamber gas flow;
6. Monitor gas mixing for drift chambers;
7. Monitor and control cryogenic target.

XML-RPC server was running on the Windows PC where iFix was running to provide a way to store variables to the Postgres database and for DAQ to find out the status of cryogenic target.

4.3.2 ACNET

ACNET is Accelerator Control NETwork developed at and supported by FNAL. We relied upon ACNET to

1. Control and monitor secondary beamline dipole and quadrupole magnets;
2. Control momentum collimator slit width;

3. Monitor beam profiles;
4. Monitor spill structure;
5. Control and monitor analysis magnet currents;
6. Monitor Hall probes installed in the apertures of analysis magnets;
7. Control and monitor RICH high voltage supplies;
8. Control beam Cherenkov mirror positions;
9. Monitor wire chamber and EM calorimeter voltages and currents;
10. Monitor spill intensity;
11. Monitor hall and target temperature;
12. Control target wheel position;

Similarly to iFix, we used XML-RPC server provided by FNAL Beams Division to control devices and record their state into the database.

4.3.3 High Voltage

High voltages on PMT's and TPC anodes were controlled through two LeCroy Research Systems 1440 systems. In order to control the mainframes from the counting house 100 m away, Equinox serial hub was connected to the private sub-net. This device enabled access to serial devices over 100 Mbit network.

Once high voltages were set, the system would continually cycle through all known channels, store the readback voltage to database and verify that the channel did not trip. This was especially important for TPC anodes which did occasionally trip. Prompt detection of trips ensured that as little data as possible was lost.

Chapter 5

Beamline

5.1 Accelerator

Beam for MIPP experiment was extracted from the Main Injector. The LINAC followed by Booster accelerate batches of protons to 8 GeV kinetic energy, and the Main Injector RF cavities accelerate protons to 120 GeV/c . Up to 7 Booster batches can be injected into the Main Injector to be accelerated simultaneously. Protons for the MINOS experiment or for $\bar{p}$-production for the Tevatron collider and are extracted in single turn. MIPP spectrometer required resonant extraction out of the Main Injector. Beam extracted towards the Switchyard, passed through the A-section of the Tevatron ring, and at the Switchyard beam could be split between Meson Test area, Meson Center (MC) area, and beam dump. MIPP spectrometer occupied MC7 hall.

MIPP experiment was approved under condition that it would not impact the accelerator program by more than 5%. In practice that meant that we were not to slow down $\bar{p}$-production by more than 5%. At the beginning of the MIPP run, this translated into extracting all but one Booster batch to $\bar{p}$-production, and slowly extracting the last batch to MIPP. Since resonant extraction increased the length of the Main Injector time cycle, while $\bar{p}$ stack was small (hence stacking rate high), MIPP received about six 600 ms spills per minute. Once the $\bar{p}$ stack grew and stacking rate slowed down, MIPP was receiving up to 15 spills per minute.

In March 2005, NuMI started receiving proton beam for the MINOS experiment, and in April 2005, machine operation was changed so that MINOS and $\bar{p}$-production co-existed with single-turn extraction to each destination, and a 4 second spill was extracted

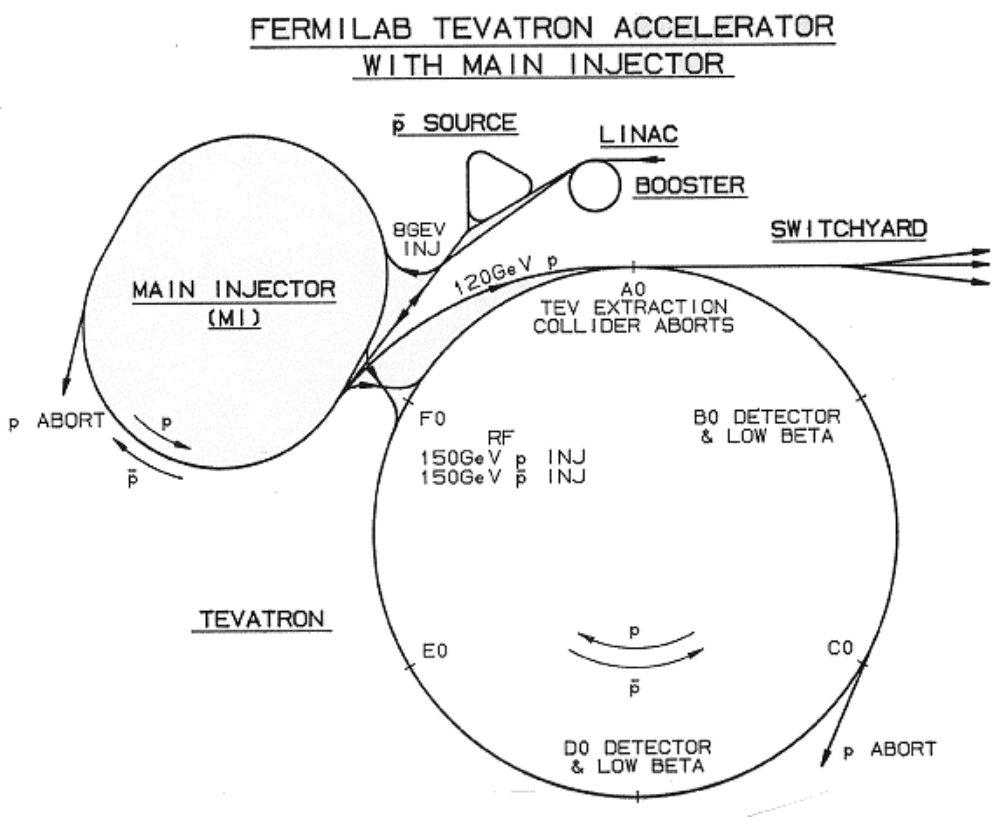

Figure 5.1: Schematic of the FNAL accelerator complex. MIPP experiment was located in the beamline past Switchyard.

to the Switchyard once every 2 minutes. MIPP operated under these conditions through February, 2006.

MIPP beamline was operated in two distinct modes:

- 120 GeV/c primary protons
- $5 - 90$ GeV/c secondary particles produced on a copper target.

5.2 Primary Beam

The minimum rate at which protons could be extracted from the Main Injector was about 10^8 particles per second. Radiation safety mandated that the experimental hall was to receive no more than 10^6 particles per second. Under normal circumstances this limitation did not affect data rates, since considerations of pileup and build up of space charge in the TPC made it impossible for the experiment to handle more than 10^5 particles per second, more realistically $3-5\times10^4$. In short, proton intensity had to be reduced by at least 3 orders of magnitude in the beamline between the Main Injector and MC7 hall. This was achieved by blowing up the beam size before passing it through a pin-hole collimator, and then focusing the beam on the experimental target.

For NuMI target running, beam intensity was further reduced to about 10^3 particles per 4 second spill. This was necessary because with a 2 interaction length target, 90% of incident particles interact, hence higher rates would create unacceptable level of pileup.

5.3 Secondary Beam

At the entrance to MC6 area, 120 GeV protons were focused onto a $0.5\times0.5\times20$ cm copper target, located 97 m upstream of the experimental target. The target is about 2 interaction lengths, hence a tenth of the primary beam was not interacting and was dumped into a series of concrete blocks. Beam was striking the target at 1.3° with respect to the horizontal, and 4 dipole kicks – two before and two after the slit collimator – were bringing horizontal beam onto the experimental target.

In order to minimize dp/p, large dispersion had to be achieved at the collimator. Six quadrupole magnets – three before and three after the collimator – enabled us to increase dispersion and then focus the beam on the target.

An estimate of particle production, gives RMS transverse momentum of about 400 MeV/c. Physical transverse dimension of the target is $\pm$2.5 mm. Hence, RMS emittance of the secondary beam varies from $\sim$ 200 mm·mrad at 5 GeV/c down to $\sim$ 11 mm·mrad at 90 GeV/c (total emittance is roughly 4 times larger). The experimental target is 5 cm in diameter, and Beam Cherenkov operation requires less than 1 mrad divergence, that is the maximum acceptable total emittance is 25 mm·mrad. Hence, for all beam momenta, we had to cut down emittance at the momentum of interest.

5.3.1 Optimizing Beam Quality

Once MIPP detectors were up and running, we quickly realized that in order to take quality data with secondary beam, not only did we have to focus the beam on the target, but also reduce the amount of beam halo that results from scraping beamline elements. There is an infinite number of quadrupole current settings that provide a well focused beam, but most of them result in significant scraping in dipole beam pipes downstream of the collimator and degrade data quality in two ways:

- Faking interaction trigger, especially DC1-based trigger,
- Filling up TPC volume and tracking chambers with so many tracks that event becomes unreconstructable.

The effect on the interaction trigger was reduced by relying more heavily on the scintillator interaction trigger (see Section 3.3.2), and veto paddle helped a little bit, but the right way to improve operating conditions was to address the source of the problem: beamline settings.

A fairly complete model of secondary beamline was assembled and analyzed using OptiM software written by Valeri Lebedev[27]. The model included realistic calculation of magnetic field in dipoles and quadrupoles based on measurements done at the FNAL Technical Division, and all apertures.[1] Once this model was complete, one could dial in the quadrupole currents and quickly understand what was happening. It became clear that significant scraping occurred in the last dipole magnet, well after the collimator, with only one quadrupole magnet behind it (see Figures 5.2 and 5.3). Of all places where scraping could occur, this is one of the worst.

[1]The model assembled for use with Methodical Accelerator Design (MAD) Program lacked apertures, and hence was incapable of addressing the problems that MIPP experiment was facing.

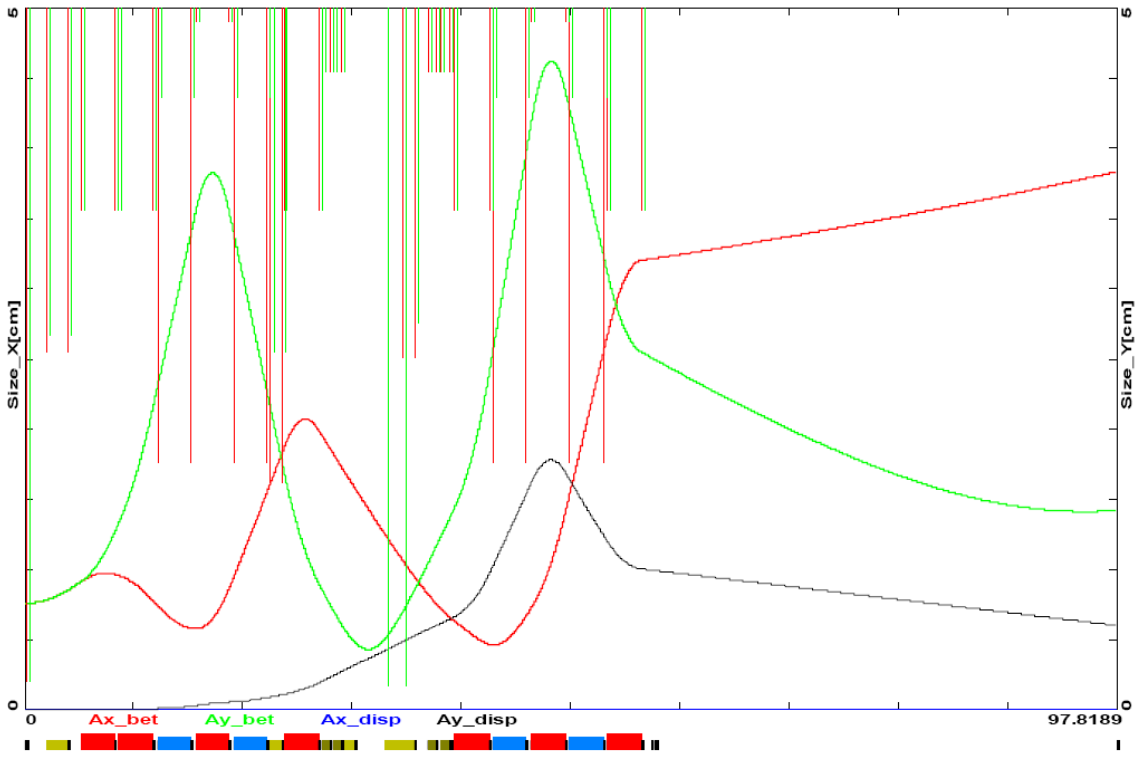

Figure 5.2: Top plot shows beam sizes (x in red, y in green) and dispersion (black curve) superimposed on top of specified apertures (again, red for x and green for y). Apertures exist in the model as line objects (rather than a box), hence aperture is specified at the front and back of every element. This plot can be produced with conservative assumptions (smaller than real-life emittance) about particle production on the copper target. Shown at the bottom are beamline elements: tallest red boxes are quads, medium blue boxes are dipoles, and khaki short boxes are scrapers and collimator.

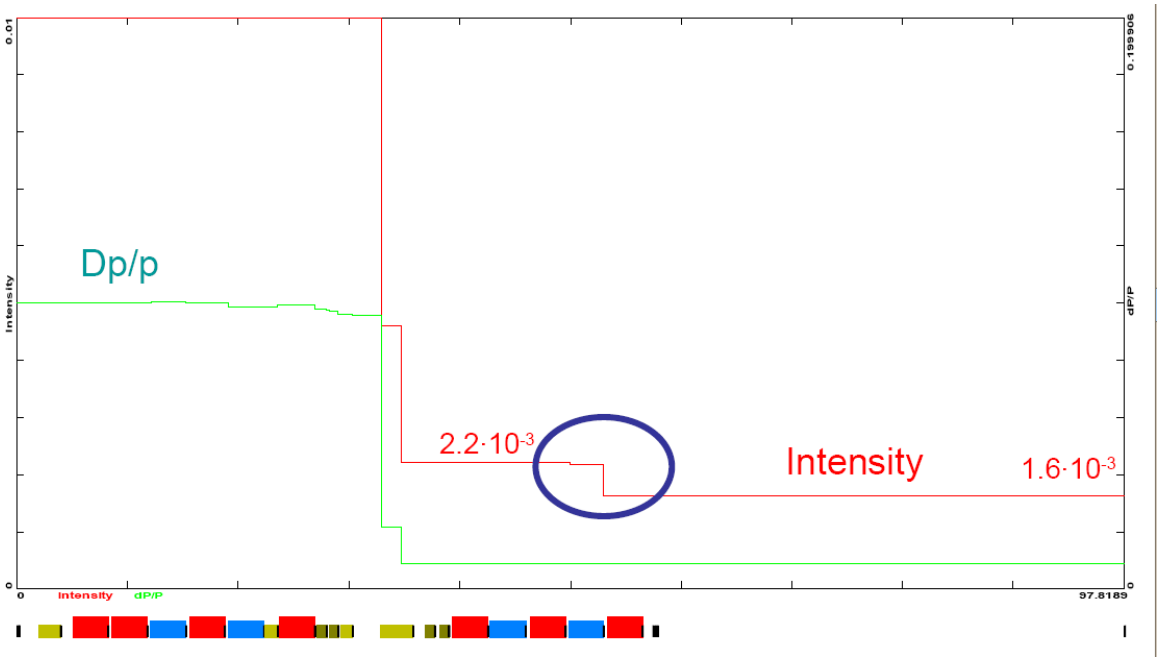

Figure 5.3: Intensity plot was created by tracking a very wide (10% dp/p) distribution of particles. OptiM tracking is very simple: a particle is lost if it hits an aperture, hence intensity is a step-function. As expected, most particles are lost at the collimator, still a large number hit the aperture of the last dipole (the loss highlighted by the blue oval).

While it was no longer feasible to move beamline elements, scrapers in particular, the following approach helped select an acceptable solution leaving all elements in their positions.

Rather than modeling forward-going beam, beam parameters (emittance, β-function, and its derivative) were chosen at the **primary target** and beam was transported **backward** and beamline settings chosen so that the beam was far away from apertures downstream of the collimator (in real beamline), touching every aperture upstream of the collimator and focusing to 0.25 cm spot at the location of the copper target with zero dispersion. The last 2 requirements are necessary to reflect reality of particles being produced from a finite-size target. Note that one does not need to mimic angular divergence of the beam at the secondary target because we are intentionally selecting a small subset of secondary particles, since full emittance at the secondary target is larger than what the experiment can handle.

Parameters which can be used to characterize beam at some location in z are:

- Beam size (x_{max}, y_{max}),
- Beam divergence ($\theta_{x,max}$, $\theta_{y,max}$),
- Beam emittance (ϵ_x, ϵ_y),
- Beta functions (β_x, β_y),
- Derivative of beta function (α_x, α_y),
- Dispersion – only y-dispersion exists (δ_y),
- Derivative of dispersion ($d\delta_y/dz$).

Of course, these parameters are not independent, since for each coordinate we have

$$x_{max}^2 = \epsilon\beta \tag{5.1}$$

$$\theta_{max}^2 = \frac{\epsilon}{\beta}\left(1+\alpha^2\right) \tag{5.2}$$

Primary consideration for choosing beam parameters at the experimental target was limiting divergence of the beam to 1 mrad, required by beam Cherenkov counters, and spot size of 2.5 cm, the size of the secondary target. Another more subtle factor is that non-dispersive beam lines tend to be more forgiving to errors in quadrupole gradients

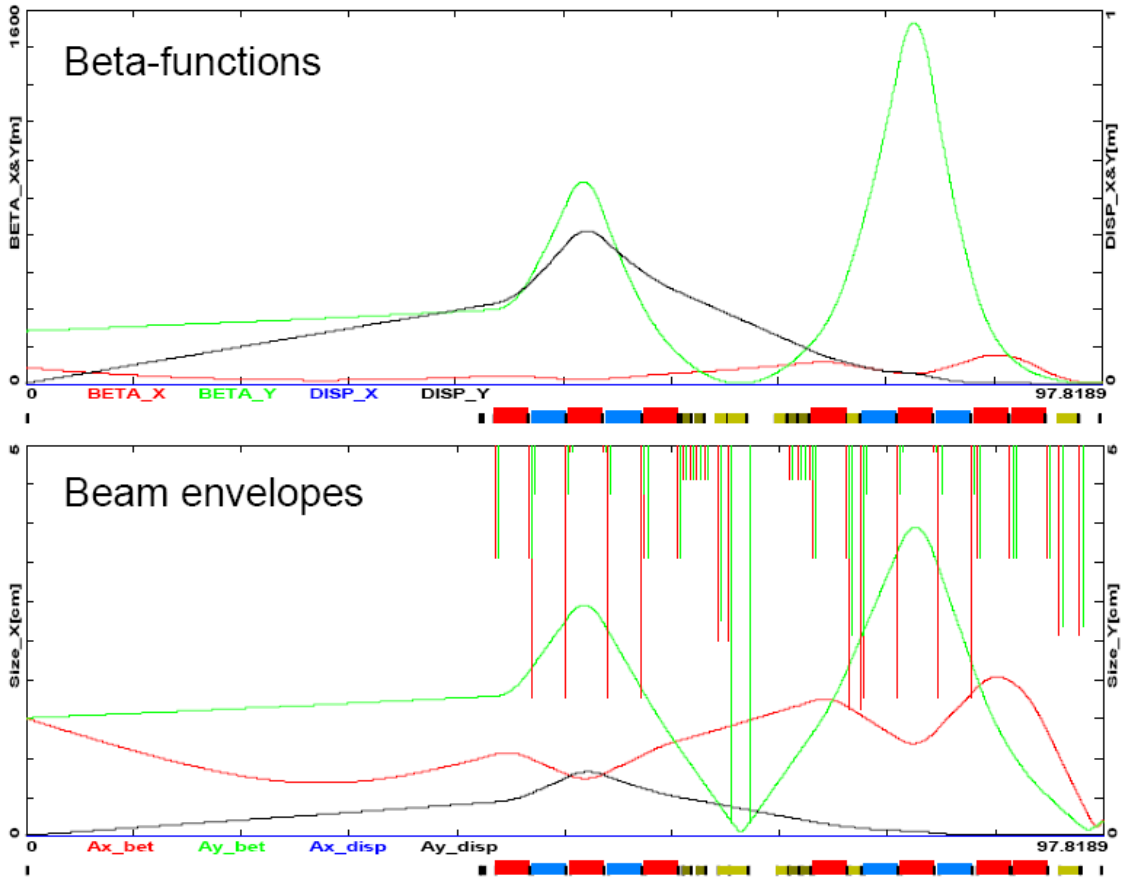

Figure 5.4: Beta functions and beam envelopes for a solution which satisfies the criterion of staying far away from the post-collimator apertures and touching the largest number of apertures upstream of the collimator.

and therefore more stable. Hence dispersion was chosen to be 0 at the experimental target. Of these parameters, we can chose to vary $x_{x/y,max}, \theta_{x/y,max}, \alpha_{x/y}$, and $d\delta_y/dz$ within reasonable limits and look for current settings to satisfy specified requirements.

An acceptable solution was obtained with $x_{x/y,max} = 1.5$ cm, $\theta_{x,max} = 0.5$ mrad, $\theta_{y,max} = 0.1$ mrad, $\alpha_x = 2$, $\alpha_y = -0.9$, and $d\delta_y/dz = 5 \times 10^{-3}$. Figure 5.4 shows beta functions and beam envelopes for this backward beam line. This choice of magnet currents keeps the beam at least 1 mm away from all beam pipes downstream of the collimator, and has the beam envelope touch the collimator.

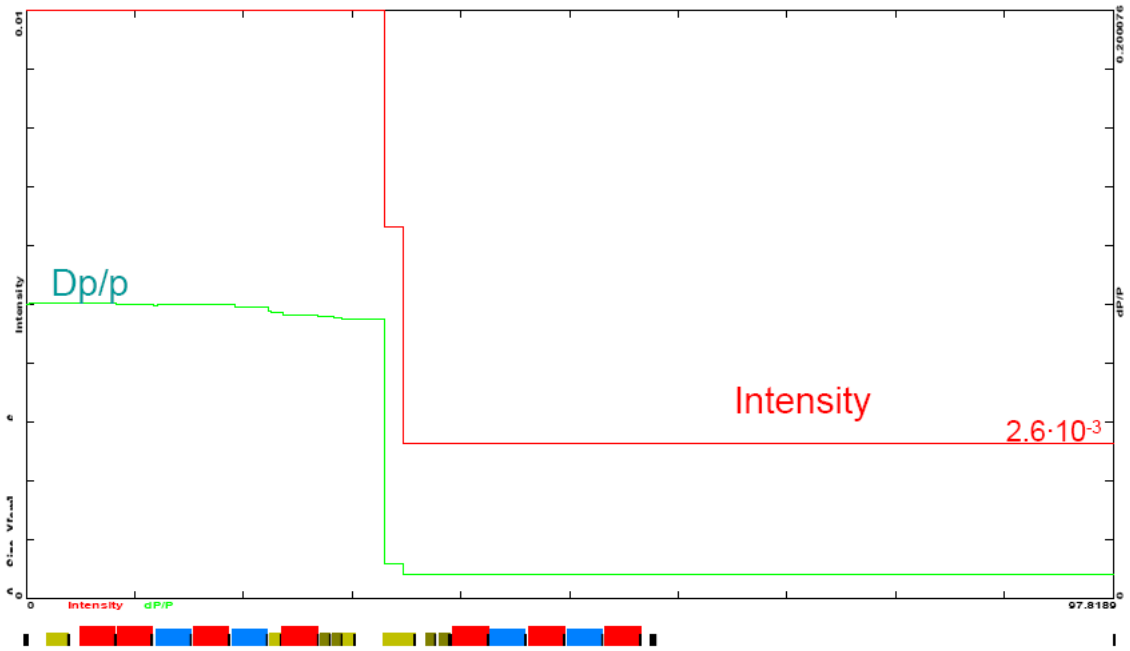

Figure 5.5: Tracking results for beamline settings obtained through reversed beamline. Unlike the first solution, this one does not show scraping in the fourth dipole magnet.

When particles were tracked forward through this solution, not only scraping was greatly reduced, but more particles were getting through, as is clear from Figure 5.5. Clear improvement was observed in the quality of experimental data when quadrupole currents derived from this solution were set, and a somewhat refined solution inspired by this modeling was used to set secondary beam.

Chapter 6

Event Reconstruction

6.1 Track Fitting

The overwhelming majority of particle trajectories (tracks) in MIPP are fit either to straight lines or track templates. Approach to both methods is presented in this section.

The task is to fit a 3-dimensional curve to a collection of measurements with different orientations in xy-plane (also referred to as views) at different z locations. Defining measurement this way allows one to easily combine 3-dimensional points computed in the TPC with 2-dimensional chamber measurements: one simply splits the TPC point into two 2-dimensional measurements.

Our convention is to measure the angle between wire orientation and y-axis, so that x-measurements (vertical wires) have $\theta = 0$ and θ is increasing clockwise. To make coordinate u of a given view collinear with x and y-axis when appropriate, $\theta = -90^\circ$ for y-measurements (horizontal wires). Figure 6.1 shows a diagram of this convention. Then a point (x, y) can be converted to u in a given view through

$$u = x \cos\theta - y \sin\theta. \tag{6.1}$$

6.1.1 Straight Line Fitting

Fitting a straight line to collection of measurements is easily done through generalized least squares method. A line in space is described by 6 parameters. We choose to represent the line through the two points at smallest and largest z: (x_1, y_1, z_1) and

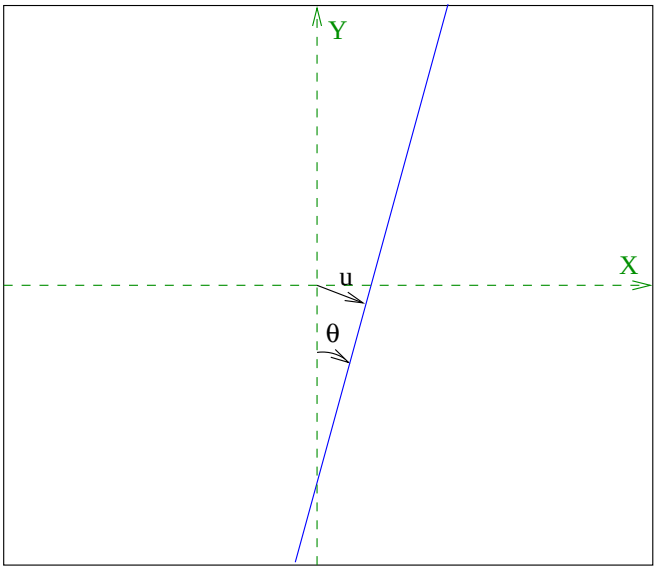

Figure 6.1: Sketch of wire plane geometry.

(x_2, y_2, z_2). Once the choice of z_1 and z_2 is made, we need to determine the four parameters $\vec{p} = (x_1, y_1, x_2, y_2)$.

At any z, we have

$$\begin{cases} x(z) = \dfrac{x_1(z - z_2) - x_2(z - z_1)}{z_1 - z_2} \\ y(z) = \dfrac{y_1(z - z_2) - y_2(z - z_1)}{z_1 - z_2} \end{cases} \tag{6.2}$$

Then using Equation 6.1 we can predict u in a given view at z through

$$u(z; i) = \sum_{j=1,4} c_{ij} p_j, \tag{6.3}$$

where

$$\vec{c}_i = \begin{pmatrix} \dfrac{z - z_2}{z_1 - z_2} \cos\theta_i \\ -\dfrac{z - z_2}{z_1 - z_2} \sin\theta_i \\ -\dfrac{z - z_1}{z_1 - z_2} \cos\theta_i \\ \dfrac{z - z_1}{z_1 - z_2} \sin\theta_i \end{pmatrix}$$

With N measurements, we write the least squares equation

$$\chi^2 = \sum_{i=1,N} w_i \left(u_i - \sum_j c_{ij} p_j \right)^2, \tag{6.4}$$

where w_i is the weight given to the wire in the track. We seek for solution which minimizes χ^2, that is

$$\frac{\partial}{\partial p_k}\chi^2 = 2\sum_N w_i c_{ik}\left(\sum_j c_{ij}p_j - u_i\right) = 0 \tag{6.5}$$

We can rewrite Equation 6.5 as a matrix equation

$$\vec{v} = \mathbf{M}\vec{p}, \tag{6.6}$$

where

$$v_j = \sum_i w_i u_i c_{ij}$$
$$M_{jk} = \sum_i w_i c_{ij} c_{ik}$$

Solving Equation 6.5 gives

$$\vec{p} = \mathbf{M}^{-1}\vec{v},$$
$$\chi^2 = \sum_i u_i w_i^2 - \vec{p}\cdot\vec{v}.$$

Finally, since

$$\frac{1}{2}\frac{\partial^2}{\partial p_i \partial p_j}\chi^2 = M_{ij},$$

i.e. M is the inverse covariance matrix, errors on parameters are given by

$$\sigma_{p_i}^2 = M_{ij}^{-1}.$$

6.1.2 Template Track Fitting

When track traverses regions of space with significant magnetic field, one needs to determine track momentum in addition to location and direction at a given z_0. If one has a rough guess at track parameters and the field is sufficiently smooth, the problem can be solved by fitting the set of measurements to a track template. Advantage of this method is the small required number of swims through the magnetic field. Disadvantage of this method is that track direction is represented by dx/dz and dy/dz, which are difficult to use when track angle to z-axis is large.

As charged particle traverses magnetic field, to first order its bend angle and therefore displacement from straight-line track is proportional to q/p, the charge and momentum

of the particle. That is, at a given z, we can represent particle position with 5 parameters: $Q = q/p$, position (x, y) and direction $(dx/dz, dy/dz)$ at $z = z_0$:

$$\begin{cases} x = x_0 + \left.\dfrac{dx}{dz}\right|_{z=z_0} \cdot (z - z_0) + Q\lambda_x(z) \\ y = y_0 + \left.\dfrac{dy}{dz}\right|_{z=z_0} \cdot (z - z_0) + Q\lambda_y(z), \end{cases} \tag{6.7}$$

where λ_x and λ_y can be interpreted as displacement from straight-line trajectory for a particle with $q/p = 1$ and can be calculated by swimming a track with guess parameters $(Q \neq 0)$ from z_0 and setting

$$\begin{cases} \lambda_x(z) = \dfrac{1}{Q}\left(x_{swim} - x_0 - \left.\dfrac{dx}{dz}\right|_{z=z_0} \cdot (z - z_0)\right) \\ \lambda_y(z) = \dfrac{1}{Q}\left(y_{swim} - y_0 - \left.\dfrac{dy}{dz}\right|_{z=z_0} \cdot (z - z_0)\right). \end{cases} \tag{6.8}$$

When $|dx/dz| < 1$ and $|dy/dz| < 1$ at z_0 and z, the errors from this representation are negligible.

Equipped with Equations 6.7 and 6.8, we need a guess at track parameters to compute $\lambda x, y$ at z of every measurement, and we can reuse linearized chi squared formalism with

$$\vec{p} = \begin{pmatrix} x(z_0) \\ y(z_0) \\ dx/dz(z_0) \\ dy/dz(z_0) \\ Q(z_0) \end{pmatrix}, \qquad \vec{c_i} = \begin{pmatrix} \cos\theta_i \\ -\sin\theta_i \\ (z_i - z_0)\cos\theta_i \\ -(z_i - z_0)\sin\theta_i \\ \lambda_y(z_i)\cos\theta_i - \lambda_x(z_i)\sin\theta_i \end{pmatrix}. \tag{6.9}$$

Notice that if the track template takes energy loss into account, this approach will to first order behave correctly, especially if energy loss over the length of the track is small compared to initial track energy.

6.1.3 Fail Safe Fitting

In case template track fit is inadequate for a track, the fail-safe method of fitting is minimizing weighed distance from measurements to the track using ROOT TMinuit package. Different weights can be chosen for x, y, z, so that even when the track is nearly perpendicular to z-axis its parameters will be computed correctly.

Given point (x, y, z) the closest point on the track (x_t, y_t, z_t) was found by minimizing

$$D^2 = w_x(x - x_t)^2 + w_y(y - y_t)^2 + w_z(z - z_t)^2. \tag{6.10}$$

If the track is straight, from the closest point on the track stored in memory, the step that one needs to take to minimize D^2 is given by [1]

$$s = \frac{w_x(x - x_t)p_x + w_y(y - y_t)p_y + w_z(z - z_t)p_z}{w_x p_x^2 + w_y p_y^2 + w_z p_z^2}, \tag{6.11}$$

where unit vector (p_x, p_y, p_z) represents direction of the track at (x_t, y_t, z_t). If the track is not a straight line, then one has to repeat the procedure until s is sufficiently small.

6.2 Wire Chambers

MIPP wire chambers are grouped into 3 triplets (BC123, DC123, DC4/PWC56) with two magnets separating the triplets. To first order, curvature due to magnetic field is negligible between the magnets as well as before Jolly Green Giant and after Rosie, so that one can reconstruct a straight line segment in each group. Once segments are found, it is simple to test whether a combination of DC123 segment with DC4/PWC56 segment appears to form a reasonable track candidate bent by Rosie. Finally, if track candidate momentum is similar to beam momentum, one can check whether combining the candidate with BC123 segment will give a reasonable 9-chamber track.

Having reliable track fits with all 9 chambers was crucial to aligning chambers and finding inconsistencies of description of spectrometer geometry.

6.2.1 Wire Clusters

A wire cluster is defined as either one wire or a group of contiguous wires. In drift chambers, we clustered wires only if their hit times were similar and the cluster size is limited to two wires. In PWC's cluster size is unlimited.

Chamber preamplifiers and discriminators would occasionally ring so that all 8 wires were hit. In those cases, wires from that preamp are not used for tracking in order to improve the signal to noise ratio.

[1] If $w_x = w_y = w_z = 1$ Equation 6.11 reduces to dot product of track direction and vector pointing from (x_t, y_t, z_t) to (x, y, z).

Once wires were grouped, the geometric center of the cluster in chamber coordinate system is computed through

$$u_{loc} = D_{plane}(W - W_0), \tag{6.12}$$

where D_{plane} is the wire spacing, and W_0 is the hypothetical wire that goes through $u = 0$ in local reference frame. A point on the wire $(u\cos\theta_{loc}, -u\sin\theta_{loc}, z_{loc})$ is then transformed to global reference frame $(x_{glob}, y_{glob}, z_{glob})$, taking into account chamber rotation and position. Finally, the global u of the cluster is obtained from (x_{glob}, y_{glob}) through Equation 6.1. Note that at this stage z_{glob} is not a meaningful coordinate because we do not know where along the cluster the hit occurred.

6.2.2 Wire Crosses

To simplify track segment pattern recognition, we formed 3-dimensional space points from wires in at least 2 views of the same chamber. Having 3D space points enabled us to apply the same track finding algorithm to BC1+BC2+BC3, DC1+DC2+DC3, and DC4+PWC5+PWC6 segments. Wire plane angles (see Table 2.1) are the same for BCs and DCs – subject to small corrections from alignment – so one could imagine doing 2-dimensional uz-search in BCs and DCs, but having one algorithm for all triplets of chambers made it easier to maintain code.

From Equation 6.1, it follows that coordinates of intersection of two wires is given by

$$\begin{cases} x = \dfrac{u_1\sin\theta_2 - u_2\sin\theta_1}{\cos\theta_1\sin\theta_2 - \sin\theta_1\cos\theta_2}, \\ y = \dfrac{u_1\cos\theta_2 - u_2\cos\theta_1}{\cos\theta_1\sin\theta_2 - \sin\theta_1\cos\theta_2}. \end{cases} \tag{6.13}$$

If more than two wires belong to a cross, its position can be computed through least squares approach (Equation 6.4), where

$$\vec{p} = \begin{pmatrix} x \\ y \end{pmatrix}, \qquad \vec{c_i} = \begin{pmatrix} \cos\theta_i \\ -\sin\theta_i \end{pmatrix}.$$

Wire crosses are then found with the following algorithm:

1. Calculate intersection of two wire clusters from different planes which do not belong to a common wire cross and verify that (x, y) is within the active chamber volume.

2. Look for wire clusters consistent with calculated (x, y) in remaining two views of the chamber.

3. Fit position of wire cross using all 4 views (if available). If χ^2 is not acceptable, then choose the 3-plane combination with the better χ^2.

Once all crosses are found, crosses which are subset of a different cross are eliminated.

The final step in the algorithm is to compute the number of clusters in each cross that belong to crosses with more clusters. Crosses where all wires are used in larger crosses are typically shadows of valid crosses, and they were not used to seed track segments.

6.2.3 Track Segments

Track segment finding is similar to wire cross finding: the algorithm evaluated all possible combinations of chamber space points and kept the ones that contained information from all 3 chambers in a triplet and had acceptable χ^2.

For the purpose of segment finding, a data structure was defined, which the following information:

- Wire crosses in the segment,
- Wire clusters in the segment,
- Minimum and maximum wire time,
- Segment fit parameters as (x_1, y_1, z_1) and (x_2, y_2, z_2).

A cross/cluster data structure was defined to hold

- Minimum and maximum wire time for cross/cluster,
- List of segments the cross/cluster is in.

With data organized this way, any of the following tests become fast:

- Are two crosses compatible in time?
- Is cross/cluster compatible in time with existing segment?
- Are two crosses already part of one segment?
- How many clusters are shared between two segments?

Track finding algorithm follows these steps:

1. Loop over all binary combinations of crosses of every pair of chambers.

2. If the two crosses compatible in time and are not part of a formed segment, continue to next step.

3. Fit a 3-dimensional line to the clusters of the two crosses and make prediction of position at the third chamber.

4. Given prediction, find the closest cross or cluster which is compatible in time with initial crosses. If newly fit segment has acceptable χ^2, go to step 6.

5. Find the closest wire cluster in each view of the third chamber compatible in time with initial crosses. If no acceptable clusters or more than one cluster is found, go to step 1.

6. If the segment has the minimum required number of clusters, save it and update track list of every cross/cluster.

At the end of segment search, it was important to filter out essentially duplicate tracks. Any track that had less than required number of unique clusters was not saved.

6.2.4 Chamber Track Candidates

A chamber track candidate is defined as a combination of DC123 and DC4/PWC56 track segments. Track bend in the Rosie magnet enables us to measure momentum of the particle. Search for track candidates was done by matching predicted position in the center of Rosie from both segments and matching dy/dz of the two segments. While the windows on both selection were quite wide (12 cm match in x, 10 cm in y, and 5 mrad in dx/dz), they helped reduce the combinatorics of possible track candidates before a template track fit was attempted.

Potential pair of segments were first fitted using a 120 GeV/c particle template. The results of the fit were used to obtain a better template and the track was refit. The track was accepted or rejected based on the χ^2 of the second fit.

Final step of the algorithm was to attempt to match the track with BC123 track segment. Obviously wrong candidates were filtered out by requiring that the charge of the candidate match the charge of beam particles in that run, and that momentum be at least

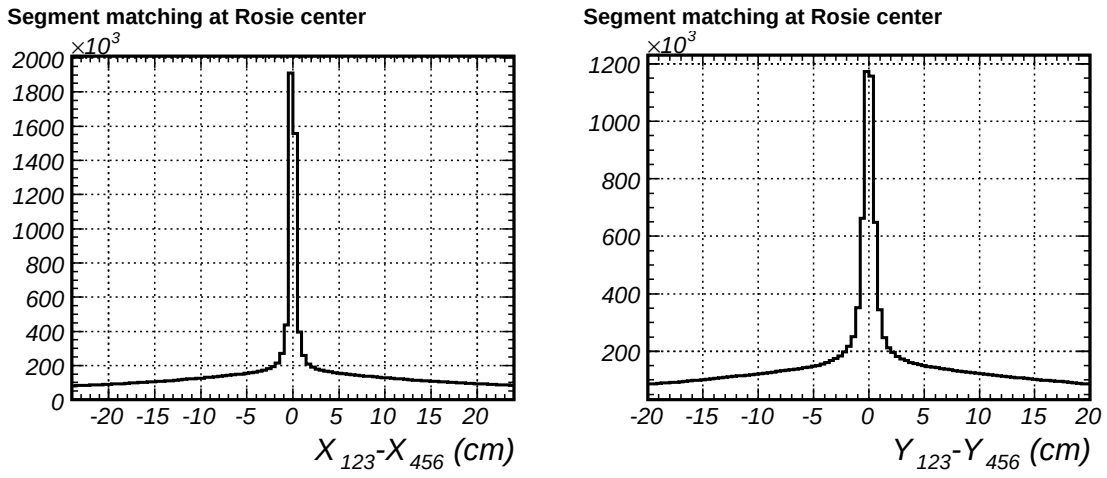

Figure 6.2: Matching of DC123 and DC4/PWC56 segments in the center of Rosie.

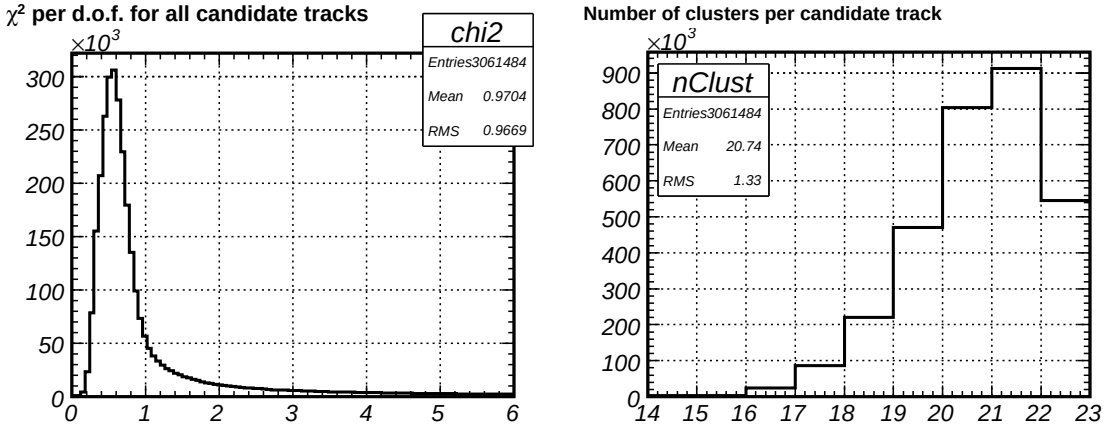

Figure 6.3: Distribution of χ^2 per degree of freedom and number of clusters in chamber track candidates.

0.8 of beam particle momentum. Decision on whether to keep the track candidate as a 6-chamber or a 9-chamber object was made based on the χ^2 of the resulting track.

6.3 Time Projection Chamber

The TPC dominates event size and is the most complex detector to reconstruct. The primary problems facing track reconstruction in the TPC are

- Large dead sections of the detector;
- 16 μs integration time, which makes the TPC very sensitive to out-of-time tracks.

Reconstruction algorithm was adopted from the algorithm used by BNL E910, which is described in great detail in [39] and MIPP-specific aspects in [32]. The main steps of reconstruction are:

1. Create two-dimensional contiguous clusters in each padrow (z-slice) of the TPC. Each cluster is fitted to a Gamma function in t: $q(t) = At^{\lambda}e^{-t}$, and a Gaussian in x. For hits with insufficient number of pad columns, the position in x was calculated through weighted mean, using charge collected on the pad as the weight.

2. Compute hit position by computing electron trajectory starting from the TPC anode plane (see Section 7.5.2).

3. Search for tracks using what amounts to a simplified Kalman filter approach. Starting from the downstream end of the chamber – where the distance between tracks is the largest – a track is formed by connecting the closest hits in the neighboring padrows. The track is then extended and position prediction is made in the next padrow. Acceptable hits are added into the track until no new hits are found in the upstream direction. Hit search is then reversed to pick up hits in the downstream direction.

4. Similar tracks – those that share a large fraction of their hits – are merged to remove essentially duplicated tracks.

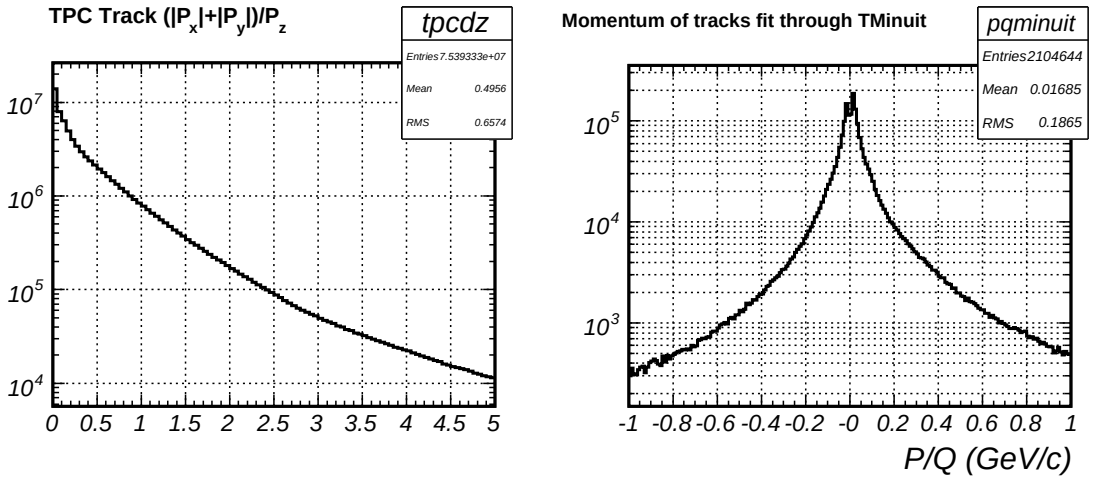

Figure 6.4: Ratio for selecting tracks which are to be fit through `TMinuit` and momenta of those tracks.

6.4 Global Tracking

The objectives of global tracking are

1. Refit TPC tracks using real JGG magnetic field;
2. Combine TPC tracks with chamber track candidates, track segments, or stand-alone wire clusters.

6.4.1 Refitting TPC tracks

If the track angle is not too large with respect to the z-axis, template track fit approach is adequate to refit the TPC track. However, if the track angle to z-axis is too large, template fitter is not able to handle it adequately, and the track is passed to fail-safe `TMinuit` fitter. Selection of the fitter was based on two criteria:

1. Ratio $(|P_x| + |P_y|)/P_z$ in the middle of the track, at $\frac{1}{4}$ and $\frac{3}{4}$ of z along the track;
2. Number of padrows in the track.

Tracks with ratio above 4 and tracks that span fewer than 4 padrows, were not attempted to be fit through template fitter. The tracks selected for slow fitter are predominantly low momentum tracks (see Figure 6.4).

In either fitter, track parameters were evaluated in the middle of the track. This way potential problems with very large dx/dz or dy/dz at the pivot point are minimized. Seed track parameters are extracted from the helical fit. Momentum was computed based on track curvature, under assumption of homogeneous magnetic field.

In the event that the template fitter could not re-swim the track from the first hit to the last hit, template fitting was considered failed, and the track was passed to the slower `TMinuit` fitter.

6.4.2 Cleaning up TPC Tracks

MIPP TPC reconstruction algorithm had two minor problems which resulted in tracks with very large χ^2:

- Two nearby tracks could be merged together;
- Track finding algorithm could grab hits that were inconsistent with the rest of the hits on the track.

To alleviate these problems, we took the following approach. Hits were removed from the track until its χ^2 per degree of freedom was under 2. Then we continued to remove those hits which contributed more than 8 times than the average contribution to χ^2. This approach cleaned up TPC tracks without sacrificing well reconstructed tracks.

6.4.3 Merging Tracks

Prior to fitting TPC tracks using the magnet field map, tracks were merged using a more sophisticated approach than just looking at the number of shared TPC and wire chamber hits. Similarity of tracks was judged by computing "cross χ^2" as the sum of weighted residuals squared of one track using parameters of another track. If the goodness of fit based on cross χ^2 was larger than 0.1 or the ratio of the first track's χ^2 to cross χ^2 was larger than 0.15, then the tracks were merged together.

6.4.4 Matching TPC Tracks to Chambers

Global tracks – those including TPC and chamber information – are formed by first attempting to match TPC tracks to chamber track candidates at DC1. If a matching candidate is not found, then a matching DC123 segment is searched for. If the segment is

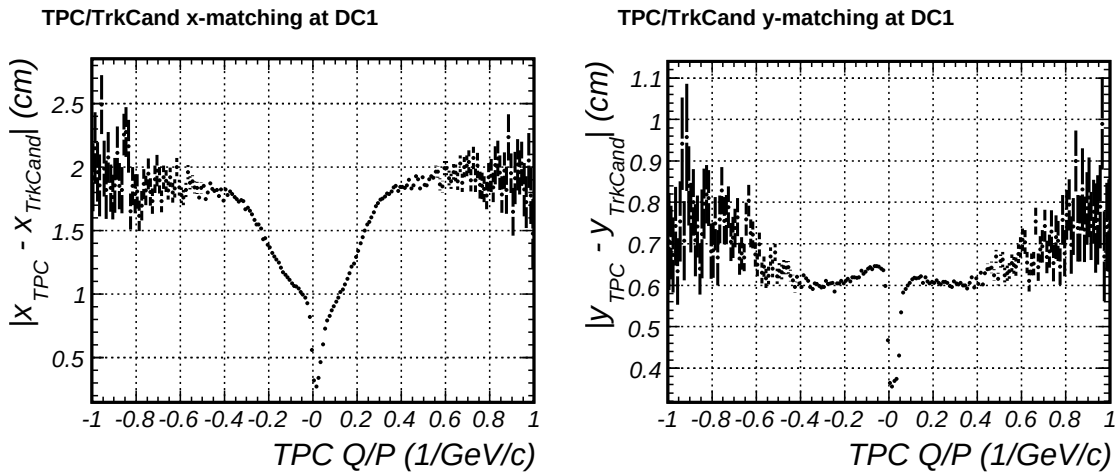

Figure 6.5: Dependence of position matching of the TPC and chamber track candidates when position is computed at DC1.

not found, then we search for nearest wire clusters in DC1, DC2, and DC3, refitting the track with the new information each time a hit is found. If predicted track position at a chamber is outside of the active area of the chamber, then no attempt is made to extend the track further. The tracks that were extended to DC3, the process continues in downstream chambers, first searching for matching C456 track segments and descending to the level of clusters if it is necessary.

6.4.5 Tracks in the Event Stream

Saving only track measurements and parameters to event stream has the potential of slowing down analysis modules that need tracks to predict track position and direction at various z along the spectrometer, since every module would have to re-swim the track in order to extract track prediction. Third order interpolation which matches two end-points and track direction at the two points was implemented to make trajectory prediction without swimming. While global tracking module still had the states of the swum track, points were inserted in the middle of two neighboring points so that third order prediction at 1/4, 1/2, and 3/4 distance in z was within 100 micron of the swim prediction. This accuracy was sufficient for all modules which used tracking results.

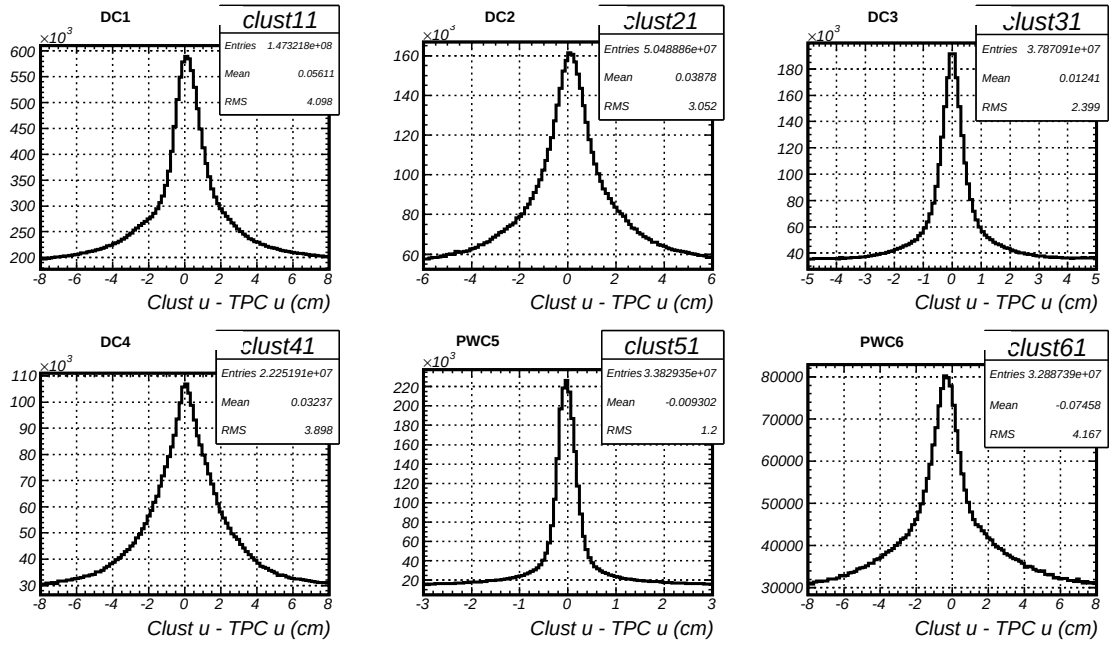

Figure 6.6: Matching of tracks at the six chambers. Notice that the x-axis scales are different.

6.5 Vertex Reconstruction

Identifying primary and decay vertices is essential for data analysis, as not only one can determine where the track came from, but also track parameters from a vertex constrained fit are more trustworthy. MIPP vertex reconstruction was split into two parts: vertex finding and vertex constrained track fitting.

6.5.1 Vertex Finding

One of the difficulties in finding vertices is the fact that beam conditions were not always clean. The algorithm that worked very well, is based on deterministic annealing filter (DAF).

Using `TMinuit`, we can fit for the point which minimizes the weighted distance squared to all tracks in the event (See Equation 6.10). The filter helps select the tracks associated with the vertex by reducing the weight of the outliers with

$$w_{DAF} = \frac{1}{1 + \exp\left(\frac{D_i^2 - R_c^2}{2T_{DAF}}\right)}, \tag{6.14}$$

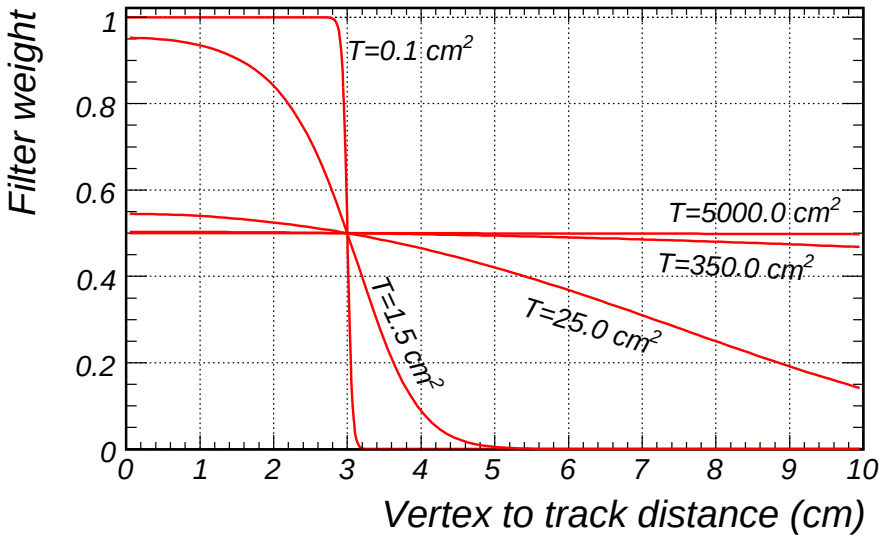

Figure 6.7: Shown are DA filter weight function for the temperatures used at MIPP.

where D_i is the distance to the track given vertex position, D_c is the filter critical radius, and T_{DAF} is the temperature. As the temperature is decreased, the weight of the outliers is reduced and the weight of the tracks with $D_i^2 < D_c^2$ is not affected. Figure 6.7 shows the weight function for the temperature schedule used by our vertex finder.

When the temperature is reduced sufficiently slowly, the filter converges on the most significant vertex even if multiple vertices exist in the event. The tracks that were included into the vertex are excluded from the available track list and the process is repeated.

In the events where the only two tracks are incoming beam track measured by the beam chambers and the same track measured by TPC and drift chambers, we found that when the temperature was lowered to 25 cm^2, it was necessary to repeat the procedure at the same temperature so that the fitted vertex position would prefer to land in the middle of the two tracks rather than exclude one of them completely.

6.5.2 Vertex Constrained Fitting

Fitting a vertex with N particles involves determining $3(N+1)$ parameters: vertex position (x_v, y_v, z_v), and track direction and momenta $(dx_i/dz, dy_i/dz; q/p_i)$. Template track fitting can be easily linearized for all parameters except z_v if the template coefficients are fairly constant as a function of x_v and y_v. Following conventions set in Equations 6.1

and 6.7, we now write vertex χ^2_v as

$$\chi^2_{vtx} = \sum_{i=1}^{N}\sum_{j=1}^{n_i} w_{ij}\left\{\left[x_v + \frac{dx_i}{dz}(z_{ij}-z_v) + Q_i\lambda_{x,i}(z_{ij})\right]\cos\theta_{ij} - \left[y_v + \frac{dy_i}{dz}(z_{ij}-z_v) + Q_i\lambda_{y,i}(z_{ij})\right]\sin\theta_{ij} - u_{ij}\right\}^2. \tag{6.15}$$

Here N is the total number of tracks in the vertex and n_i is the number of measurements associated with i-th track. It is the product of z_v and dx_i/dz that prevents us from being able to linearize the fit for z_v. With z_v held fixed, our solution must satisfy:

$$0 = \frac{\partial}{\partial p_i}\chi^2_{vtx} = \mathbf{M}\vec{p} - \vec{v}. \tag{6.16}$$

If we define a vector of constants, like in Equation 6.9

$$\vec{c}_{ij} = \begin{pmatrix} \cos\theta_{ij} \\ -\sin\theta_{ij} \\ (z_{ij}-z_v)\cos\theta_{ij} \\ -(z_{ij}-z_v)\cos\theta_{ij} \\ \lambda_{x,i}(z_{ij})\cos\theta_{ij} - \lambda_{y,i}(z_{ij})\sin\theta_{ij} - \end{pmatrix},$$

then

$$\vec{p} = \begin{pmatrix} x_v \\ y_v \\ dx_1/dz \\ dy_1/dz \\ Q_1 \\ . \\ . \\ dx_N/dz \\ dy_N/dz \\ Q_N \end{pmatrix} \qquad \vec{v} = \begin{pmatrix} \sum_{ij} w_{ij}u_{ij}c_{1,ij} \\ \sum_{ij} w_{ij}u_{ij}c_{2,ij} \\ \sum_{j} w_{1j}u_{1j}c_{3,1j} \\ \sum_{j} w_{1j}u_{1j}c_{4,1j} \\ \sum_{j} w_{1j}u_{1j}c_{5,1j} \\ . \\ . \\ \sum_{j} w_{Nj}u_{Nj}c_{3,Nj} \\ \sum_{j} w_{Nj}u_{Nj}c_{4,Nj} \\ \sum_{j} w_{Nj}u_{Nj}c_{5,Nj} \end{pmatrix} \qquad \mathbf{M} = \begin{pmatrix} \mathbf{A}_0 & \mathbf{A}_1 & .... & \mathbf{A}_N \\ \mathbf{A}_1^T & \mathbf{B}_1 & 0 & 0 & 0 \\ ... & 0 & ..... & & \\ ..... & & & & \\ \mathbf{A}_N^T & 0 & \cdot & 0 & \mathbf{B}_N \end{pmatrix}. \tag{6.17}$$

Symmetric matrix $\mathbf{M}$ is made up of the following matrices:

$$\mathbf{A}_0 = \begin{pmatrix} \sum_{ij} w_{ij} c_{1,ij}^2 & \sum_{ij} w_{ij} c_{1,ij} c_{2,ij} \\ \sum_{ij} w_{ij} c_{1,ij} c_{2,ij} & \sum_{ij} w_{ij} c_{2,ij}^2 \end{pmatrix},$$

$$\mathbf{A}_i = \begin{pmatrix} \sum_j w_{ij} c_{1,ij} c_{3,ij} & \sum_j w_{ij} c_{1,ij} c_{4,ij} & \sum_j w_{ij} c_{1,ij} c_{5,ij} \\ \sum_j w_{ij} c_{2,ij} c_{3,ij} & \sum_j w_{ij} c_{2,ij} c_{4,ij} & \sum_j w_{ij} c_{2,ij} c_{5,ij} \end{pmatrix},$$

$$\mathbf{B}_i = \begin{pmatrix} \sum_j w_{ij} c_{3,ij} c_{3,ij} & \sum_j w_{ij} c_{3,ij} c_{4,ij} & \sum_j w_{ij} c_{3,ij} c_{5,ij} \\ \sum_j w_{ij} c_{4,ij} c_{3,ij} & \sum_j w_{ij} c_{4,ij} c_{4,ij} & \sum_j w_{ij} c_{4,ij} c_{5,ij} \\ \sum_j w_{ij} c_{5,ij} c_{3,ij} & \sum_j w_{ij} c_{5,ij} c_{4,ij} & \sum_j w_{ij} c_{5,ij} c_{5,ij} \end{pmatrix},$$

and $\mathbf{A}_i^T$ is the transpose of $\mathbf{A}_i$.

Thus, the solution to vertex position is given by

$$\vec{p} = \mathbf{M}^{-1} \vec{v}.$$

In order to determine z_v, we scan around the seed value of the vertex, and compute z_v and error on z_v from parabolic fit to the 5 points around the minimum. In practice, since the track template coefficients do change with vertex location, until the computed minimum is close enough to the z-coordinate where template coefficients were evaluated, we continue the scan with template coefficients re-evaluated at the new minimum. Most vertex z positions returned by DA filter vertex finder are sufficiently good, so that only one scan is required to fit vertex z.

6.5.3 Fixing Track Momentum in Vertex Fit

Central momentum of beam tracks can be measured very well, and typical spread in momentum is a few percent, therefore in vertex-constrained fits, momentum of beam tracks should not be varied. The algorithm outlined above is easily modified to fix momentum of one ore more tracks by changing matrices $\mathbf{A}_i$ and $\mathbf{B}_i$ to

$$\mathbf{A}_i = \begin{pmatrix} \sum_j w_{ij} c_{1,ij} c_{3,ij} & \sum_j w_{ij} c_{1,ij} c_{4,ij} \\ \sum_j w_{ij} c_{2,ij} c_{3,ij} & \sum_j w_{ij} c_{2,ij} c_{4,ij} \end{pmatrix},$$

$$\mathbf{B}_i = \begin{pmatrix} \sum_j w_{ij} c_{3,ij} c_{3,ij} & \sum_j w_{ij} c_{3,ij} c_{4,ij} \\ \sum_j w_{ij} c_{4,ij} c_{3,ij} & \sum_j w_{ij} c_{4,ij} c_{4,ij} \end{pmatrix},$$

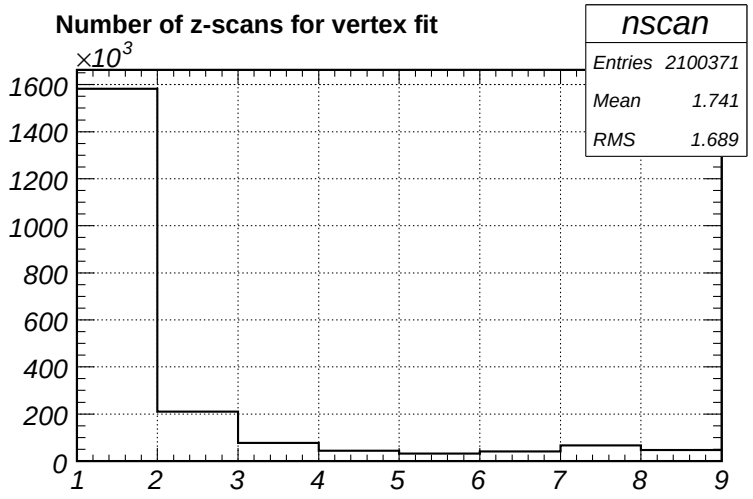

Figure 6.8: Number of z scans required for a vertex constrained fit.

and replacing the relevant part of vector $\vec{v}$ with

$$v_i = \begin{pmatrix} \sum_j w_{1j}(u_{ij} - Q_i c_{5,ij}) c_{3,ij} \\ \sum_j w_{1j}(u_{ij} - Q_i c_{5,ij}) c_{4,ij} \end{pmatrix}.$$

Otherwise, no changes to the algorithm are required.

6.5.4 Limitations of Vertex Fitting

Vertex finder clusters tracks within ± 3 cm of the vertex position. This means that nearby secondary vertices may get erroneously pulled into the primary vertex. The two problems that arise is the pull on vertex position that the incorrect tracks will have and the incorrect conclusion that the extra particles come from the vertex rather from a neutral decay.

Current implementation of vertex fitter splits the vertex only to require that the RMS of track times (as measured by drift chamber wire hits) is below 20 ns. This cleans up pileup, but does not do anything to tracks otherwise incorrectly associated to a vertex.

6 mm resolution of vertex z (see Figure 6.9 is inferior to ≈ 2 mm resolution that was obtained by BNL E910 experiment. The primary reason is thought to be imperfect understanding of distortion corrections due to non-uniform magnetic field. Uniformity of

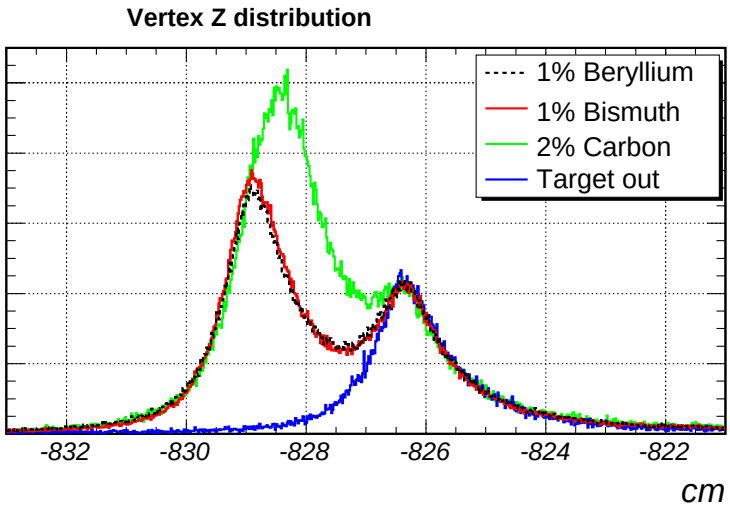

Figure 6.9: Shown are distribution of fitted vertex z from three different targets and target out configuration. The histograms were normalized to have the same height of the interaction counter. Excluding the long tails, resolution is approximately 6 mm.

magnetic field in E910 was significantly better so that corrections of order millimeter were required[36]. In practice, poor vertex resolution in z makes target out subtraction somewhat more important for differential cross section measurement, but does not have a large effect on the analysis presented here.

6.6 Particle Identification

Particle identification is done using different detector, depending on the track momentum. For particles under 1 GeV/c , energy loss in the TPC can discriminate between different species. Time of flight wall was designed to work for particles with momentum up to 3 GeV/c . Threshold Cherenkov can identify particles with momentum up to around 17 GeV/c . Finally, above 20 GeV/c , only RICH is able to discriminate different species. Since this work is focused on high momentum end of the spectrum, reconstruction algorithm of the RICH is described here.

6.6.1 Particle Identification Methods

Given a track that passes through the RICH radiator volume, there are two approaches to determining the particle ID:

1. Calculate the ring radius and convert radius and track momentum into particle mass;

2. Calculate the likelihood for electron, muon, pion, kaon, proton hypotheses and select ID of the hypothesis with the largest likelihood.

For most momenta of interest, the two approaches give identical results, as one would expect by looking at Figure 6.17. The first method has the advantage of being fast, but it does not take the dispersion of radiator gas into account. The second method is slower, but has the capability of improving separation at high momenta where the difference between π/K/p Cherenkov angles is less than the thickness of the ring. However, this improvement can only be obtained when the detector is very well calibrated. This work is based on calculation of ring radii, and is adequate for momenta where pion and kaon statistics is significant.

6.6.2 Fitting Ring Radius

The algorithm to fit ring radii is based on deterministic annealing filter (DAF) coupled to hit sharing algorithm used in HERA-B RICH [37].

While the algorithm does not take the effect of dispersion of CO_2 in detail, the RMS width of the ring as a function of ring radius is taken into account. Figure 6.10 shows that RMS of the light distribution can be modeled by a simple function for $r > 9$ cm:

$$\sigma(r) = C \cdot (r)^{-a}, \tag{6.18}$$

where $C = 23.78$ and $a = 1.044$ give $\sigma(r)$ and r in cm. For $r \lesssim 9$ cm, the number of photoelectrons starts dropping as the photons for higher wavelengths go below Cherenkov threshold. In order to allow the algorithm to converge to radius below 9 cm, the width associated with the ring was modeled as

$$\sigma(r) = \begin{cases} C \cdot r_{crit}^{-a}, & r \leq r_{crit} \\ C \cdot r^{-a}, & r > r_{crit} \end{cases} \tag{6.19}$$

r_{crit} was chosen to be 8 cm for reasons explained in Section 6.6.4.

Looking at the index of refraction and PMT efficiency as a function of wavelength of light, one cannot expect that the function of expected photoelectrons to be Gaussian. However for simplicity, the weight of each PMT given the ring radius is taken as

$$w_i(r) = \frac{(r - r_i)^2}{\sigma^2(r)}. \tag{6.20}$$

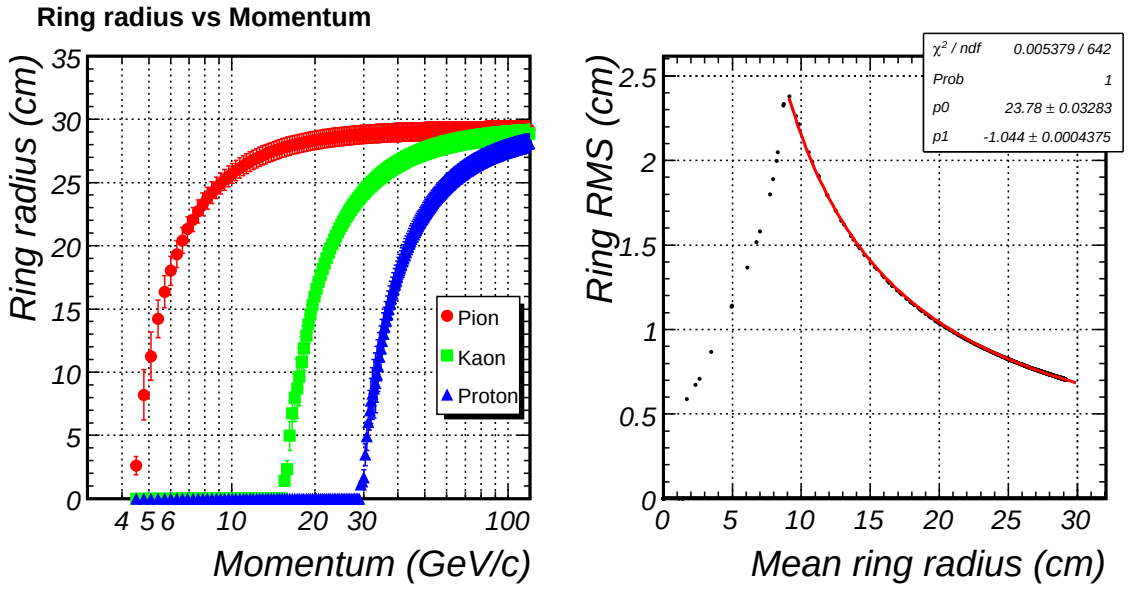

Figure 6.10: Shown are pion, kaon, and proton mean ring radii and RMS of light distribution is used as error.

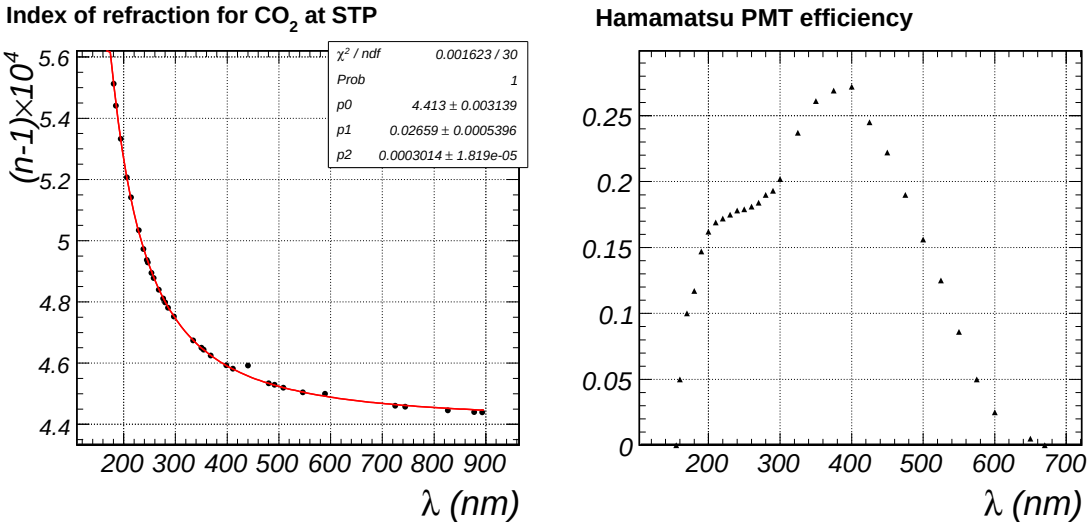

Figure 6.11: Shown are available data for CO_2 index of refraction and efficiency of Hamamatsu PMT's (efficiency shape of FEU's is similar but about a factor of 2 lower). The index of refraction is well fit by $(n-1)\cdot 10^4 = 4.413 + 2.66\cdot 10^{-2}\cdot\lambda^{-2} + 3.01\cdot 10^{-4}\cdot\lambda^{-4}$ where λ is in μm.

The first step is to select in-time track, with non-zero path length through CO_2, and predicted ring center within maximum (electron) ring radius from the PMT array. For each ring hypothesis, we compute the number of hits within the active region – defined by electron ring radius with a ~ 5 cm safety margin. Any track with less than 3 hits in the active region is dropped from the track list.

To determine the seed ring radius, we scan the minimization function for radii from 2.5 cm up to electron radius in steps of $\sigma(r)$ and select the radius with the smallest function value. To limit the effect of outliers, the weight of hits is limited to σ^2_{max}. Section 6.6.3 explains the reasons why $\sigma_{max} = 3.7$ was chosen.

Equipped with predicted ring radius, we iterate over DAF temperature cycle with the following algorithm:

1. Compute $\sigma_{max}(r)$, where r is the current guess of the ring radius. It is important not to vary σ_{max} as r changes because that forces minimization to choose smaller radius and produces slightly wider distribution.

2. Compute filter hit weight. The DAF critical radius is taken as σ^2_{max}.

3. Compute hit occupancy $o_{i;j}$ in each ring, which is defined as the number of PMT's that fall in to the same radius bin of j-th track. 0.4σ bins were used.

4. Fit each ring radius allowing ring center position to vary if at least 6 hits are associated with the ring. Each hit weight is modified as
   $w_{i;j} = w_i(r) \cdot w_{DAF} \cdot \dfrac{o_{i;j}}{\sum_j o_{i;j}}$,
   thus the total weight of each hit is 1, but varies in different tracks so that hit sharing is taken into account.

The DAF temperature cycle of (5, 1, 0.2, 0.04) cm^2 was found to work well even in busy events. At the end of the cycle, hit usage was computed with 0 cm^2 DAF critical radius where hits with weight larger than 0 were considered to be used by the algorithm. Rings that had less than 2 non-shared hits were interpreted to come from noise and were assigned $r = 0$.

6.6.3 Choosing σ_{max}

DAF critical radius parameter σ_{max} dictates the signal region for a given ring radius. There are two conflicting considerations that must be taken into account to select

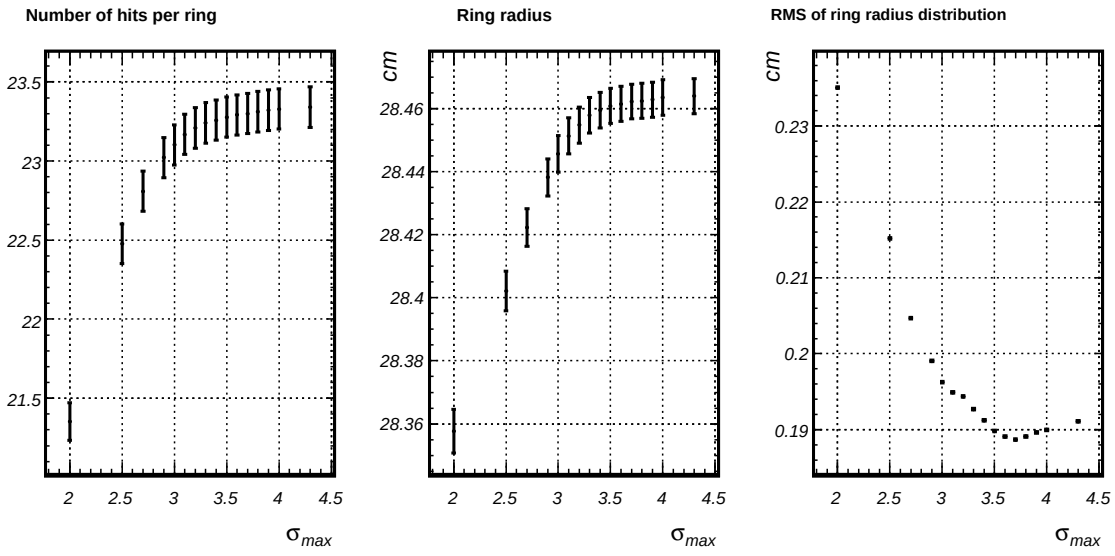

Figure 6.12: Shown are effects on the proton ring fits by different choices of σ_{max} (see text for explanation).

its value. On the one hand, the region should be sufficiently large to include all hits that come from the ring. On the other hand, very large σ_{max} will be more susceptible to noise.

Figure 6.12 shows how proton ring fits are affected by the choice of ring signal region. We see that smaller values of σ_{max} prevents the algorithm from using all of the available information for the ring fit, resulting in fewer hits on a ring, smaller radius, and larger width of ring distribution. As σ_{max} is pushed past 3.7, the potential for picking up noise is higher, resulting in somewhat larger width of the proton ring distribution.

6.6.4 Incorrectly Fit Rings

A feature of the algorithm is that it will preferentially go for hits inside the signal region, whether those hits were generated by noise or particle Cherenkov light. There are two predictable ways in which the algorithm will incorrectly fit a ring

1. Shift ring center far away from predicted position;

2. Fit maximally allowed ring radius, well above electron ring radius.

Minimization was done with limits on ring radius and center displacement from track prediction. In the case of ring center shift, a momentum dependent window was

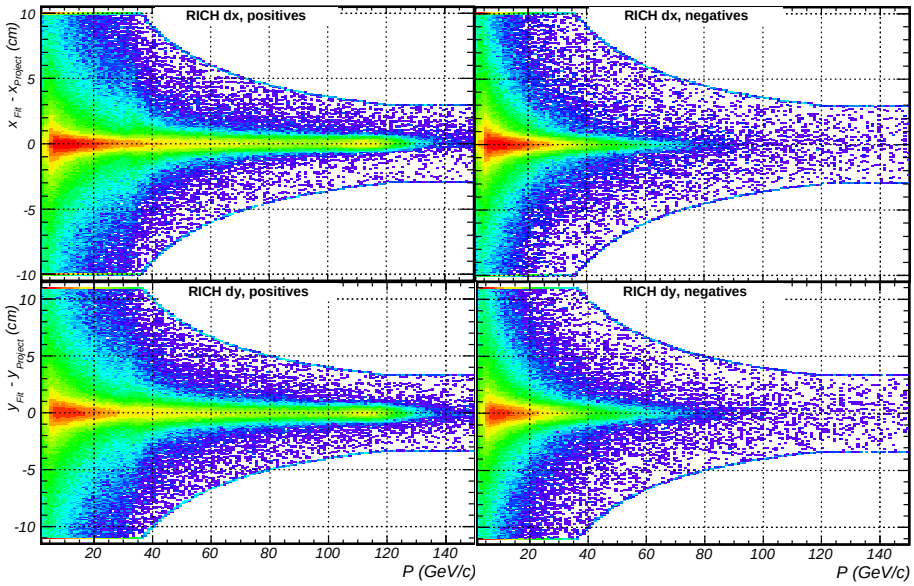

Figure 6.13: Shown are distributions of ring center displacement in x and y by the fit from the prediction made by incoming track.

chosen with

$$D_{x,y} = \begin{cases} C_{x,y}/p_{tot}, & p_{tot} < 120 \\ C_{x,y}/120, & p_{tot} \geq 120 \end{cases} \tag{6.21}$$

where $C_x = 360$ cm GeV/c , $C_y = 400$ cm GeV/c , and p_{tot} is momentum of the track. The choice is motivated by effects of multiple scattering, since the track position and angle predictions are more reliable for higher momentum tracks. Finally, D_x was limited to 10 cm and D_y to 11 cm so that the ring would be less likely to "walk" into another ring potentially causing two incorrectly fit rings.

6.6.5 Corrections to Ring Radius

When the RICH was repaired after the accident, every fourth PMT column was left empty. This creates aliasing in ring fits due to regularly missing information. Effect on ring fits can be observed by scanning over pion ring radius selecting events in a narrow band of momentum so that predicted ring radius does not change by more than ± 0.1 cm. Figure 6.14 shows that observed ring radius depends on the mean value of ring radius and the x-coordinate of the ring center. The period of the sinusoidal variations is 5.5 cm – distance between four PMT columns.

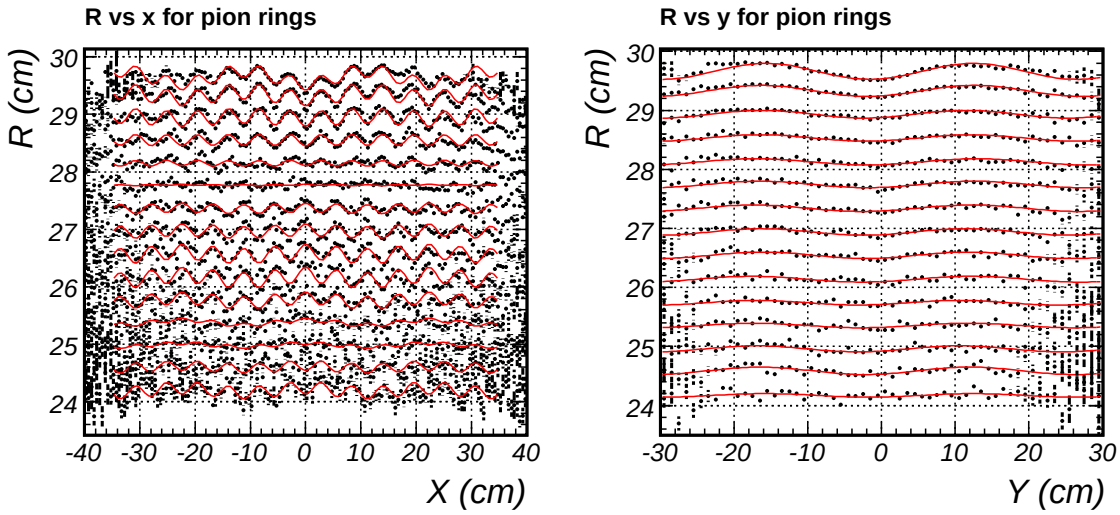

Figure 6.14: Ripples in measured RICH ring radius due to aliasing. The binned histograms shown result from scan of pion rings in 4 mm steps of central ring radius.

These ripples in measured radius can be parametrized through

$$\delta R_x(x,R) = A_{x0}(R)\cos\left(\omega_x x\right) + A_{x4}(R)\cos\left(\frac{\omega x}{4}\right), \tag{6.22}$$

$$\delta R_y(y,R) = A_y(R)\cos\left(\omega_y y + \phi\right). \tag{6.23}$$

Lower frequency corrections in x as well as correction in y result from systematic difference in ring radius as a portion of the ring is no longer detected by photomultipliers as the ring center shifts away from the center of the PMT array. As Figure 6.15 shows, when we do that we find that the amplitude $A_{x0}(R)$ is well described by $A_0 sin(\omega R)$. This corroborates the statement that ripples result from geometric aliasing.

Ripple corrections are most important for high radius rings when at high momenta the difference in ring radii between protons, kaons, and pions becomes small. Figure 6.16 shows that for high momentum pions the effect is a $\sim 10\%$ improvement in the RMS of ring distribution.

6.6.6 Particle Identification from Ring Radius

For a Cherenkov photon in a gas with index of refraction n, the angle at which photon is emitted by a particle with speed β is given by

$$\frac{1}{2}\theta^2 = 1 - \frac{1}{n\beta}. \tag{6.24}$$

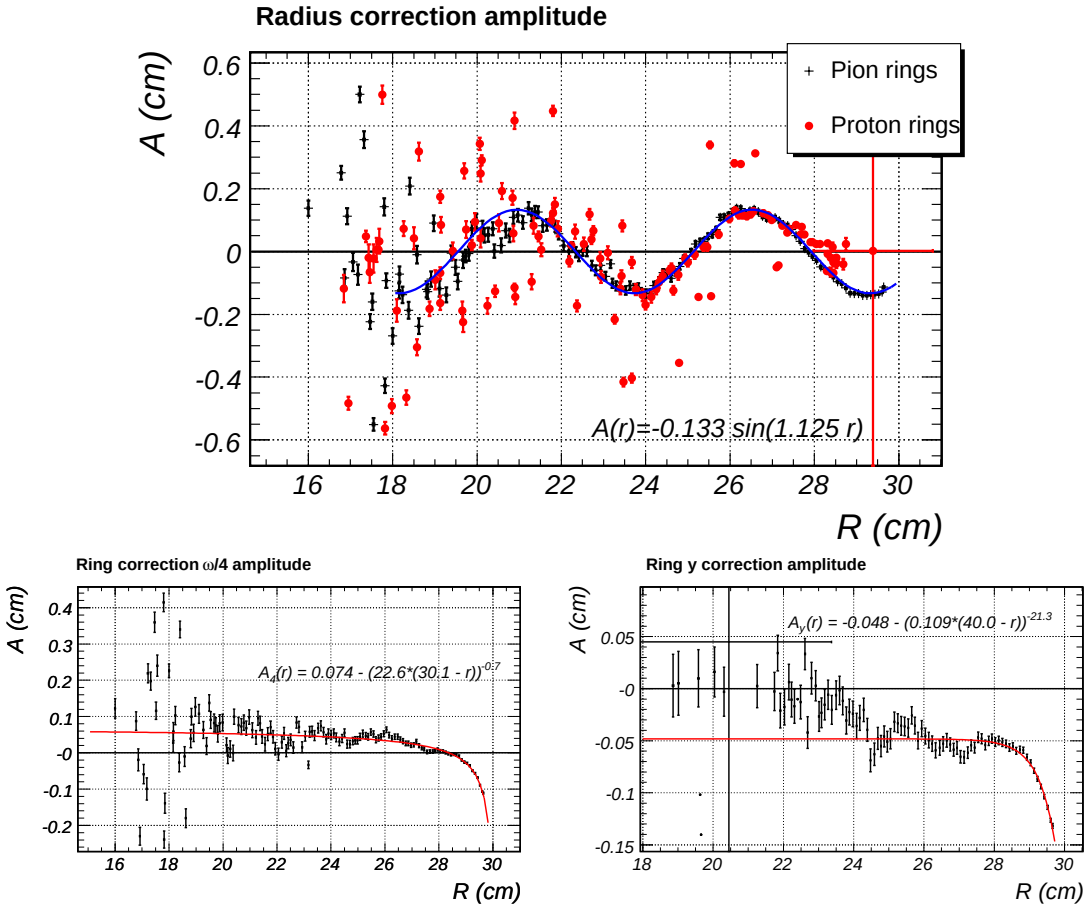

Figure 6.15: Results of fits to amplitude of ring radius ripples as a function of central ring radius. As a sanity check, the scan was repeated for proton rings to verify that the effect is not specific to pion rings. The fact that amplitude of the dominant oscillation in x is consistent with $\sin(\omega_x R)$ confirms that the effect is purely geometric.

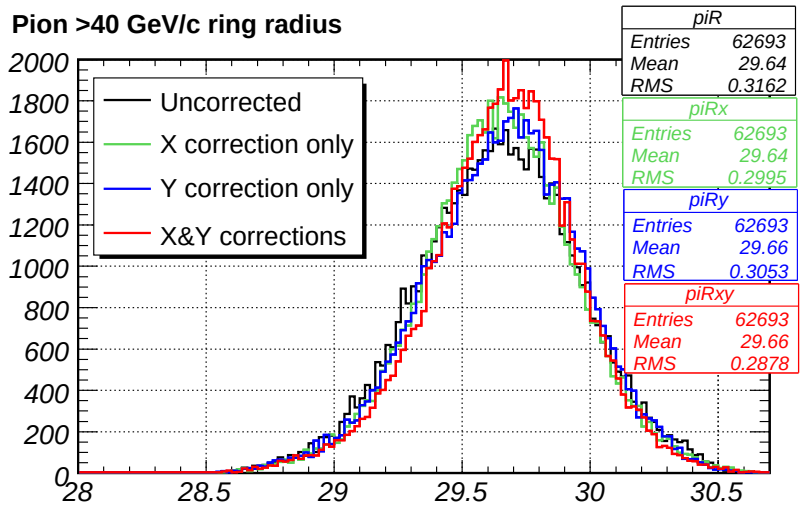

Figure 6.16: A 10% improvement in radius width of high momentum pions is obtained by removing ripple corrections through parametrized equations.

We can define θ_0 as the maximum opening angle, when $\beta = 1$. Then

$$\frac{1}{2}\theta_0^2 = 1 - \frac{1}{n}.$$

From equation of relativistic momentum $p = m\gamma\beta$, we get

$$m^2 = p^2\left[\frac{1}{\beta^2} - 1\right] = p^2\left[\left(\frac{1 - \frac{1}{2}\theta^2}{1 - \frac{1}{2}\theta_0^2}\right)^2 - 1\right] = p^2\left[\left(\frac{F^2 - \frac{1}{2}R^2}{F^2 - \frac{1}{2}R_0^2}\right)^2 - 1\right], \tag{6.25}$$

where $F = 990$ cm is the focal length of RICH mirrors, and R_0 is the ring radius of $\beta = 1$ particle. Given the fact that $n \approx 1 + 4.5 \cdot 10^{-4}$ in CO_2 at STP, $\theta_0^2 \approx 9 \cdot 10^{-4}$. Equation 6.25 can then be approximated to better than one part in a thousand by

$$m^2 = p^2\frac{R_0^2 - R^2}{F^2}, \tag{6.26}$$

which is handy to get a feel for behavior of the ring radius on momentum. Using equation 6.25 we can then transform R vs p plot into a more useful m^2 vs p plot, which can be used for an analysis.

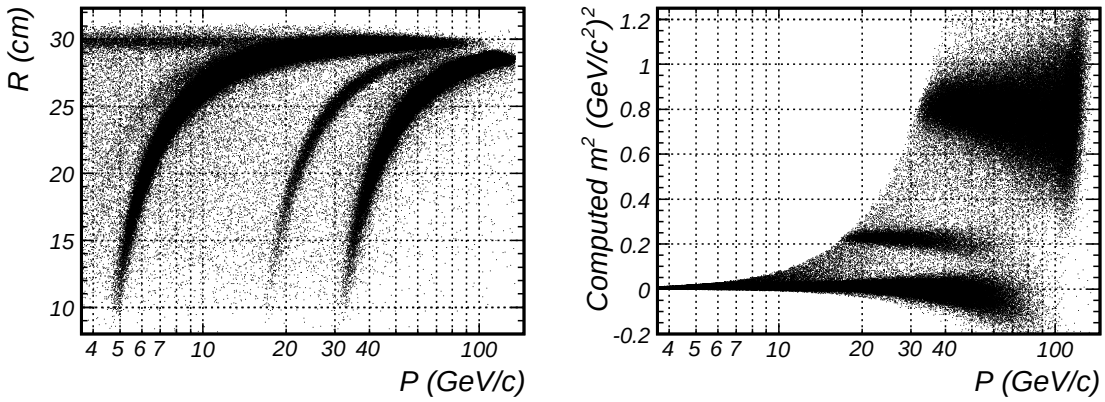

Figure 6.17: Shown is distribution of RICH ring radii in 120 GeV/c interactions (left) and the same plot where mass squared is computed using Equation 6.26.

Chapter 7

Detector Calibration and Alignment

Good detector calibration is essential for reconstruction algorithms to work well. We were calibrating different parts of the spectrometer in multiple passes, each subsequent pass depended on constants generated in the previous passes.

In the first pass, we performed calibration of systems that did not require tracking: ADC pedestals, event trigger time, time offsets of drift chamber wires, hot channels in the RICH and wire chambers.

With calibrated drift chamber time offsets, reconstruction was able to improve signal to noise ratio, and we were able to align wire chambers, and later align other subsystems (TPC, RICH, calorimeters) to the chambers.

7.1 Event Time

Good event time is critical to performance of the TOF wall and Kp-separation in 5 GeV/c beam. In order to have 3-sigma Kp-separation out to 3 GeV/c , one needs 200 ps resolution on time difference measurement (see Figure 7.1).

One of the complications in calibration of T0 counters is temperature dependence of the time offset, requiring time-dependent offset for each channel. Figure 7.2 shows an example of an overnight run where the delay cables drifted by about 1 ns with respect to event trigger. It is evident that just one offset per channel per run (or subrun) is insufficient since desired resolution is 200 ps.

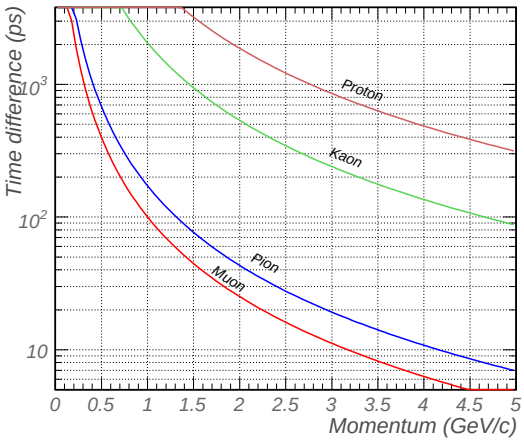

Figure 7.1: Time of flight difference from $\beta = 1$ particle for a straight line particle from the target to time of flight wall.

We represented the offset of each channel as a third degree polynomial for each subrun (typically about 5000 events). Coefficients of polynomials were calculated using the following algorithm.

1. Calculate pedestals.
2. Determine TDC offset for every PMT and trigger bit.
   - Different trigger bits were timed in to a nanosecond or so, which is good for trigger system, but the offsets are comparable to the effect we want to correct.
3. TDC offset of the trigger bit with the largest number of entries is chosen as a reference and relative trigger bits are computed for each counter (group of 4 PMT's).
4. Partition data into bursts. Each burst contains at least 80 triggers (if possible) and lasts no more than 10 minutes.
   - Data is first split into spills, and then spills with less than 80 events are merged with adjacent spills unless the burst would become too long.
   - Average time (seconds since Jan 1, 1970) is computed for each burst.
5. For each burst, TDC distribution of every channel is fitted to a Gaussian, and the mean and the error on the mean are saved.

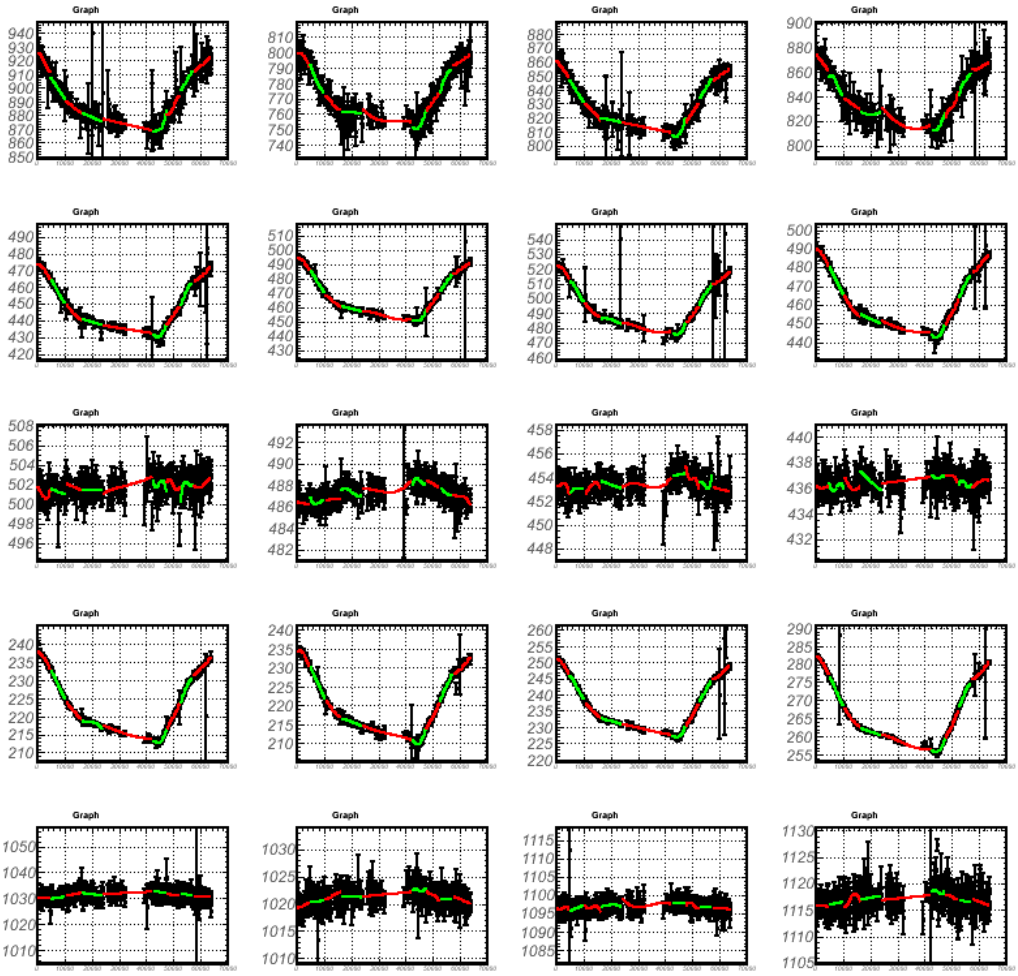

Figure 7.2: Variations in T0 counters timing offset for an overnight run and superimposed correction curves for every subrun. Each of the five columns shows distribution for the four PMT's that belong to the counter and set of cables. From top to bottom, the rows correspond to T00-ribbon, T01-ribbon, T01-RG8, TBD-ribbon, T00-RG8. TDC counts are plotted on the vertical axis, with 60 ns per bin for TBD-ribbon, and 30 ns per bin for all other counters.

6. The distribution of TDC offsets of every channel is fitted to a third degree polynomial.

7. Steps 2 and 3 are redone using the fits from step 6. Then the final fits (steps 5 and 6) are obtained and results are stored into the database.

The second correction that is applied to TDC signals is time slewing from the amount of charge that creates the signal. Figure 7.3 shows that there is a systematic dependence of PMT hit time on the amount of charge that the PMT collected. Time-slewing correction was computed with the following algorithm:

1. Pedestal-subtracted ADC spectrum is fitted to Landau for each channel.

2. Entries between 0.5 and 2.5 of Landau MPV are used to make a graph for every channel. Entries get sorted by $1/\sqrt{ADC}$, and TDC distribution of at least 40 entries is fitted to a Gaussian, and is saved along with the average $1/sqrtADC$.

   - The rationale for limiting the range of ADC signals is to avoid over-correcting very small signals, and limit the impact of pileup on high-ADC events.

3. Distribution for each channel is fitted to a parabola.

4. To ensure that the TDC distribution is centered at 0 once all corrections are applied, an overall offset for each channel is calculated with the temperature and ADC correction taken into account before results are saved into the database.

Results of these corrections give 120 ps resolution for T01-TBD time difference (see Figure 7.4, which is sufficient for both TOF wall and beam time of flight at low momenta.

7.2 Drift Chamber Time Offsets

Between the drift chamber electronics and difference in cable length, time offset had to be calculated for each wire. In addition, there were systematic shifts from run to run, thus effectively we needed a constant for each wire and run. Of course, no single run had enough statistics to determine the offset for each wire, so we used the following approach to compute time offsets (t_0's).

1. In each run we attempt to determine t_0 for wires which have enough statistics;

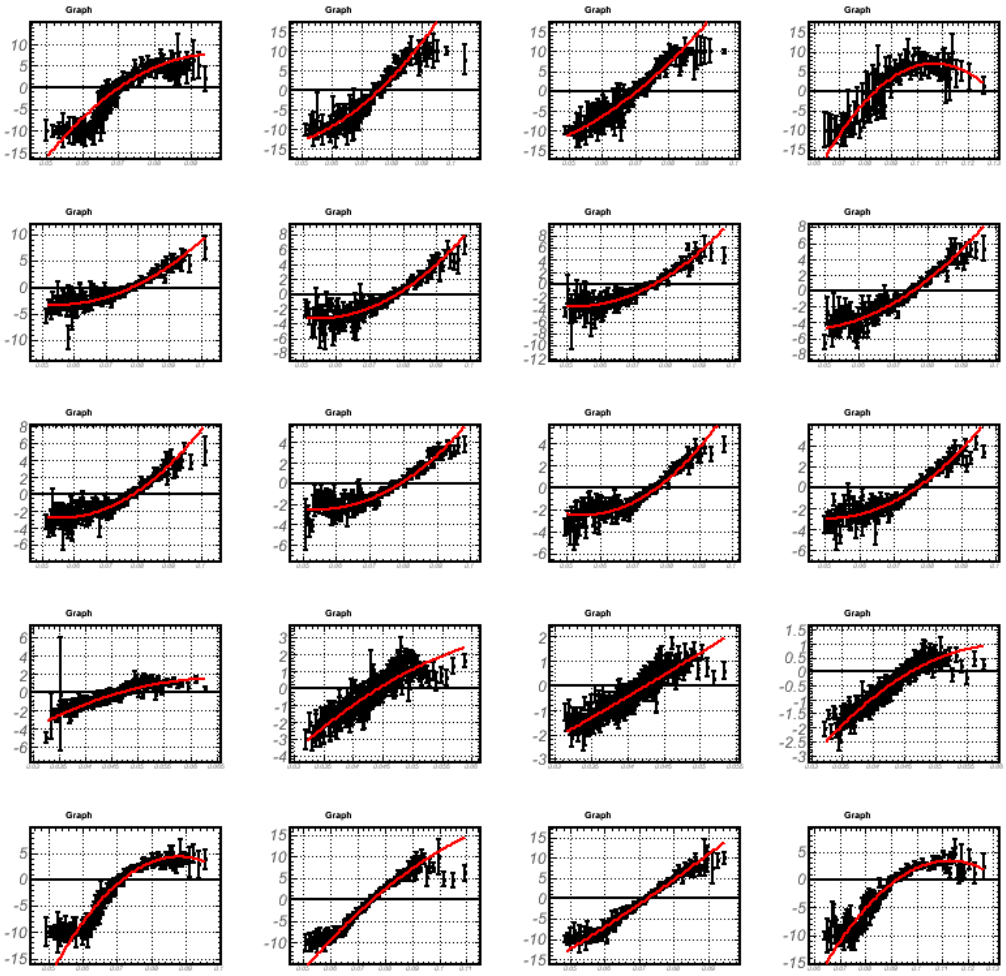

Figure 7.3: Plotted are TDC after temperature correction versus $1/\sqrt{ADC}$ and superimposed quadratic fits. The five columns are identical to those in Figure 7.2.

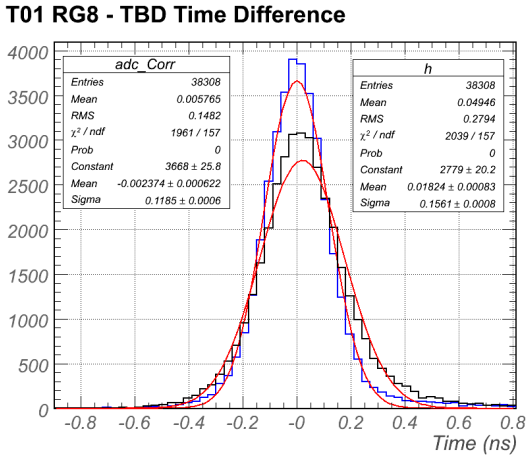

Figure 7.4: Shown is the reconstructed time difference between T01 and TBD counters with (blue curve) and without (black curve) ADC correction. Time slewing correction improves the resolution by more than 25 %, so it is worthwhile to apply it.

2. For each run where at least 3 wires were fit, we compute the average $t_{0,run}$ for the run;

3. For every wire in the runs which have the run offset computed, we compute overall offset for the wire ($t_{0,wire}$ by shifting entries from different runs by $t_{0,run}$.

4. For every run, we use wires with valid $t_{0,wire}$ to recalculate $t_{0,run}$;

5. Steps 3 and 4 are repeated three times, each subsequent iteration picks up more runs and wires;

6. For every wire in every run, time offset is set to t_0 if it was computed in step 1, otherwise it is set to $t_{0,run} + t_{0,wire}$, thus taking into account differences from run to run and from wire to wire.

7.2.1 Event Selection

Event selection is quite important in order to determine t_0's well. We attempted to limit pileup by imposing the following requirements:

- No more than two $\mathrm{T01}_{3/4}$ or $\mathrm{TBD}_{3/4}$ are allowed in the event;

- If there were two 3/4 signals in either counter, time separation between the two had to be at least 100 ns;
- If a beam chamber had more that 24 wires hit, it is ignored;
- If a drift chamber had more 150 wire hit, it is ignored.

Although a significant fraction of data was thus ignored, the signal to noise ratio was much higher than if all the available data were used. Given the fact that wires on the edge of the chamber have little signal, it was extremely important to try reject noise.

7.2.2 Fitting

Wire time distributions can be modeled quite well by a Gaussian with exponential tail, i.e.

$$f(t) = \begin{cases} A \cdot \exp\left(-\frac{1}{2}\left(\frac{t-t_{peak}}{\sigma_t}\right)^2\right), & t < t_{peak} + \sigma_{cut}\sigma_t \\ A \cdot \exp\left(\frac{1}{2}\sigma_{cut}^2 - \frac{t-t_{peak}}{\sigma_t}\sigma_{cut}\right), & t \geq t_{peak} + \sigma_{cut}\sigma_t \end{cases} \tag{7.1}$$

Here t_{peak} is the usual Gaussian peak, and σ_{cut} is a unitless parameter which determines how many sigma to the right of the peak the function becomes exponential. In this representation, the function and its derivative are continuous. After making a reasonable guess at parameters for a histogram, fitting was done through `TMinuit` minimizer package from `ROOT`, and time at half-maximum was taken as t_0.

7.3 Chamber Alignment

7.3.1 Aligning Chamber Planes

Initial chamber plane positions from the survey of the experimental hall agreed with data to within a few a few millimeters. Misalignment of chamber planes was sufficiently small, so that track finding efficiency was not affected too much, but as Figure 7.5 shows, improvement to alignment were necessary. To put matters in perspective, 120 GeV/c particle is deflected from straight line by only 1.8 cm through the length of the experiment, so a half wire spacing (1.5 mm) misalignment of PWC6 leads to a 10% systematic effect.

Alignment was split into two parts:

- Aligning beam chambers,

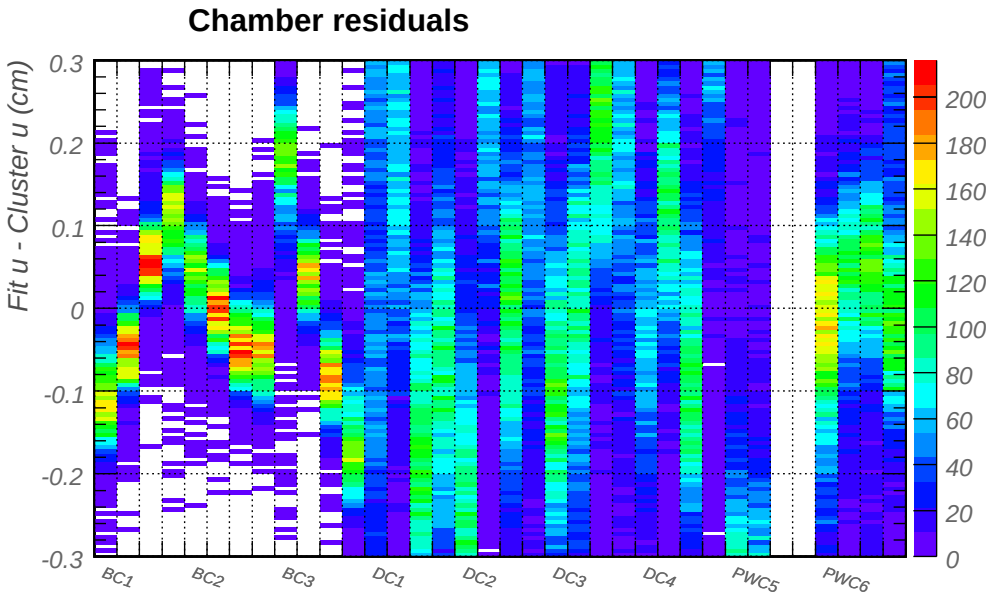

Figure 7.5: Chamber residuals before the chamber alignment was done. On the horizontal axis are chamber planes, on the vertical – residuals from 9-chamber track fits.

- Chambers 1-6 to beam chambers.

Doing alignment for beam chambers separately boosts statistics for the 3 chambers, since a good beam track is available in overwhelming majority of events. Chamber 1-6 alignment was done with 6 chamber tracks and 9-chamber beam tracks. The first set of tracks made it possible to track chamber rotations relative to one another (BCs do not have a long enough lever arm), and the second set made sure that alignment of all 9 chambers was consistent.

Track selection is crucial to successful alignment calculation. For the final pass, we selected only those tracks that passed through all 6 chambers and where at most two chamber planes were missing. Requiring almost all planes to be present provided some immunity to false positives and bias in fits due to insufficient amount of data. Unfortunately, chamber efficiency was not high enough to allow us to use only those tracks where all chamber planes were present. If a wire plane contained two hit wires, it was excluded from the fit so as to limit the impact of noise and pileup. Lastly, tracks below 4 GeV/c were rejected, because of non-negligible multiple-scattering, and the fact that energy loss for low-momentum particles was not taken into account. This requirement was not a heavy toll

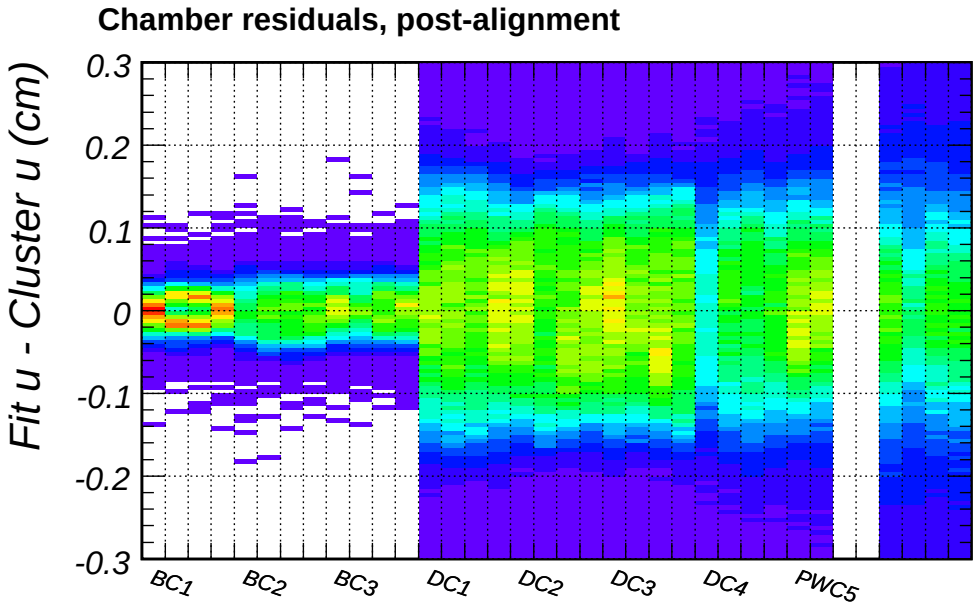

Figure 7.6: Residuals once chamber alignment was completed.

on available statistics because of poor acceptance for low-momentum particles in chamber 6.

The algorithm is quite simple. For each wire in the track we calculate unbiased residual, i.e. residual when the wire is taken out of the track fit. We compute the mean of residuals for each wire plane using all available tracks, and shift the wire plane by 0.3 of the residual. Next the track list is preened by removing those tracks where any one of residuals exceeded 1.5 wire spacing plus the absolute value of computed mean. The procedure was repeated until the largest mean of residuals was below 1% of wire spacing.

A typical run with at least 5000 tracks provided enough statistics to do reliable alignment, to monitor its stability and correlation with beam momentum.

7.3.2 Z-alignment and Rotations

A lot of effort went into verifying that chamber z-positions and rotations about z-axis are correct [26]. Since magnetic field makes track fits more uncertain, we relied upon field off data. Unfortunately, the amount of field off data is very small, so precision of field-

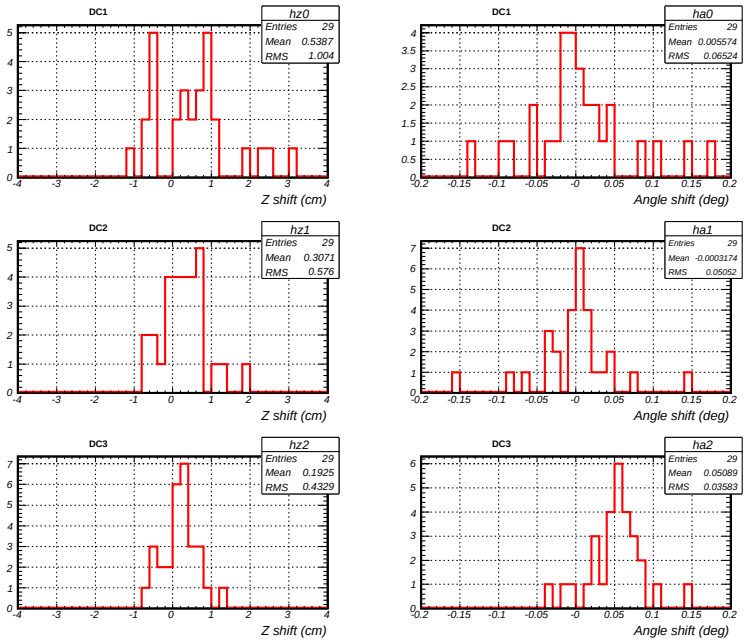

Figure 7.7: DC123 z-alignment with field off runs without known geometry errors. Still, DC3 is being systematically rotated by 0.055° by z-alignment algorithm in 29 different runs from 5 different time periods.

off alignment is limited. Nevertheless, this work helped find major errors in positioning of chambers in the experiment.

The algorithm for alignment of chambers is similar to wire plane offset: tracks were stored in memory for the entire run, and at the end minimization of the sum of χ^2 was done using `TMinuit` by shifting z of the chambers and rotating them about z-axis.

Figure 7.7 shows that even when all known errors were solved in the geometry description, DC3 appeared to have a rotation about z-axis of 0.055° (nearly 1 mrad). The effect of this rotation on the edge of the chamber is about $\frac{1}{4}$ of wire spacing, which is noticeable, so this rotation was corrected.

Figure 7.8 shows results of z-alignment algorithm re-run with DC3 rotated. Here we see that the alignment algorithm wants to move DC123 in z by 5 mm, 3 mm, and 2 mm respectively. These corrections were not applied for the following reasons:

- We cannot easily estimate effect from Earth's magnetic field and residual field in the magnets;

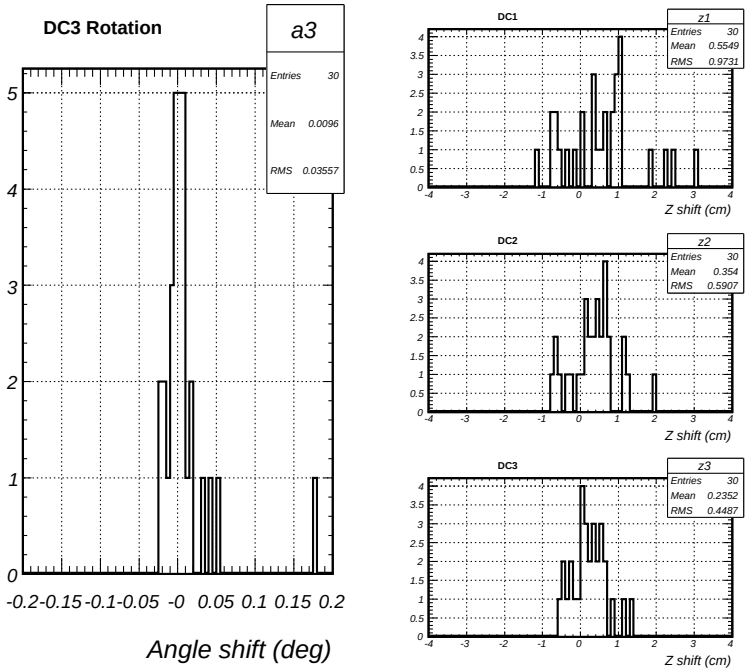

Figure 7.8: DC123 z-alignment after rotation in DC3 was removed.

- Rotation of chambers about x- and y-axes, which can shift z-position of the hit, is not taken into account by reconstruction;
- The systematic error on position measurement due to these misalignments is less than 0.1 wire spacing).

7.4 Tuning Magnetic Field

Measurement of magnetic field with Ziptrack had very small uncertainties in positions of the Hall probe jig, but due to the size of the holder, precise rotation of the probe could not be set or measured. This leaves room for dominant component to bleed into very small component and thus can be observed with data as well as magnetic field measurements.

7.4.1 B_x/B_y Rotation

Wire plane alignment of runs with different momenta showed very strong correlation of alignment constant for vertical-measuring planes of the PWCs (see Figures 7.9 and 7.10). The most likely possibility for this problem was large B_x component of the field in magnet field map.

To determine whether the dominant B_y bleeding into B_x is responsible for this correlation, we ran another track χ^2 minimization algorithm, where only 9-chamber beam tracks were used, and the algorithm was free to rotate B_x and B_y components:

$$B'_x = B_x \cos\theta + B_y \sin\theta,$$
$$B'_y = -B_x \sin\theta + B_y \cos\theta.$$

Results, shown in Figure 7.11 demonstrate that $\theta_{JGG} = \theta_{Rosie} = 0$ is not consistent with data. The large spread of the two rotation angles comes from the fact that minor wire-plane misalignment will have an enormous effect on large-momentum runs, where the minimizer will compensate for the misalignment by inflating B_x.

The two magnets' fields were measured with the same apparatus rotated by 180° about y-axis. Therefore, if the misalignment truly comes from rotation of the Ziptrack Hall probe holder, the B_x/B_y ratio in the center of the magnet (where B_x has to be vanishingly small), must be equal and opposite. Figure 7.12 clearly shows that in the case of B_x, the

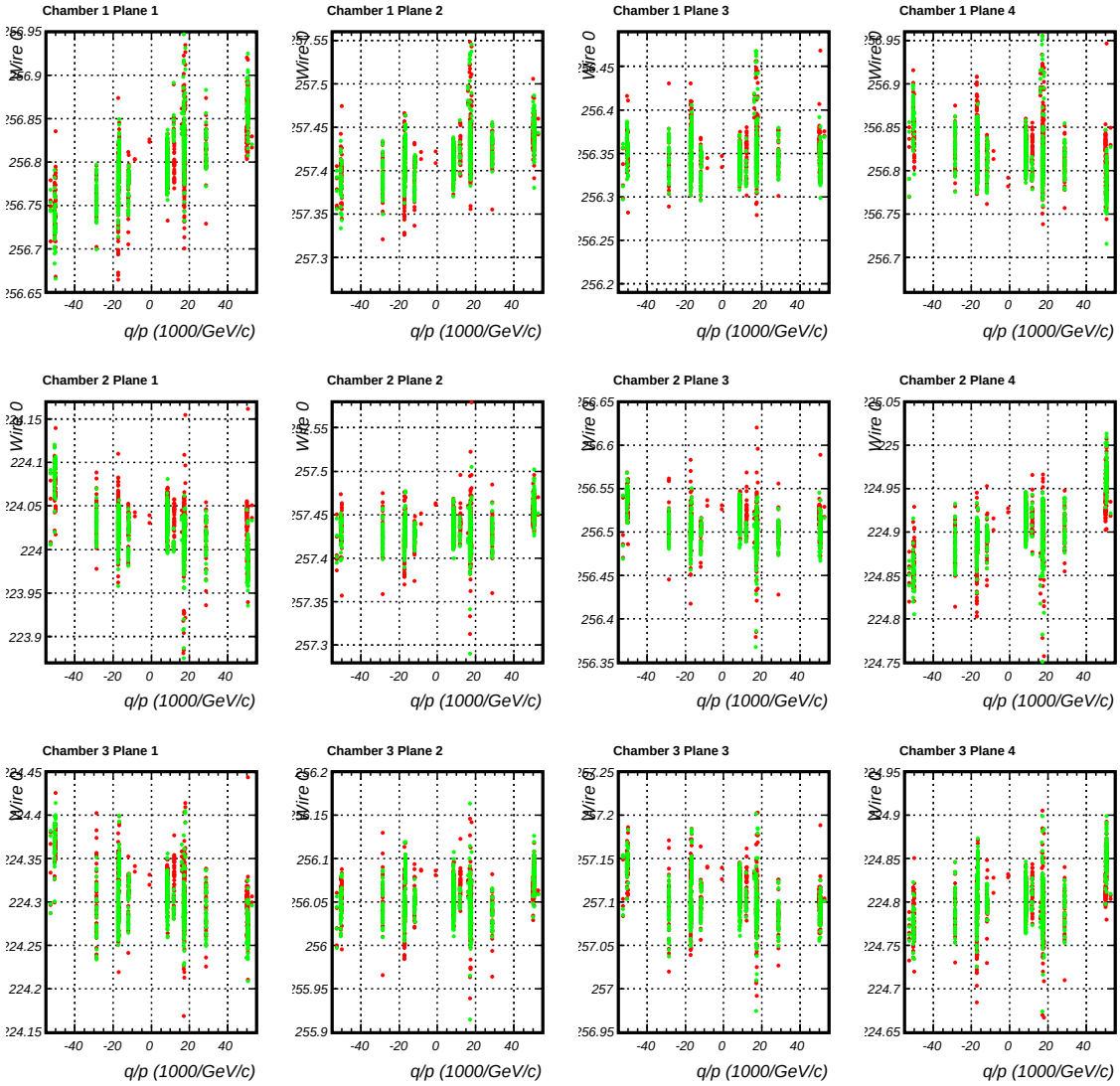

Figure 7.9: DC123 alignment results for runs with different beam momenta. Red dots come from alignment with BCs fixed, and green diamonds from alignment with BCs allowed to vary.

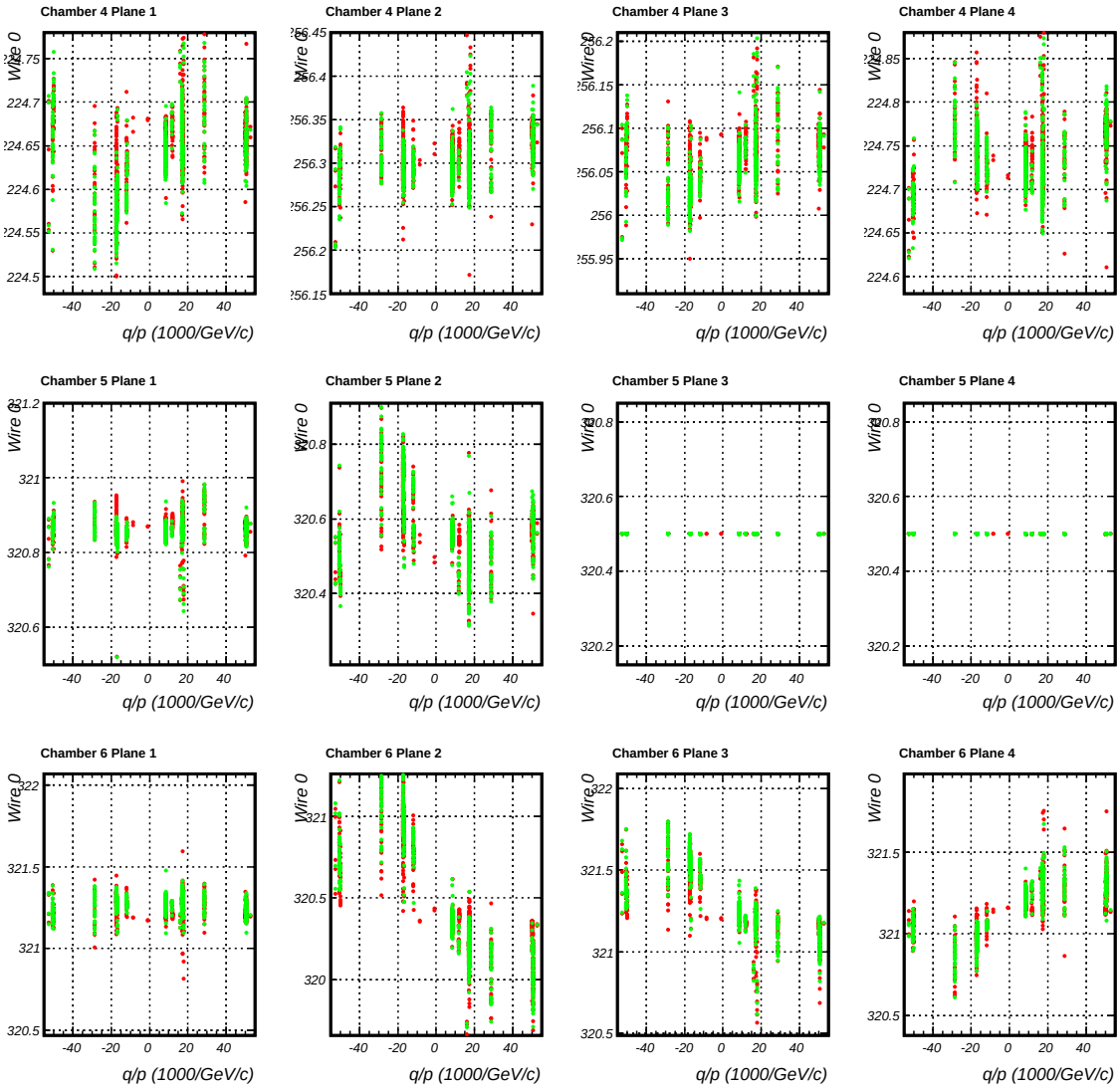

Figure 7.10: DC4 and PWC56 alignment results for runs with different beam momenta. Red dots come from alignment with BCs fixed, and green diamonds from alignment with BCs allowed to vary. Notice the large correlations of alignment offset in the second (vertical-measuring) plane of PWC5 and PWC6.

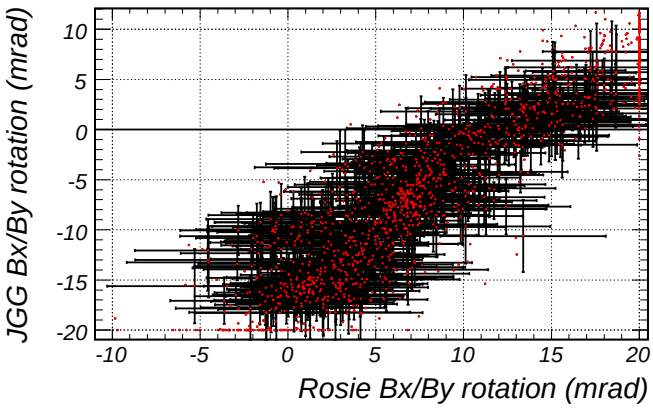

Figure 7.11: Results of optimizing B_x/B_y rotation. While the different runs are clustered in a line rather than a single point, all runs exclude rotation (0, 0) for the two magnets' field components.

ratio is about 0.7%, and in the case of B_y, the ratio is 0.3%. The point $(7, -7)$ is supported by the data, as it falls in the middle of the line in Figure 7.11, so both magnets' field map B_x/B_y components were rotated by 7 mrad in opposite directions.

7.4.2 B_y/B_z Rotation

While the experiment is not very sensitive to B_z since most track angles are small with respect to the z-axis, the Hall probe measurements do suggest a 3 mrad rotation of B_z/B_y components, which was done. The summary of chamber wire plane alignment

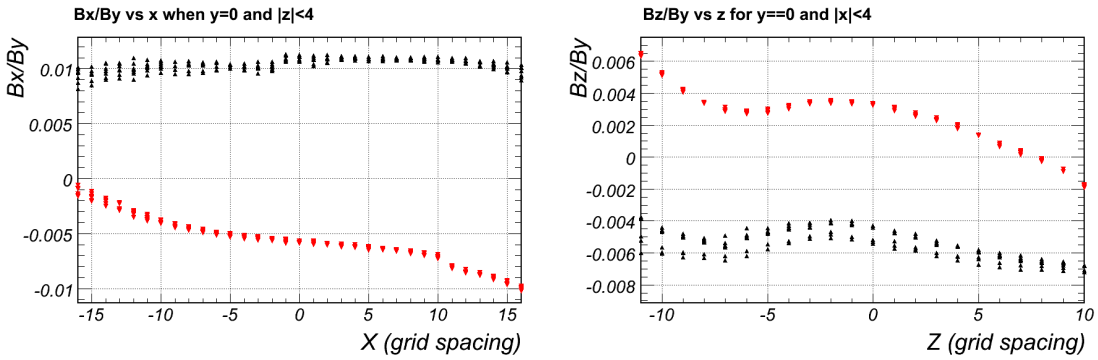

Figure 7.12: The ratios of field components in the center of the magnet. JGG is shown in up-pointing black triangles and Rosie in downward-pointing red triangles.

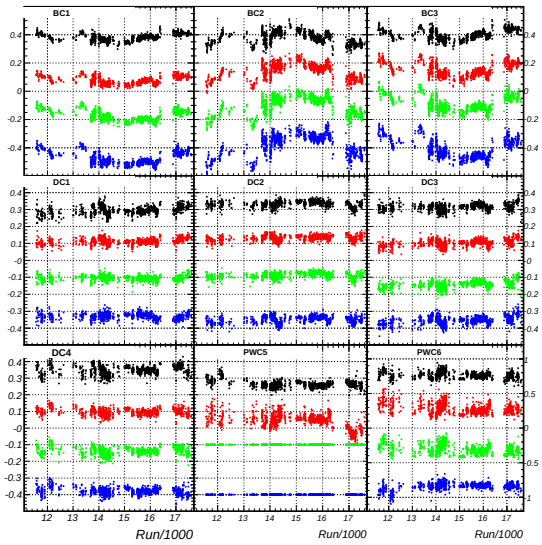

Figure 7.13: Alignment summary with geometry and magnetic field corrections. Plane 1 is at the top of every set of graphs for each chamber. Note: the y-scale of PWC6 plots is different from all other chambers.

constants with xy and yz rotations taken into account is shown in Figures 7.13 and 7.14.

7.4.3 B_x/B_z Rotation

The most difficult rotation of magnetic field components to correct is that about y-axis. B_x and B_z are comparable in most regions of the magnet, so B_x/B_z or B_z/B_x ratios of magnetic field measurements are not as convincing as is the case of B_y/B_z ratio. While tracking is not very sensitive to this rotation, TPC drift correction is. To determine the optimal rotation, the slope of TPC x-residual vs z was measured for a different values of the component rotation. Results shown in Figure 7.15 suggest that the data wants to have the components rotated by 9.6 mrad.

The ratio of magnetic field components while not convincing, favors rotation of the same magnitude (see Figure 7.16) to achieve better symmetry of the B_x/B_z ratio. Given that rotation is of the same order of magnitude as the other two rotations, and TPC is more sensitive to it than the magnetic measurements are, rotation of 9.6 mrad was applied to both JGG and Rosie.

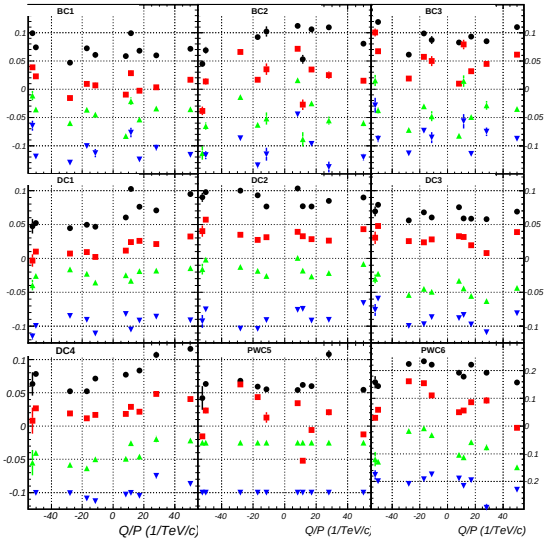

Figure 7.14: Alignment summary with geometry and magnetic field corrections. Plane 1 is at the top of every set of graphs for each chamber. While correlations with momentum still exist, they are small, and their effect on tracking can be measured. Note: the scale of PWC6 plots is different from all other chambers.

7.5 TPC Electron Drift

Understanding of electron drift in the TPC consists of two more or less independent problems. The first is measuring drift velocity in the absence of magnetic field which is equal to drift velocity when magnetic and electric fields are collinear. We call this velocity v_0. The second is drift velocity components given magnetic field and the angle between magnetic and electric fields (electric field is assumed to be constant 122 V/m). This 3-dimensional effect distorts the tracks from straight-line projection in a complicated fashion by as much as 8 cm in x and 10 cm in z. Good understanding of this effect is crucial if TPC measurements are to be trusted.

7.5.1 Measuring v_0

Drift velocity in argon-methane mixtures is a function that depends on a number of variables: fraction of methane, ratio of electric field and pressure, oxygen and water vapor contamination, and gas temperature. Measurements for clean P10 (90% Ar 10% CH_4) are shown in Figure 7.17. The choice P10 at atmospheric pressure makes dependence of drift velocity on pressure very small when electric field is about 120-150 V/cm.

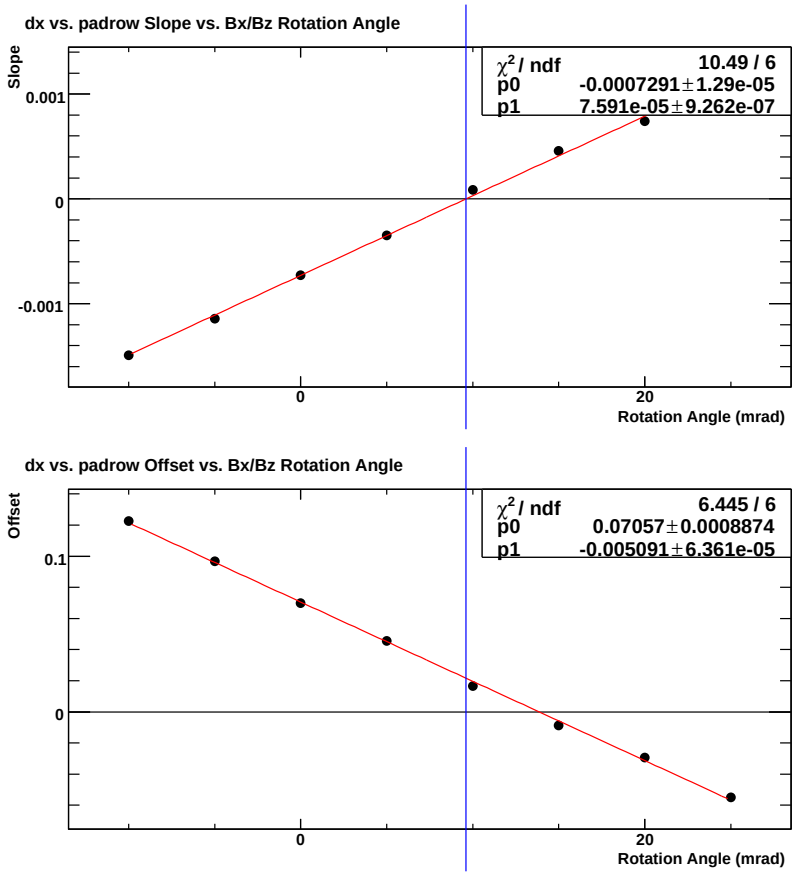

Figure 7.15: Shown is dependence of the slope of x-residual on z for different rotation of B_x/B_z components.

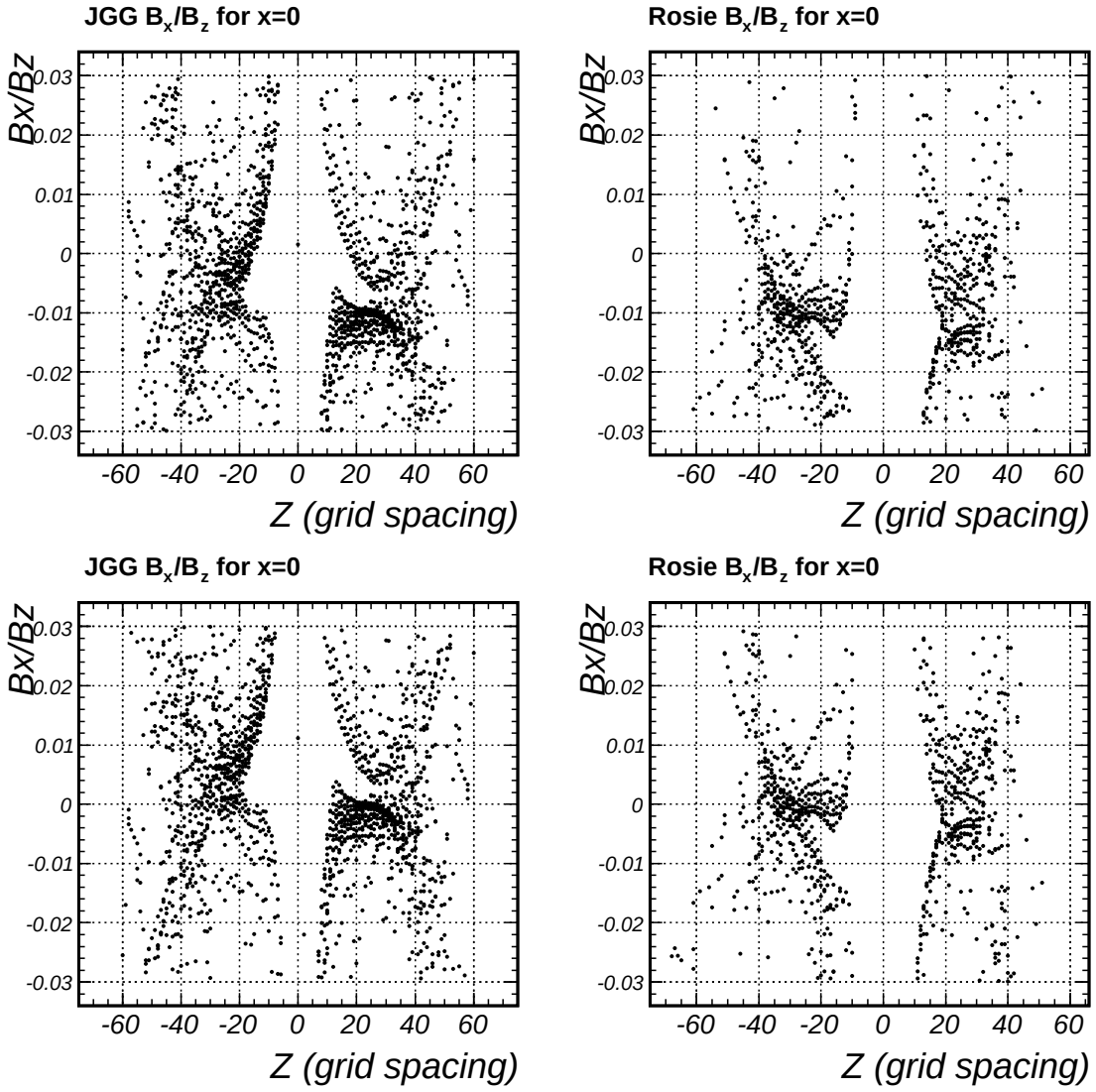

Figure 7.16: The top pair of plots shows the ratio of B_x/B_z of the two magnets for $x = 0$ in the field map. The bottom pair shows the same ratio when the field components are rotated by 9.6 mrad. Note that unlike B_x/B_y and B_z/B_y, the sign of this ratio is expected to be the same for both magnets, since the Hall probes were rotated about y-axis.

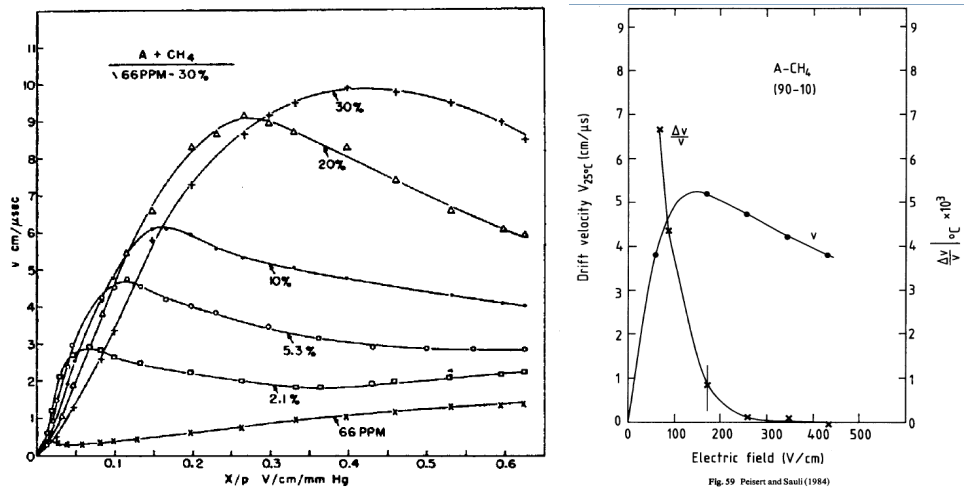

Figure 7.17: Two sets of measurements of drift velocity in P10 mixture[10, 33].

Distortions of the drift velocity in the center of the TPC are small as the field is quite uniform. This makes it possible to measure drift velocity even when magnetic field is on using reconstructed hits in the center of the TPC drift volume.

In order to remove any sort of bias from measurement of the drift velocity, we did full reconstruction of event, and then refit the vertex using information from chambers only. In order to achieve this using one value of drift velocity for all runs, the cut windows to match TPC track to chambers were quite loose. Once the vertex-constrained fit was done, we selected vertices with three or more tracks, and saved position predicted at the z of the hit and its measured time. One can take two distinct approaches to measure velocity: bin the data in t or z and do a least squared fit or do a non-linear fitting where the square of distance from the straight line to the data point is minimized. The latter method has the advantage that outliers have a smaller effect on the fitted slope, and therefore is not as sensitive to event selection as the former method.

One of the unknowns in the system is trigger delay time which should be constant from run to run. Figure 7.18 shows the measured trigger offset as a function of run. There are some notable features in the plot:

- Runs before 12700 have a systematically different trigger delay. Between runs 12700 and 13000, a lot of work on the trigger was done in the hall, so while we do not know how much the trigger time was changed, the data suggests a 70 ns difference.

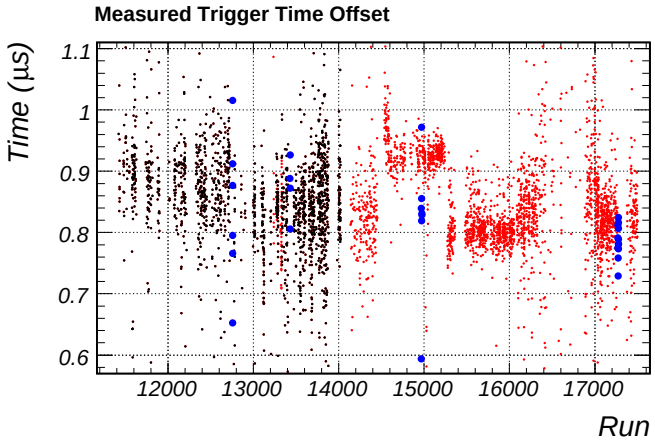

Figure 7.18: Measured TPC trigger delay time as a function of run. Large blue circles come from field off runs. See text for further explanation.

- NuMI runs (14500-15250) measure a different trigger delay. This is not very surprising, because NuMI events are very busy and therefore wide windows to match TPC tracks to chamber data may have an adverse effect.

- Field off data gives approximately the same delay as field on data, which is a confirmation that the effect of the magnetic field on the drift velocity in the center of the TPC is negligible.

- Runs before 14100 were taken with a larger gating grid delay, which limited the active volume of the TPC. Reduction of the gating grid delay did not affect trigger delay.

With these results, we fix the delay to 875 ns for runs before 12700 and to 800 ns for runs above 12700. Then we go back to the data to measure drift velocity with constant trigger delay. Figure 7.19 shows the measured drift velocity when trigger offset is free, and when it is fixed.

Computed drift velocity varies smoothly with run number, and strongly correlates with water content measured in the TPC exhaust gas. Therefore, we feel that v_0 is measured to 0.01 cm/μs, or 0.2%. The uncertainty of 10 ns on trigger delay time adds 0.2% systematic error on hit position. At the top of the 80 cm drift volume, this translates into precision of y-measurement of better than 2.4 mm.

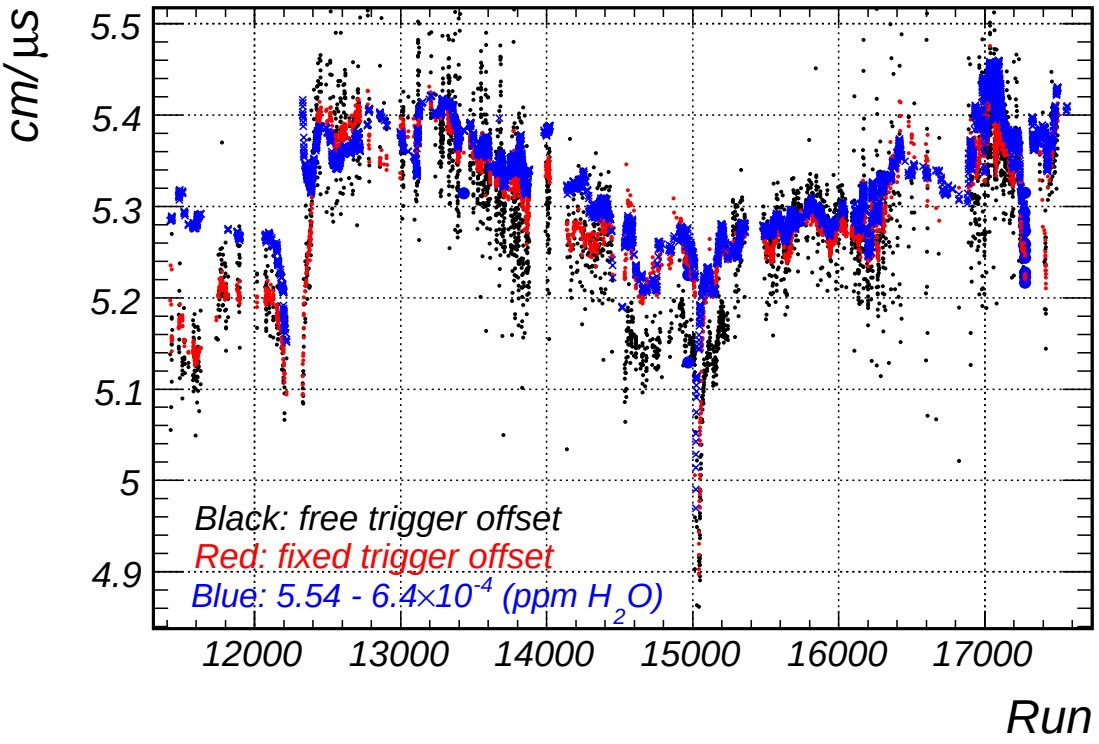

Figure 7.19: Measured TPC drift velocity as a function of run. The benefit of fixing trigger time is clear: the precision of velocity measurement is much higher, and the correlation with water content in the TPC gas becomes much stronger.

7.5.2 Distortion Corrections

Electron drift in a non-uniform magnetic field is a complicated problem. Conceptually, it is clear that if electric and magnetic fields are not collinear, the force due to magnetic field on electron creates a force proportional to $\vec{E}\times\vec{B}$, but electron motion in that direction will cause additional force proportional to $(\vec{E}\times\vec{B})\times\vec{B}$, hence all three components of the drift velocity are non-zero.

A linear model of drift is motivated by drag force which is proportional to drift velocity:

$$\frac{d\vec{v}}{dt} = \frac{e}{m}\vec{E} + \frac{e}{m}\vec{v}\times\vec{B} - \frac{\vec{v}}{\tau} = 0, \tag{7.2}$$

where $\vec{v}$ is the drift velocity, e is electron charge, m its mass, $\vec{E}$ is the electric field, $\vec{B}$ is the magnetic field and τ can be though of as the mean time between collisions of drifting electron and gas molecules. Equation 7.2 can be solved to obtain

$$\vec{v} = -\frac{|e|\tau E/m}{1+b^2}\begin{pmatrix}(1+b_x^2)e_x + (-b_z+b_xb_y)e_y + (b_y+b_xb_z)e_z\\ (b_z+b_xb_y)e_x + (1+b_y^2)e_y + (-b_x+b_yb_z)e_z\\ (-b_y+b_xb_z)e_x + (b_x+b_yb_z)e_y + (1+b_z^2)e_z\end{pmatrix}, \tag{7.3}$$

where signs take into account the negative charge of electron, $\vec{E} = E(e_x, e_y, e_z)$, $v_0 = |e|\tau E/m$, and $b_i = \dfrac{|e|\tau}{m}B_i = \dfrac{v_0}{E}B_i$.

If $\vec{E} = E\hat{y}$, and $\vec{B} = B(\cos\theta, \sin\theta, 0)$, this equation reduces to:

$$\vec{v} = -\frac{v_0}{1+b^2}\begin{pmatrix}b^2\cos\theta\sin\theta\\ 1+b^2\cos^2\theta\\ b\sin\theta\end{pmatrix}, \tag{7.4}$$

where $b = v_0B/E$.

However, when this equation is used to correct drift, one quickly sees that there is significant over-correction in both x and y (Figure 7.20). While we do not know the reason why linear model fails to describe the drift in the TPC, the solution was to use Magboltz Monte Carlo program[34, 35]. Magboltz takes the gas mixture, electric field, and constant magnetic field at arbitrary angle with respect to the electric field. Simulated trajectories of 10^6 electrons are used to predict the three drift velocity components. In order to use results given by Magboltz, we had to create a map of drift velocity components in (B, θ) space, with θ is defined by Equation 7.4. Figure 7.21 shows that we needed to model angles up to 50°.

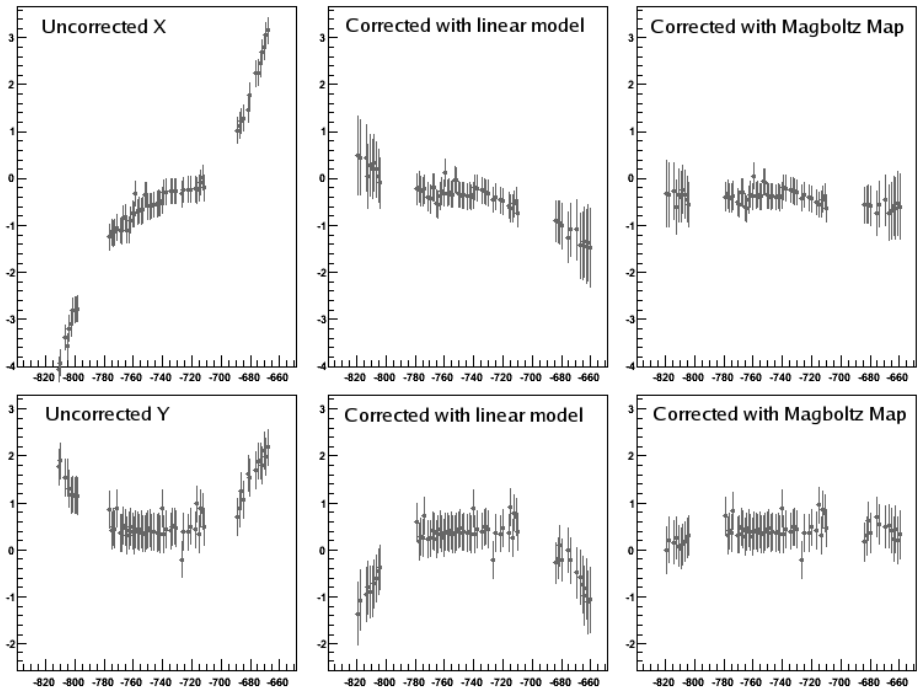

Figure 7.20: Shown are xz and yz projections of TPC hits from a 120 GeV/c track. The units on both axes are cm.

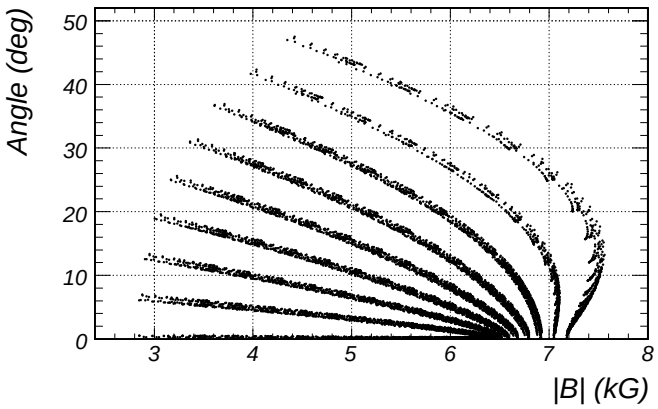

Figure 7.21: Angle between the vertical and horizontal field components in the JGG field map inside the TPC drift volume.

We included all details of the gas mixture that was provided by our monitoring:

- Oxygen concentration, which was relatively stable at 350 ppm.
- Nitrogen concentration at 78/21 of oxygen concentration, since oxygen must have come from air.
- Water concentration. Since drift velocity strongly correlates with water content, gas mixtures with 50, 300, 550, 700, and 950 ppm of water were modeled with v_0 of 5.403, 5.299, 5.179, 5.097, and 4.965 cm/μs respectively.

Equipped with 5 Magboltz maps and v_0 for a run, we compute the map for the run using a weighted sum of the 2 maps with closest v_0, since $v_i(B,\theta)/v_0$ depends on v_0. As Figure 7.20 shows this model of electron drift agrees with the data.

7.6 RICH R_0

Over the course of the run, CO_2 density in the RICH fluctuated by about 1.5%, which translates into a 3 mm difference in R_0 ($\beta = 1$ ring radius). The RMS width of 120 GeV/c proton ring distribution is about 1.8 mm, so at high momenta density fluctuations widen the ring radius distribution if ring radius is left uncorrected.

In the case of 120 GeV/c thin target data, calibration of the effective index of refraction is easily achieved by measuring radii of uninteracted protons. In a typical file with 5000 events one finds more than 1000 clean events with uninteracted protons. We can rewrite Equation 6.25 as

$$\frac{1}{2}R_0^2 = F^2 - \frac{F^2 - \frac{1}{2}R^2}{\sqrt{1 + m_{prot}^2/p_{beam}^2}}, \tag{7.5}$$

which allows us to compute R_0 from measured proton ring radius. Figure 7.22 shows the summary of RICH calibration thus obtained.

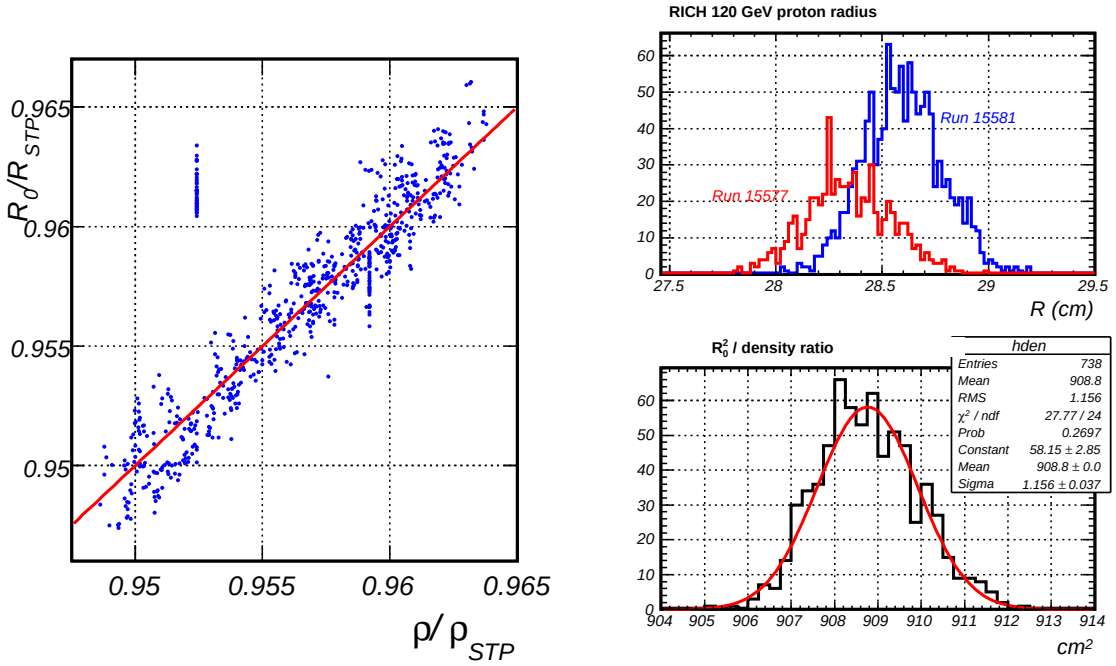

Figure 7.22: The left plot shows dependence of RICH R_0^2 on the density of CO_2, where both variables are divided by respective value at STP. The few outliers come from subruns where gas temperature or pressure are not recorded in the database. The $y = x$ line is superimposed to demonstrate that the expected linear dependence between R_0^2 and gas density is observed. The top right plot shows the difference in proton ring radius distributions in two extreme nearby runs. CO_2 pressure was raised between the two runs. Bottom right plot tells us that R_0^2 is known to about 0.1%.

Chapter 8

Monte Carlo Simulation

Monte Carlo simulation was necessary in order to measure reconstruction performance. In particular for this analysis, we need to know particle identification efficiency and backgrounds.

We used FLUKA-06 [22, 23] to simulate particle production and GEANT 3.21 [6] to transport particles through the spectrometer. GEANT hits (idealized energy deposition) were stored into the ROOT event tree, and hits were converted into digits (mock raw data) with packages written by the MIPP collaboration.

8.1 Time Projection Chamber Digitization

In order to get an accurate model of the TPC track, the following effects have to be modeled:

- Electron drifting in non-uniform magnetic field,
- Variations in gas gain due to different anode voltages,
- Diffusion of charge in space,
- Diffusion of charge in time,
- Electronic noise.

TPC gas volume inside the field cage has dimensions of $104.4 \times 79.4 \times 162.8$ cm. It was was segmented into $0.87 \times 1.05 \times 1.27$ cm rectangular parallelepipeds so that GEANT

could record hits at boundary crossings. The objective of digitization is to compute the ADC in each voxel. A voxel is defined as time slice on a pad in a padrow.

8.1.1 Generating Digits

Starting from hit position (x, y, z), we drift the hit to anode wire plane obtaining (x', y_{anode}, z') and drift time t_d (see Section 7.5.2). Fourth order Runge-Kutta stepper was implemented to do this, and with 0.5 μs steps it computed distortion with precision of about 1 micron, as tested by reversing the drift to restore input position.

Before TPC digits are generated, (x', z', t_{drift}) are converted to pad column, padrow, and time bucket $(x_{col}, x_{row}, t_{bkt})$ through

$$x_{col} = (x' - x_{col,0})/L_{col}$$
$$x_{row} = (z' - x_{row,0})/L_{row}$$
$$t_{bkt} = (t_d - t_{trig})/T_{bkt}$$

Here $x_{col,0}$ and $x_{row,0}$ are locations of column 0 and pad 0, $L_{col} = 0.8$ cm and $L_{row} = 1.2$ cm are pad sizes, and $T_{bkt} = 0.1\mu$s/bucket. Trigger time t_{trig} is generated as a constant time offset plus uniformly distributed $0 - 50$ ns jitter time. In real data, this time offset is measured, and the jitter results from the fact that the TPC 20 MHz clock is not synchronized to trigger time.

The next step is to spread the hit energy deposition over pads, columns and buckets. To improve performance of the algorithm, we defined a 3-dimensional array of total charge in TPC voxels. At the beginning of event, charge on each voxel is reset to 0. For each hit, we define a three dimensional energy density function as the product of Gaussian in pad column centered at x_{col}, Gaussian in padrow centered at x_{row}, and gamma function in buckets with the peak at t_{bkt}. The integral of the the function is set to hit energy deposition multiplied by gain factor which is different for every anode section of the TPC. For each TPC voxel where the integral of the density function is at least 0.5 counts, the charge sum is incremented, and the track number that generated the hit is added to the track list associated with the voxel. Having the associated track list allows to establish correspondence between reconstructed track and MC track.

In the course of the run, some anode regions were not able to hold the nominal high voltage of 1250 V, thus creating large dead regions in the TPC. Undoubtedly, the missing

data has an adverse effect on track finding algorithm, so it has to be modeled. Each anode region was assigned a different gain: the factor converting GEANT hit energy deposition to ADC. Additional missing data comes from electronic problems as a number of sticks (two half-padrows) never readout. These sticks were turned off in the Monte Carlo simulation.

To generate TPC digits, for each voxel on a good stick with at least 1 ADC count, we multiply the charge by an Gaussian random number centered at 1 to randomize pad gain. Finally, we add a Gaussian pedestal and if the total charge in the voxel is above threshold, it is written out.

8.1.2 Generating Noise

There are 3 sources of noise in the TPC:

1. Hot voxels;
2. Hot pads where all voxels are lit up or every other voxel is on;
3. Charged cosmic particles.

All of these sources of noise are typically well rejected by the TPC reconstruction alogrithm. Cosmic particles are rare, and are not likely to go through the target, so they were not modeled. In order to speed up modeling of noise, a random Gaussian number of voxels was selected to be noisy in an event and their ADC spectrum was was generated to be consistent with data.

8.2 Wire Chamber Digitization

GEANT hits in wire chamber planes were converted to hit wires by computing the number of drift cells that the track crossed, and dividing deposited energy equally between all wires. A track number list is filled for every wire as the deposited energy is being added to wires. Charge from all hits is integrated over all wires, and wires above threshold are written out as digits. This approach makes it more difficult to tune chamber efficiency than choosing a random number for each wire. However, it is motivated by the physics of wire chambers, and makes it possible to simulate cross talk where it is most likely to happen given distribution of particles at the chamber.

In addition to computing wires above threshold, drift time needs to be calculated in the drift chambers. As the charge is being split between wires, the minimum distance from track to wire is stored. In the case where more than 2 drift cells are crossed, minimum distance is set to 0 for the inner wires. Minimum distance is converted into drift time using linear relation between drift distance and drift time.

Final part of chamber digitization is to add cross talk. Cross talk on discriminator/pre-amplifier cards was simulated by computing the total amount of charge on each card, and a fraction of that charge added to all wires on the card. In the case of drift chambers, the common group is 8 wires, and 32 in proportional chamber. If a wire that gets cross talk contribution was not hit, its minimum drift distance is set to the smallest drift distance in the group in order to preserve causality.

8.3 RICH Hits and Digitis

Cherenkov photons in the RICH are generated by GEANT with a fixed gas density consistent with the average CO_2 density during the data taking. Over the year of running, the density in the RICH varied by about 1%. Given the fact that detector can be easily calibrated (see Section 7.6) one gas density for Monte Carlo is sufficient.

To generate PMT hits, photons are generated along the trajectory of the track according to the parametrized functional form of the index of refraction (see Figure 6.11). Photons are then transported to be reflected off the mirrors and then to the PMT array. Absorption in CO_2, reflectivity of the mirrors, opacity of the quartz windows are taken into account in transport of photons.

Digits are generated by choosing a random number between 0 and 1 for each photon. Photons with this number above PMT efficiency for the photon's wavelength generate digits.

Chapter 9

Data Analysis

Objective of the data analysis is to extract the ratios of production of charged pions and kaons with momentum above 20 GeV/c using 120GeV/c proton data on 2% interaction lengths carbon target in bins of longtitudinal and transverse particle momentum. With four particle species ($K^{\pm}, \pi^{\pm}$), there are a total of six ratios, although only three are mathematically independent. In practice, the four ratios of interest are those of like charges and like species, i.e. K^+/π^+, K^-/π^-, K^-/K^+, and π^-/π^+, since systematic errors of the four ratios are different and the latter two ratios have been described phenomenologically[4] with simple relation.

9.1 Data Binning

9.1.1 Geometric acceptance

Although the objective is to sample as much of (p_z, p_T) space as possible, geometric acceptance of the RICH is not perfect above 20 GeV/c . Figure 9.1 shows acceptance of the PMT array for particles with ring centers within 5 cm of the edge of the array. At 20 GeV/c momentum kaon ring radius is approximately 15 cm, so a significant fraction of the ring must be detectable to provide positive identification.

Given the statistics of recorded proton carbon interactions and fact that transverse momentum spectrum is steeply falling (see Figure 9.2), we limit our attention to regions of the space where geometric acceptance of the RICH is at least 50%.

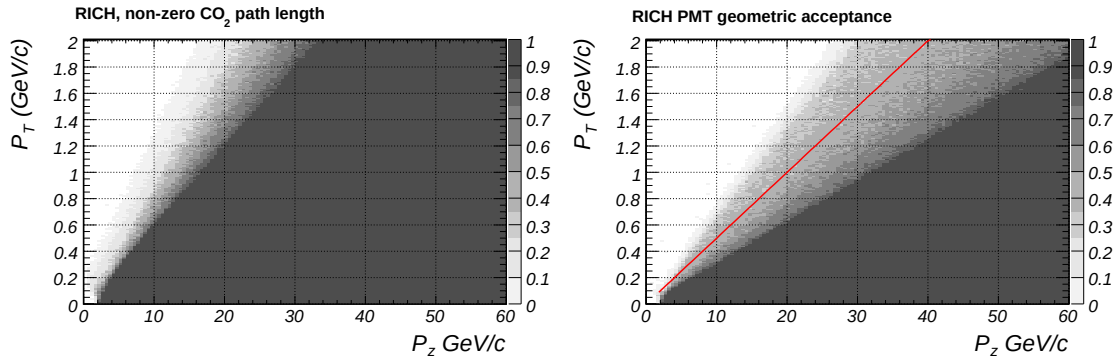

Figure 9.1: Shown are geometric acceptances for RICH radiator volume and PMT array where the ring center is within 5 cm of PMT array. Line $p_T = 0.05p_z$ shows the limit for 50% geometric acceptance by the photomultipliers.

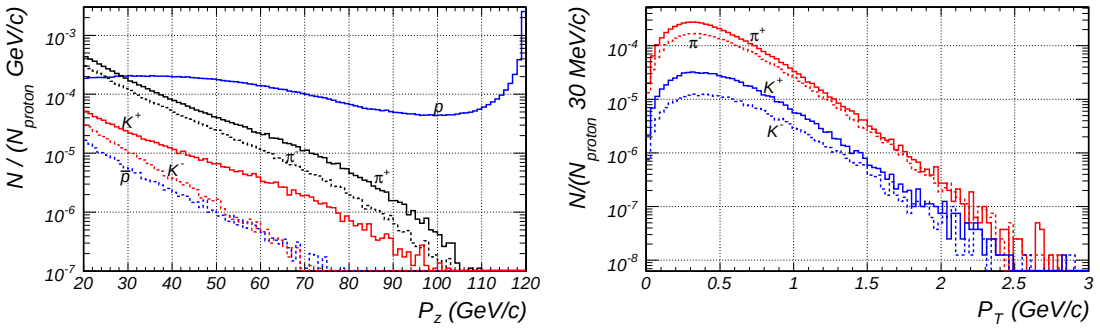

Figure 9.2: Shown are charged hadron fluxes with longtitudinal momentum above 20 GeV/c per incident proton as simulated by FLUKA-06 on 2% carbon target.

9.1.2 Bin Selection

The choice of upper and lower limits on p_z is governed by two considerations. Kaon threshold is around 17 GeV/c , thus 20 GeV/c momentum with $\sim 5\%$ momentum resolution ensures minimal bias from the threshold effect which we are unable to measure from the data at this time. Particle production with momentum above 90 GeV/c is heavily dominated by inelastically scattered protons, so cutting the right bin at $p_z < 90$ GeV/c will reduce the background underneath K^+ peak and remove a small number of true kaons and pions.

In the limit of infinite statistics, one would like to have the smallest bins possible. However with $5 \cdot 10^5$ recorded triggers and estimated 50% interaction trigger purity, we must select sufficiently large bins in order to have a statistically significant measurement. Figure 9.3 shows bin by bin the expected number of π^+ from $2 \cdot 10^5$ proton-carbon interactions modeled in FLUKA-06. Of the four particles of interest, π^+ is the majority particle, hence at the very least one needs to have a significant number of pions to do the measurement. The criteria used to select bin boundaries was to get 3% or better statistical error on π^+ if possible. On the other hand, momentum resolution is at most 5.5%, so using that as the upper limit, we select at least 20% bins so that mixing between bins is minimized. The 24 bins defined for the measurement are

Bin	Minimum p_z	Minimum p_z	Maximum p_T	Maximum p_T
(0, 0)	20	24	0	0.2
(0, 1)	20	24	0.2	0.4
(0, 2)	20	24	0.4	0.6
(0, 3)	20	24	0.6	1.0
(1, 0)	24	31	0	0.2
(1, 1)	24	31	0.2	0.4
(1, 2)	24	31	0.4	0.6
(1, 3)	24	31	0.6	1.0
(1, 4)	24	31	1.0	1.2
(2, 0)	31	42	0	0.2
(2, 1)	31	42	0.2	0.4
(2, 2)	31	42	0.4	0.6
(2, 3)	31	42	0.6	1.0
(2, 4)	31	42	1.0	1.55
(3, 0)	42	60	0	0.2
(3, 1)	42	60	0.2	0.4
(3, 2)	42	60	0.4	0.6
(3, 3)	42	60	0.6	1.0
(3, 4)	42	60	1.0	2.0
(4, 0)	60	90	0	0.2
(4, 1)	60	90	0.2	0.4
(4, 2)	60	90	0.4	0.6
(4, 3)	60	90	0.6	1.0
(4, 4)	60	90	1.0	2.0

9.2 Pileup Removal

Resonant extraction from the Main Injector could not be tuned to guarantee a single particle per 10 μs cycle in the machine, therefore a significant fraction of triggers contain two or more incident protons. While the probability of both protons to interact is small, pileup can create confusion in vertex finding and fitting. Since this bias is not modeled in the Monte Carlo, it is best to remove pileup events from the analysis.

In order not to bias the measurement, pileup removal has to be done using information from detectors upstream of the target as much as possible. This includes

- Number of tracks in the beam chambers, and beam track time;
- Three scintillator counters (charge and hit time differences);
- Four beam Cherenkov PMT signals (charge and hit times);

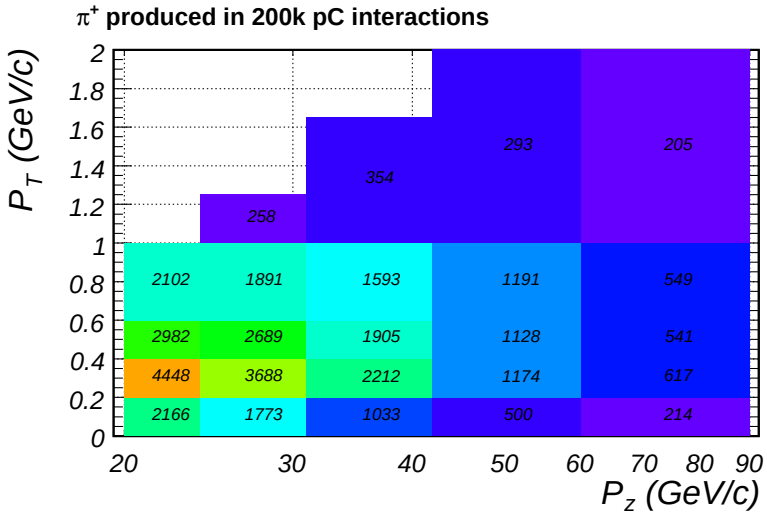

Figure 9.3: Expected number of π^+ events in the bins selected for the ratio measurement. Bin boundaries in p_z are 20, 24, 31, 42, 60, 90 GeV/c , and in p_T 0.2, 0.4, 0.6, 1 GeV/c . The largest p_T bin stretches to 2 GeV/c or 0.05 of the lower bin boundary, which corresponds to 50% geometric acceptance.

- Times of reconstructed secondary tracks.

We can easily select pileup events by looking at the amount of energy deposited by uninteracted proton tracks inside the TPC. Figure 9.4 shows that when two or more tracks are on top of one another, TPC integrates the total ionization energy resulting in multiple peaks in dE/dx. One has to keep in mind that the chamber integrates over 15 μs, while most detectors keep information in a 100 ns window, and chamber TDCs have 1 μs window. Therefore a fraction of events which look like pileup in the TPC will create normal response in all other detectors.

Events with $dE/dx < 3$ were taken to come from clean events, whereas those with $dE/dx > 5$ were selected as pileup candidates. Figure 9.5 shows distribution of variables which are most helpful to select between clean and pileup events. In order of significance, these are

1. Number of beam tracks is greater than 1;
2. Average charge of beamline scintillator counters is greater than 1.8;
3. Beam track time is outside of -5 to 20 ns window;

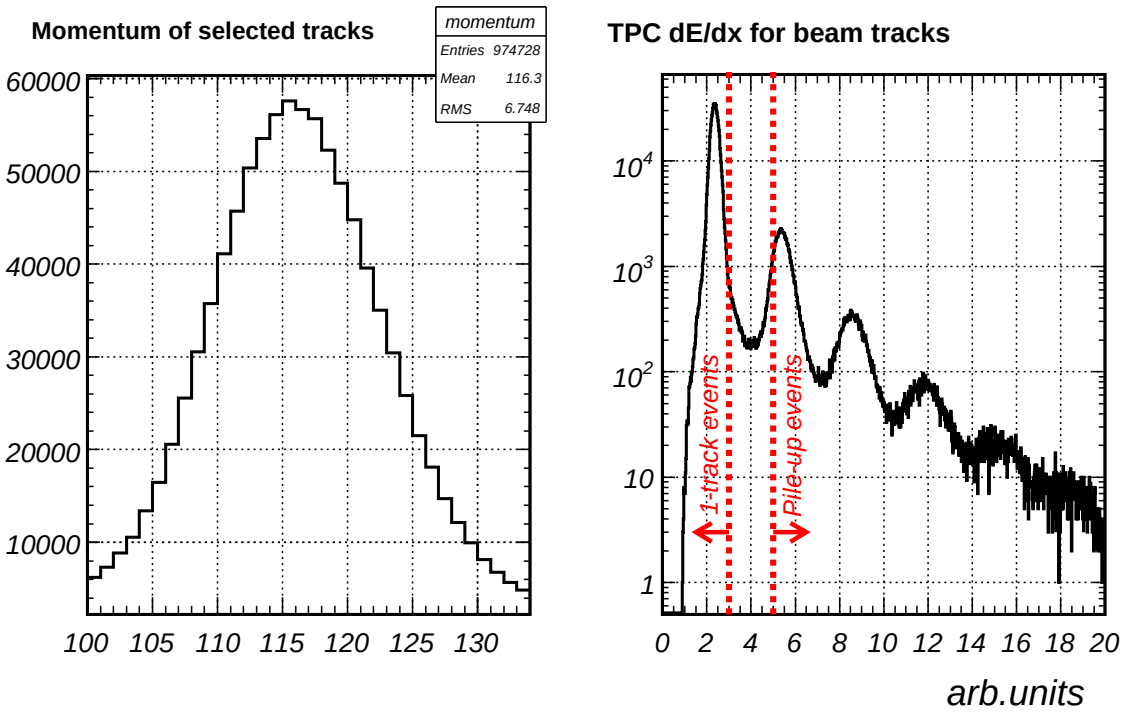

Figure 9.4: Shown is momentum (in GeV/c) and energy loss of beam tracks in the TPC where single and pileup proton tracks are easily identified.

4. Large (greater than 1 ns) time difference of signals in T0 counters;

5. Average charge of beam Cherenkov charge is greater than 330 ADC counts;

6. Inconsistent TDC values of beam Cherenkov counters.

One additional cut is placed on the time of secondary tracks. This is the only cut that does involve data from detectors downstream of the target. However, as Figure 9.6 shows, in case of single-proton tracks selected for pileup study, only 1% of events with no pileup candidates have out of time secondary tracks and 45% of pileup candidates have out of time secondary tracks. Thus, requiring that all tracks come in between -15 and 55 ns removes additional sources of pileup.

In addition to dE/dx in the TPC, additional variable that helps us judge the performance of pileup removal is the amount of energy deposited in the hadronic calorimeter. Figure 9.7 shows that the cuts clean up energy deposition in the TPC volume and in the hadronic calorimeter. While about 20-40% of the data contains pileup after these simple cuts less than 1% of the data contains events with pileup.

9.3 Primary Vertex Selection

With 6 mm vertex resolution in z, the cuts on target-like events needs to be done in such a way so as not to introduce a bias into the measurement. We open a wide window to include both the target and the scintillator, and subtract appropriately scaled target out data.

To determine the fraction of target out data that needs to be subtracted from target in data, we plot distributions of vertex z in each set in pileup free events. The shape of the z distribution is well described by a Gaussian with exponential tails on both sides plus a constant background. First, we make a fit to the target out data to determine the shape of the trigger counter peak. To fit for the target in distribution, we hold all parameters of the scintillator peak fixed except for the amplitude. Figure 9.8 shows that this technique does a good job at fitting for the carbon data z distribution and tells us that the available target out data needs to be scaled by 0.934 ± 0.026 to account for the presence of scintillator behind the target. Based on this plot we can tell that by defining target region from -832 to -825 cm in z will eliminate any potential bias due to cuts.

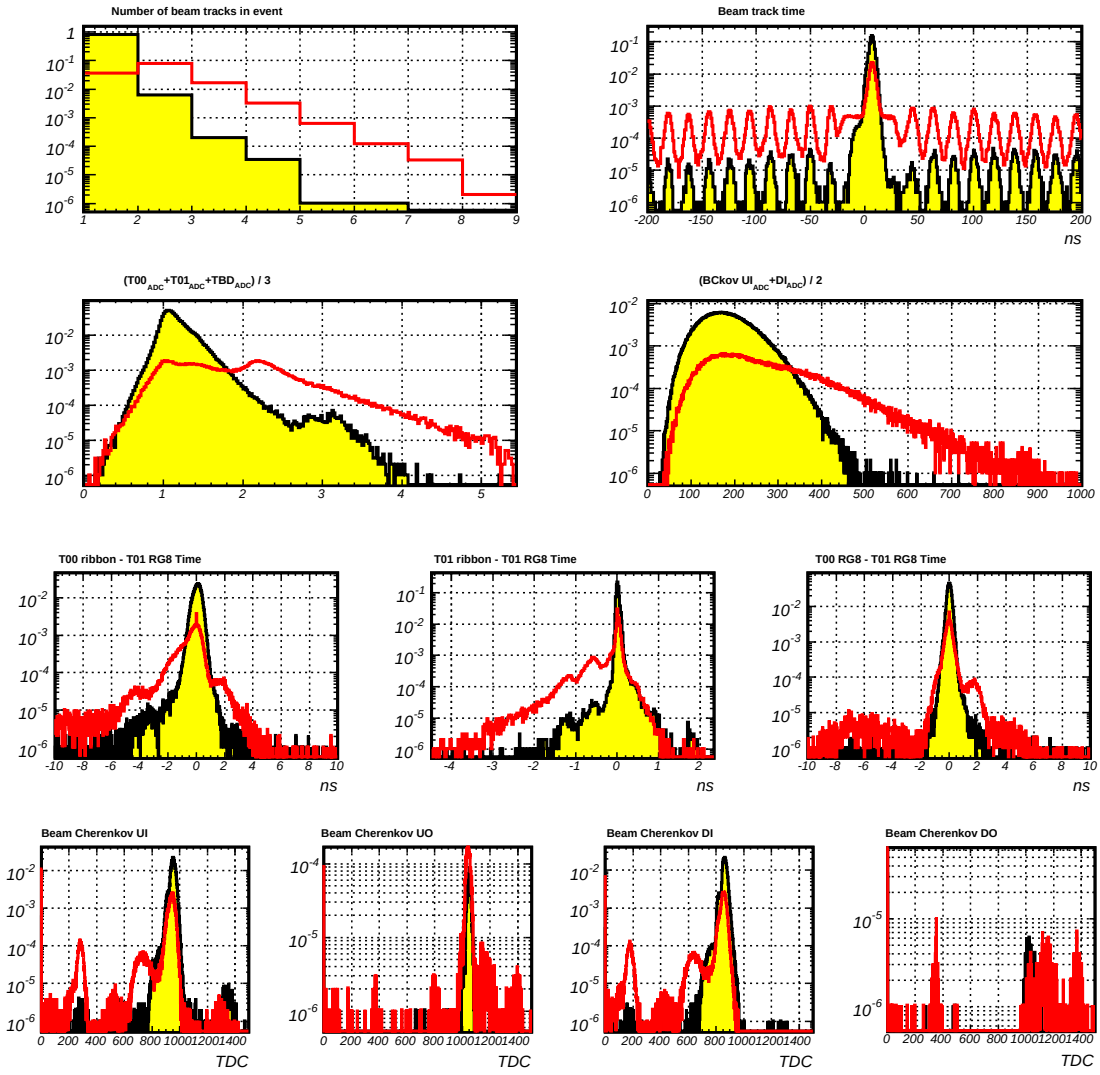

Figure 9.5: Distribution of variables that help distinguish pileup events from clean events. Solid yellow histograms are filled with information from single-track candidates, and red histograms from pileup candidate events.The histograms are scaled by the total number ($5.7 \cdot 10^5$) of proton tracks selected for the pileup study.

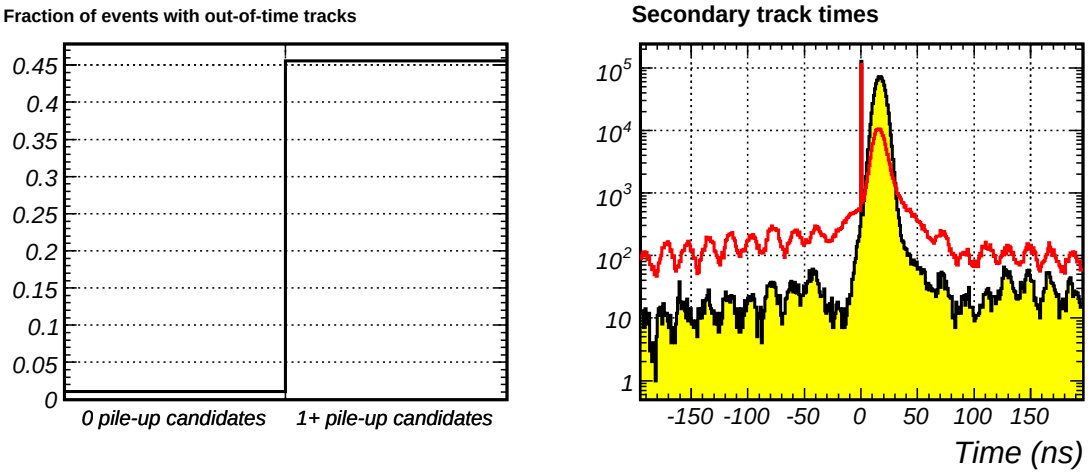

Figure 9.6: Shown on the left is fraction of events containing out of time secondary tracks in single proton candidate and pileup candidate events. On the right is distribution of times for the two classes of events. The peak at 0 ns corresponds to tracks that have no information from the drift chambers.

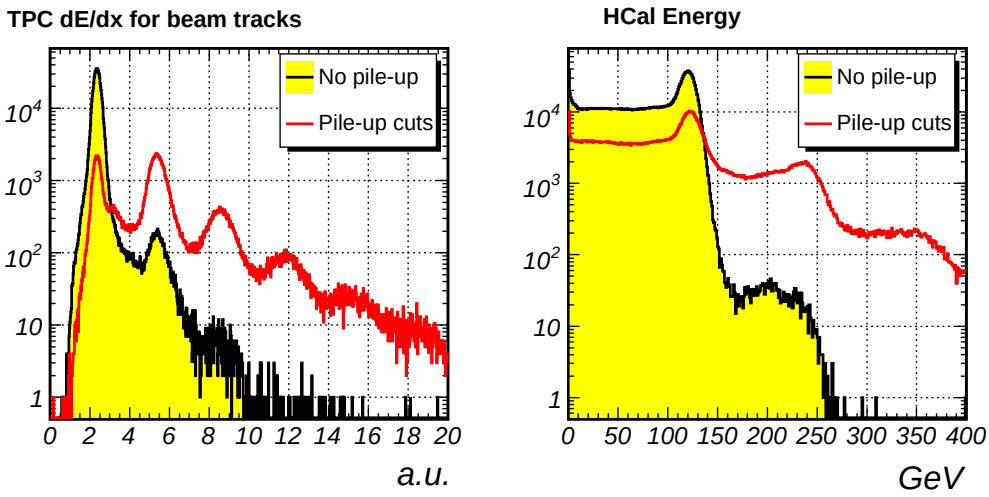

Figure 9.7: pileup cuts are good at removing multiple peaks from TPC dE/dx of beam tracks and very high calorimeter energy. Less that 1.5% of beam tracks have measured dE/dx consistent with two or more particles and less than 0.5% of events deposit more energy than a single 120 GeV/c proton.

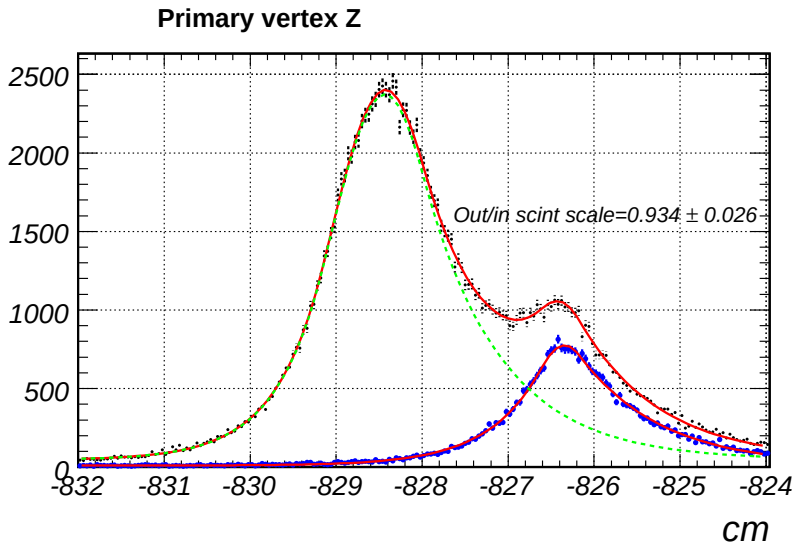

Figure 9.8: 2% carbon and target out data. The scale factor of available thin target data is based on fitting Gaussian with exponential tails to the target and the interaction counter.

9.4 Interaction Trigger Efficiency

Interaction trigger efficiency needs to be understood as multiplicities of events containing kaons and pions may be somewhat different. To remove bias from calculation of the efficiency, we selected interactions from events where minimum bias trigger recorded the event. For the study of interaction trigger efficiency, we selected events with no pileup and vertex z between -831 and -827 cm.

9.5 Particle ID Variable

Computed mass squared using RICH ring radius varies with particle p_z and p_T making it impossible to directly compare data and Monte Carlo simulation (see Figures 9.11 and 9.12). To alleviate this problem, we create a particle ID variable α through

$$\alpha(m^2) = a_{ij} + b_{ij}m^2, \tag{9.1}$$

where a_{ij} and b_{ij} are different from bin to bin. We defined $\alpha = 0$ to correspond to pion and $\alpha = 1$ to proton. Then kaon peak will be found at 0.265.

To find a_{ij} and b_{ij}, in each (p_z, p_t) bin we group negatives and positives from carbon, beryllium, and target out data together. Distributions of m^2 are fit for pion and

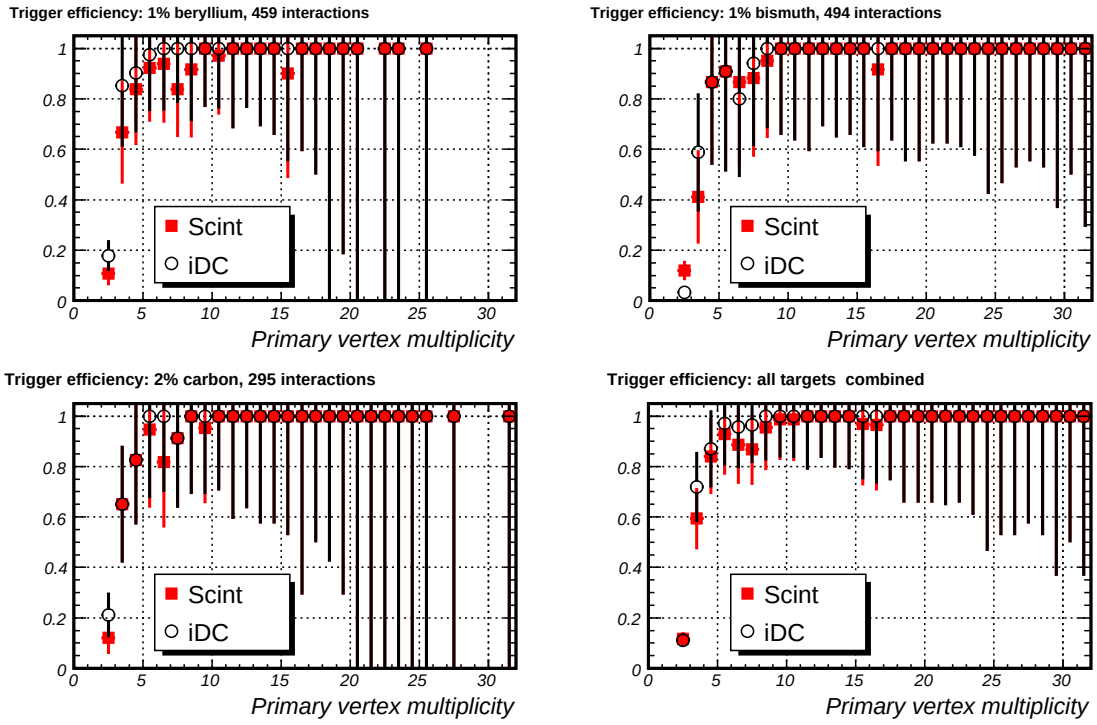

Figure 9.9: Interaction trigger efficiency for different targets at 120 GeV/c and the combined trigger efficiency for all targets.

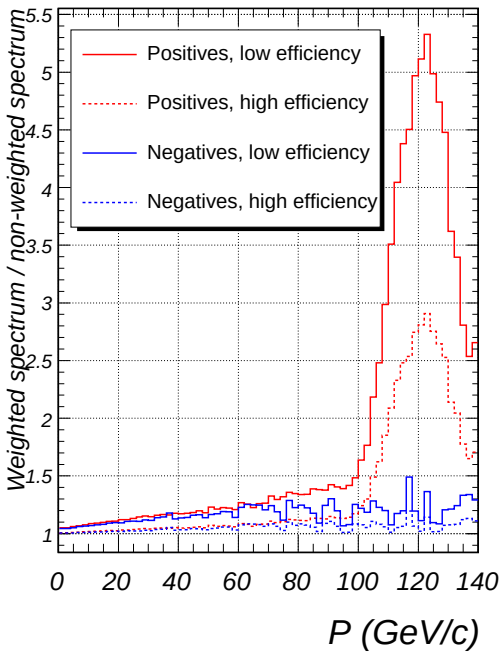

Figure 9.10: Combined carbon, beryllium, and target out momentum spectrum enhancement under the assumptions of the most efficient and the most inefficient trigger.

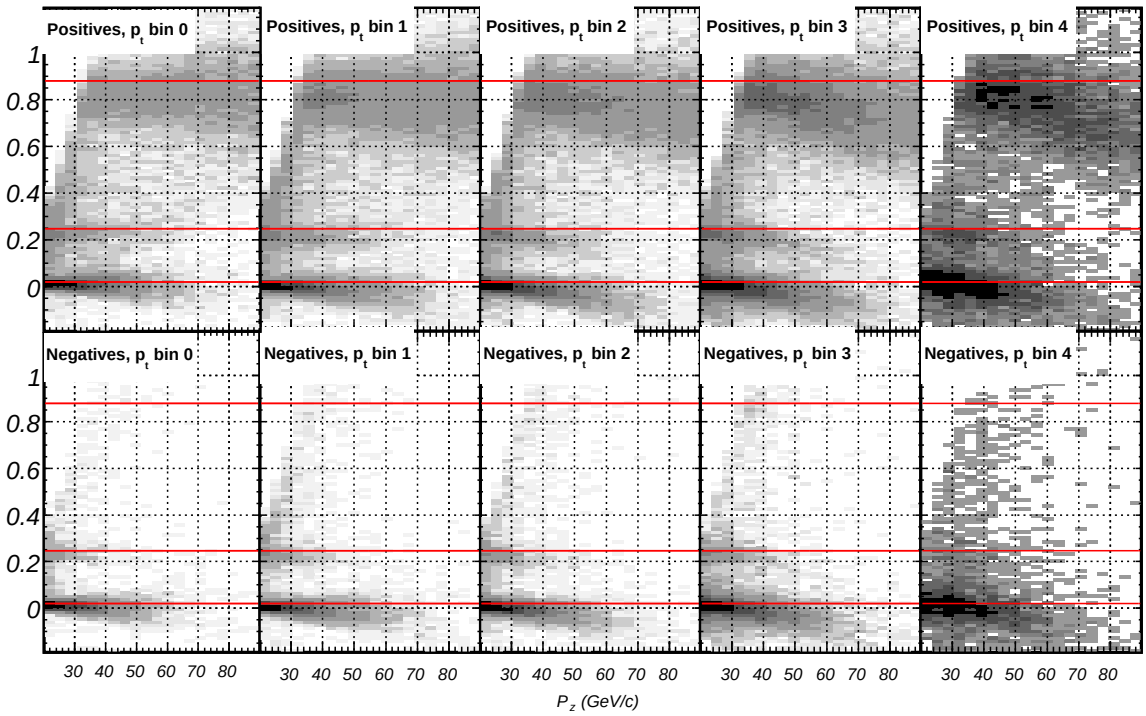

Figure 9.11: Variations of computed mass squared with p_z and p_t make it impossible to directly compare data and Monte Carlo. Superimposed are horizontal lines corresponding to mass squared of pions, kaons, and protons.

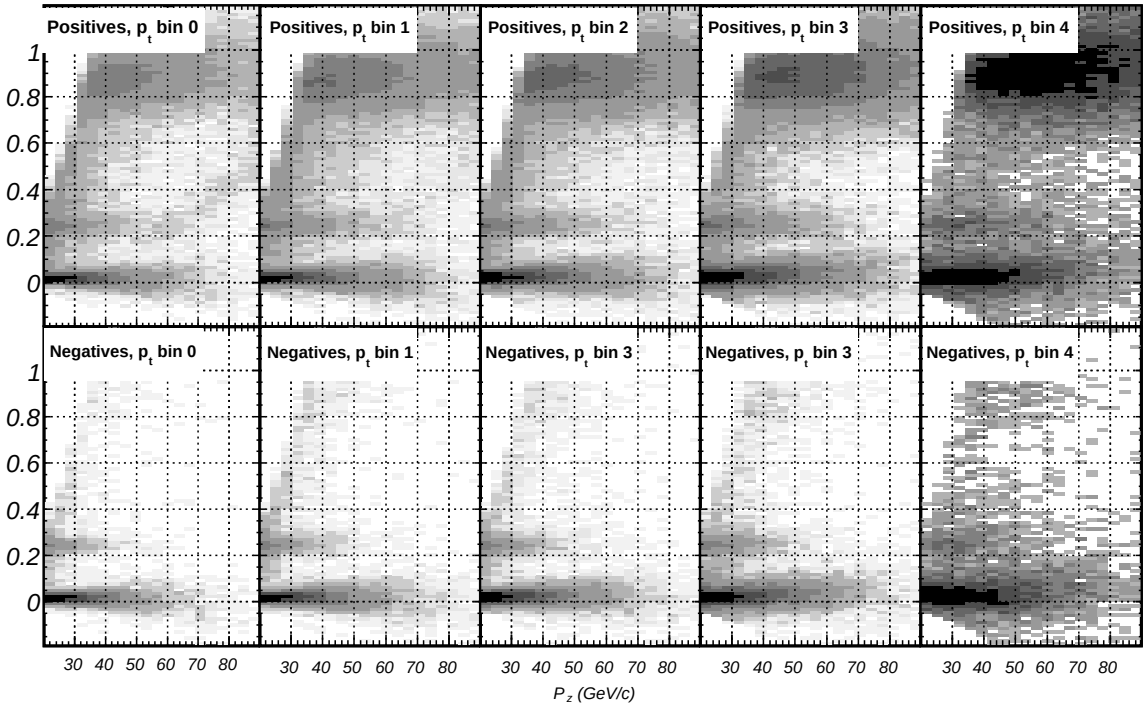

Figure 9.12: Variations of computed mass squared observed in data are not present in Monte Carlo.

		Data				Monte Carlo	
p_z bin	p_t bin	$m_\pi^2 \cdot 10^3$	$m_p^2 \cdot 10^3$	$a_{ij} \cdot 10^3$	b_{ij}	$a_{ij} \cdot 10^3$	b_{ij}
0	0	12.9 ± 0.1	228.4 ± 1.2	-15.9	1.230	-23.8	1.171
0	1	8.4 ± 0.1	229.3 ± 0.9	-10.1	1.199	-25.3	1.175
0	2	8.5 ± 0.1	229.8 ± 1.1	-10.1	1.197	-25.7	1.170
0	3	12.2 ± 0.2	228.2 ± 1.2	-14.9	1.226	-26.1	1.172
1	0	11.0 ± 0.2	228.4 ± 1.2	-13.4	1.219	-23.1	1.161
1	1	4.0 ± 0.1	222.8 ± 0.9	-4.8	1.211	-26.2	1.175
1	2	2.3 ± 0.1	223.3 ± 0.7	-2.8	1.199	-27.5	1.172
1	3	4.2 ± 0.2	225.5 ± 1.1	-5.1	1.198	-27.2	1.169
1	4	13.3 ± 1.4	219.2 ± 3.4	-17.2	1.287	-29.0	1.168
2	0	8.2 ± 0.3	794.5 ± 2.2	-10.5	1.272	-22.3	1.208
2	1	-3.6 ± 0.2	792.4 ± 1.3	4.6	1.256	-27.1	1.211
2	2	-8.9 ± 0.2	799.4 ± 1.2	11.1	1.237	-32.4	1.202
2	3	-9.2 ± 0.3	804.7 ± 1.3	11.3	1.229	-32.4	1.196
2	4	-1.9 ± 1.3	803.3 ± 3.9	2.4	1.242	-32.7	1.188
3	0	2.0 ± 0.8	810.0 ± 1.7	-2.5	1.238	-15.8	1.147
3	1	-15.3 ± 0.6	807.6 ± 1.0	18.5	1.215	-22.0	1.150
3	2	-27.2 ± 0.6	797.4 ± 1.0	32.9	1.213	-31.9	1.160
3	3	-33.1 ± 0.6	791.0 ± 1.0	40.2	1.214	-40.1	1.164
3	4	-27.6 ± 1.9	810.1 ± 2.8	33.0	1.194	-38.9	1.151
4	0	-11.9 ± 2.8	813.6 ± 1.7	14.4	1.211	-8.6	1.111
4	1	-34.7 ± 2.0	793.6 ± 1.2	41.9	1.207	-11.5	1.116
4	2	-58.2 ± 2.2	766.3 ± 1.3	70.6	1.213	-24.8	1.132
4	3	-67.5 ± 2.2	744.2 ± 1.4	83.2	1.232	-48.7	1.150
4	4	-80.9 ± 5.7	726.7 ± 3.5	100.1	1.238	-61.2	1.150

Table 9.1: Coefficients for conversion from m^2 in $(\mathrm{GeV}/c^2)^2$ into particle ID variable α. For p_z bins 0 and 1, the numbers were computed using pion and kaon peak since proton is under threshold below 31 GeV/c . Ideal $a_{ij} = -22.45 \cdot 10^{-3}$ and $b_{ij} = 1.162$ $(\mathrm{GeV}/c^2)^2$.

proton peak or kaon if proton is under threshold in both data and Monte Carlo. Peak positions are then converted into coefficients through

$$b = \left[m_p^2 - m_\pi^2\right]^{-1} \tag{9.2}$$

$$a = -bm_\pi^2 \tag{9.3}$$

9.6 Corrections from Monte Carlo Simulation

9.6.1 Need for Corrections

A number of effects which one cannot easily extract from data must be corrected for. These include

1. Interactions in the spectrometer: about 10% of secondary particles will interact before reaching the RICH;
2. Interactions in the RICH flange: about 10% of particles passing through the flange rather than the RICH window will interact;
3. Decay in flight: about 10% of kaons will decay before they reach the RICH;
4. Particle misidentification due to RICH efficiency and ring fitting efficiency;
5. Particle misidentification due to multiple scattering: large angle scattering of a small fraction of protons (majority particle above $\sim$ 30 GeV/c) will create a measurable contamination, especially under the kaon peak;
6. Decay products of neutral particles (e.g. K_S, Λ) that get incorrectly pulled into the primary vertex.
7. Interactions in the trigger counter;

Figures 9.13 and 9.14 show that data and Monte Carlo distributions of the particle ID variable compare well in most bins, although Monte Carlo peaks are somewhat narrower.

9.6.2 Background Modeling

In order to extract correct numbers of pions and kaons, one has to evaluate the shape of the background in the particle ID variable and subtract the background from underneath the peaks. Figure 9.15 shows distribution of reconstructed Monte Carlo mass squared in one of the bins. As one would expect, protons are the primary source of background under the kaon peak in the bin where proton is under threshold. What is more surprising that a significant number of true protons get identified as pions. The possible explanations for this are

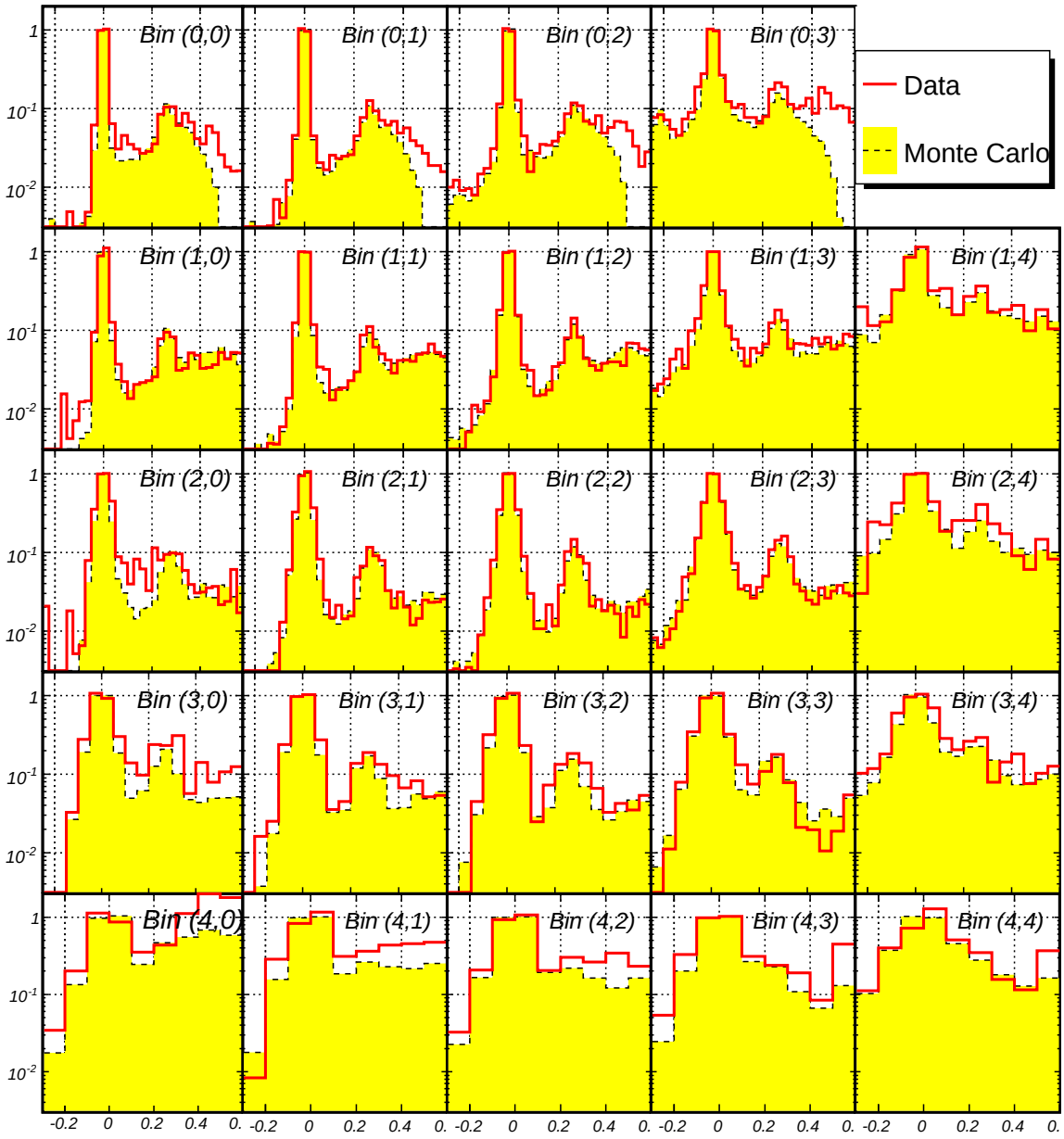

Figure 9.13: Data – Monte Carlo comparison of particle ID variable distributions for positives in the (p_z, p_t) bins. Histograms are normalized to set the pion peak to 1.

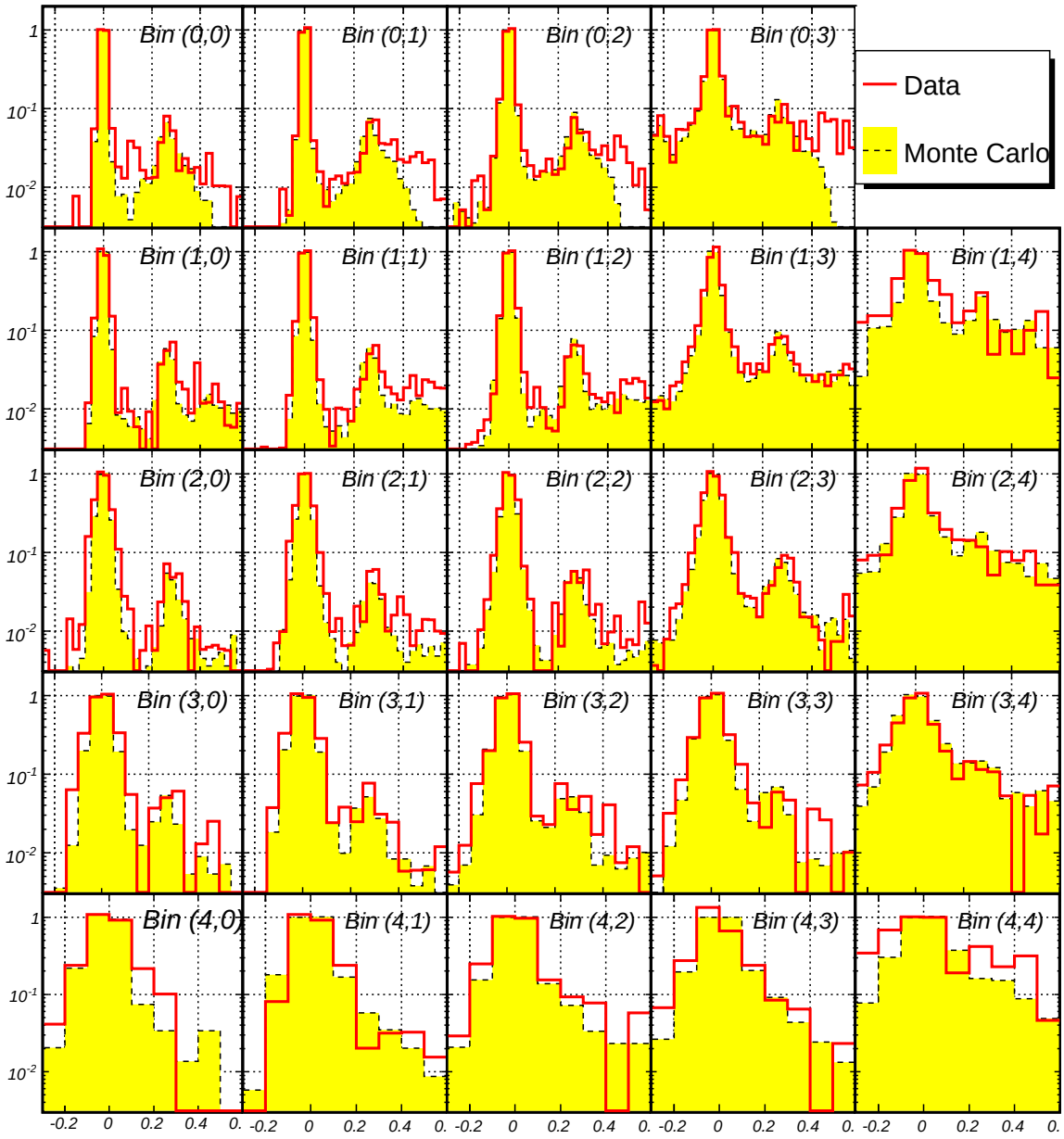

Figure 9.14: Data – Monte Carlo comparison of particle ID variable distributions for negatives in the (p_z, p_t) bins. Histograms are normalized to set the pion peak to 1.

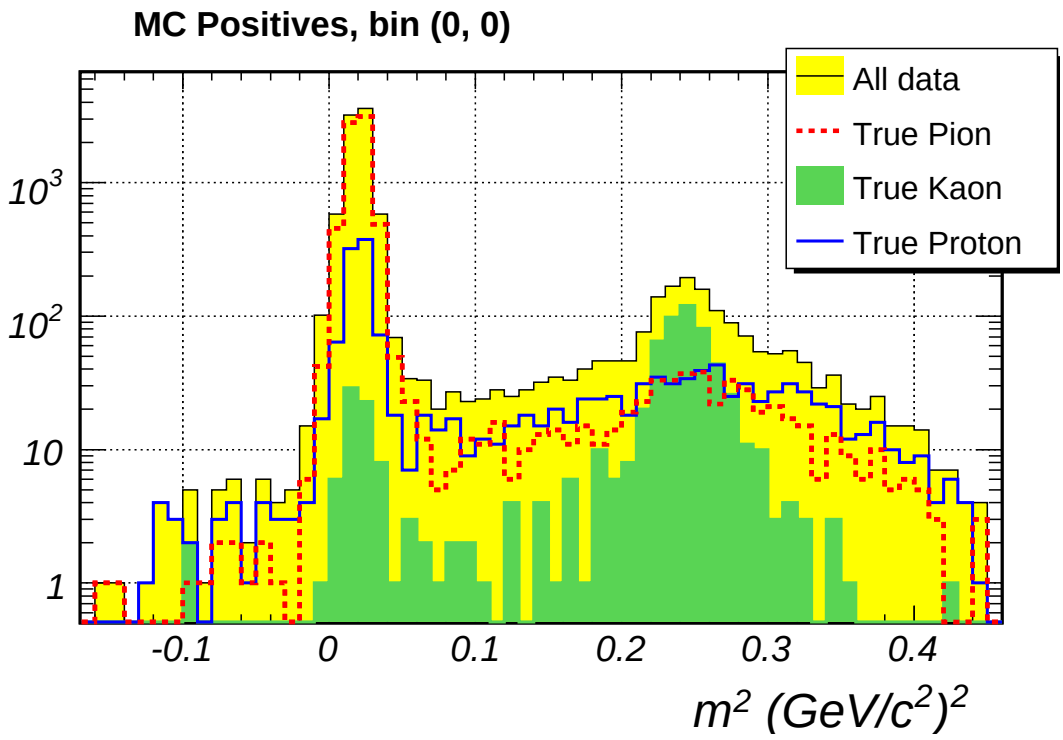

Figure 9.15: Shown is reconstructed Monte Carlo mass squared in the first bin. It is clear that background has to be subtracted in order to extract correct number of kaons.

- Protons interacting in the spectrometer that create a forward pion or electron so that the track is extended into the RICH and get identified as pions;
- Incorrect reconstructed – true track association.

Currently, data – Monte Carlo comparison is the best model of background that we have, so to extract the signal from the background, we use true Monte Carlo information to extract the occupancy o of pions and kaons in the bins of particle ID histograms. Pion (kaon) occupancy is defined as the fraction of true pions (kaons) with reconstructed momentum within 4 σ of true momentum. The highest occupancy (see Figures 9.16 and 9.17) almost never goes above 0.8. From interactions in the spectrometer and large angle multiple scattering, one would expect this value to be closer to 0.9, so we will study the effect on the measurement by changing $(1 - o)$ by 10% from the computed value.

Equipped with occupancy in each bin, we apply it to a data sample multiplying every bin of the data binned the same way by the computed occupancy. Then the number of pions in kaons is simply the integral of the derived histograms. The error on the count

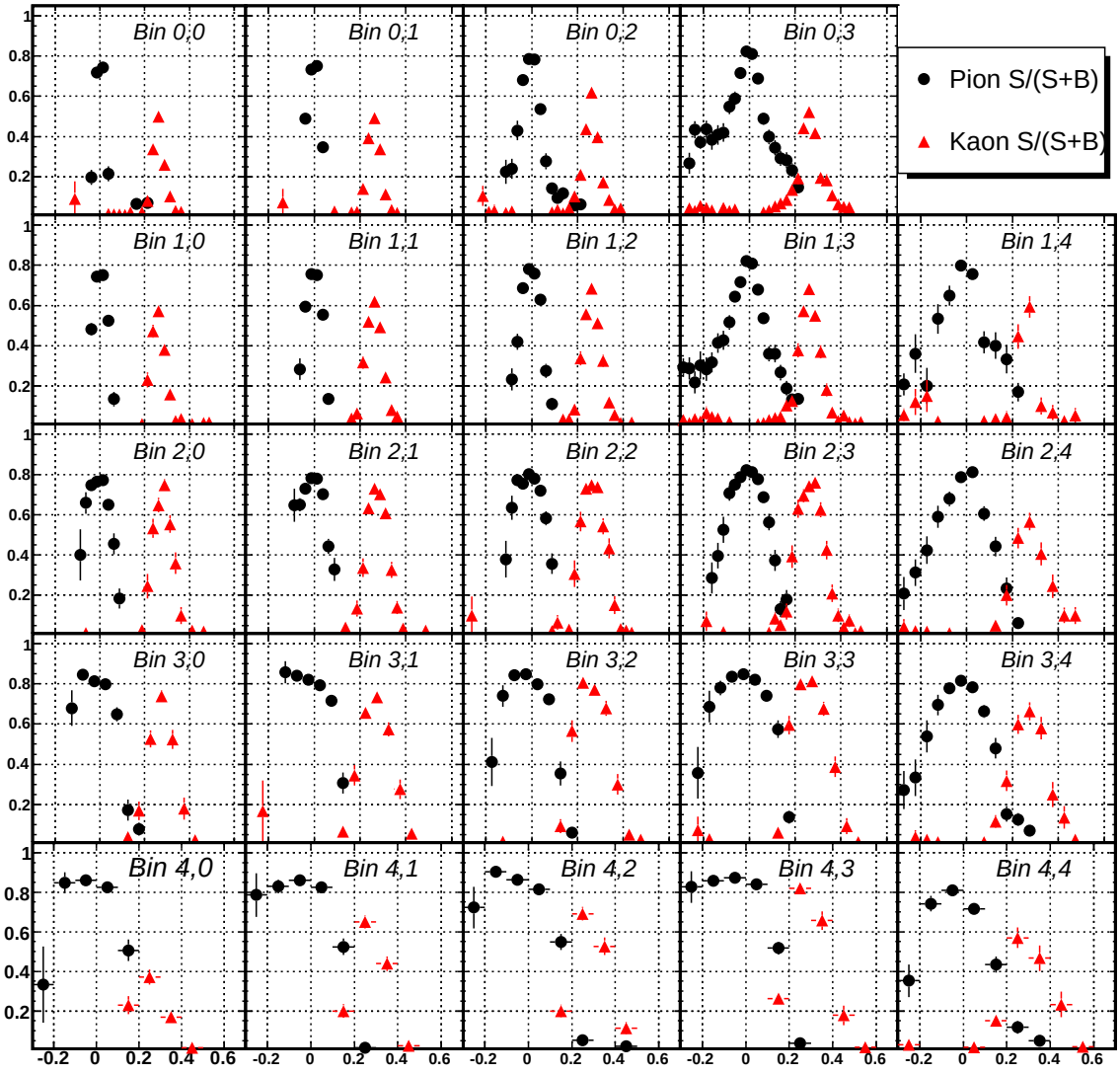

Figure 9.16: Occupancy of positive pions and kaons in Monte Carlo in the (p_z, p_t) bins.

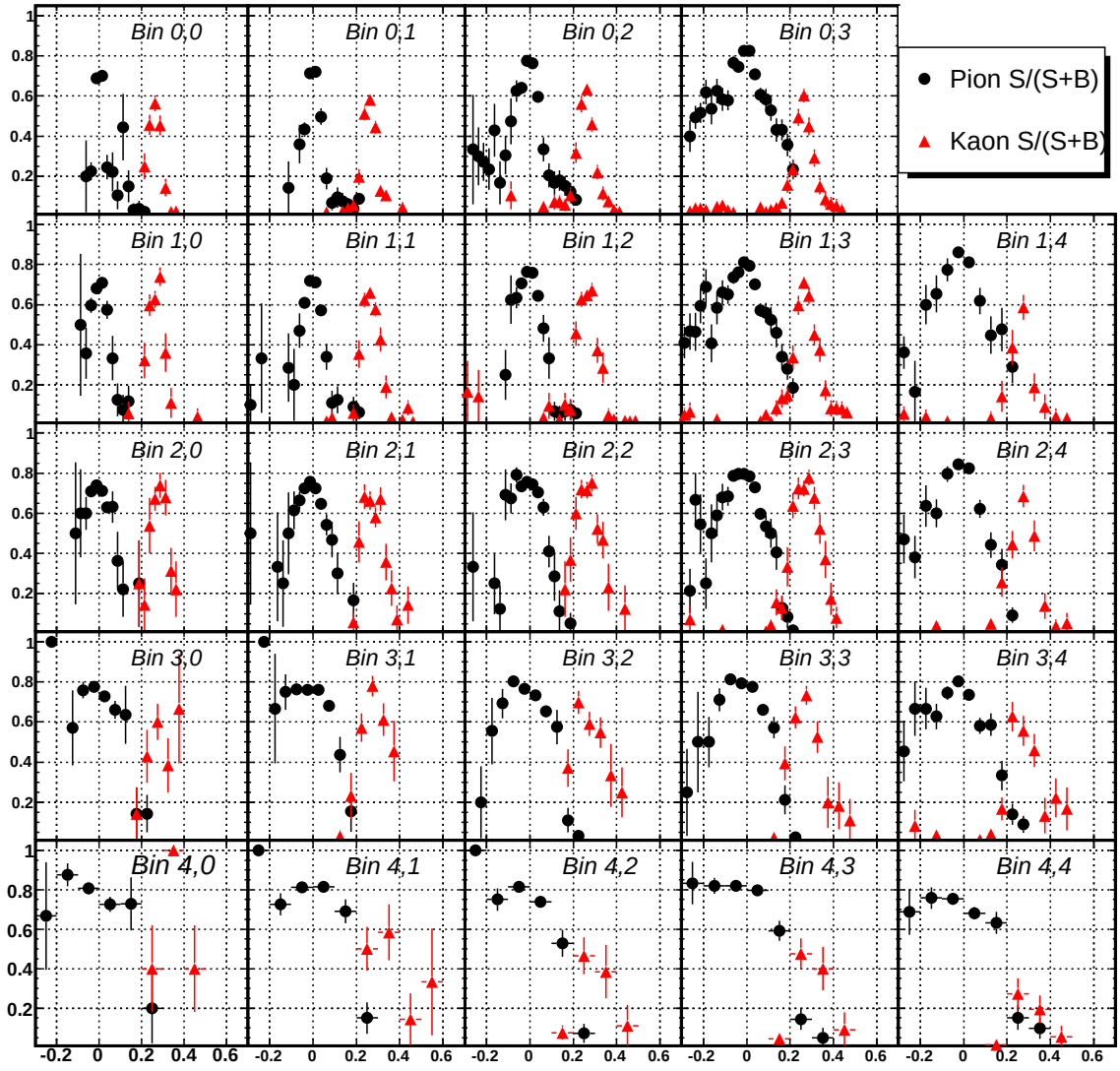

Figure 9.17: Occupancy of negative pions and kaons in Monte Carlo in the (p_z, p_t) bins.

of particles is the sum of errors in each bin added in quadrature.

Chapter 10

Results

10.1 Corrections and Errors

We can judge how well the analysis method performs by comparing ratios derived from reconstructed Monte Carlo to true ratios in each bin. Results shown in Figure 10.1 indicate that typical required corrections are less than 10%. What is somewhat surprising is that many bins in π^-/π^+ ratio require more than a 5% correction. Both particles are well identified in the RICH and do not contain significant amount of background. Corrections derived from Monte Carlo are necessary for the reasons outlined in Section 9.6.1, however given the size of π^-/π^+ correction, we will assign a 50% uncertainty on the correction in addition to the computed error on the correction.

As expected, errors associated with poor knowledge of interaction trigger efficiency are quite small with exception of the bins which have little statistics. To compute the error associated with trigger efficiency, we compute the ratios using the upper estimate of efficiency, giving each identified particle the weight equal to inverse of efficiency. We then repeat the process with the lowest estimate of efficiency and compute the quantity

$$\frac{r_\epsilon - r_0}{r_\epsilon + r_0}. \tag{10.1}$$

Here r_ϵ is the ratio measured given the assumption on trigger efficiency, and r_0 is the ratio derived using the average efficiency.

Another small error is associated with the knowledge of how much target out data should be subtracted from target in data. The results of fits of Gaussian with exponential tails (Figure 9.8) give a 2.5% uncertainty on target out subtraction. Figure 10.3 shows that

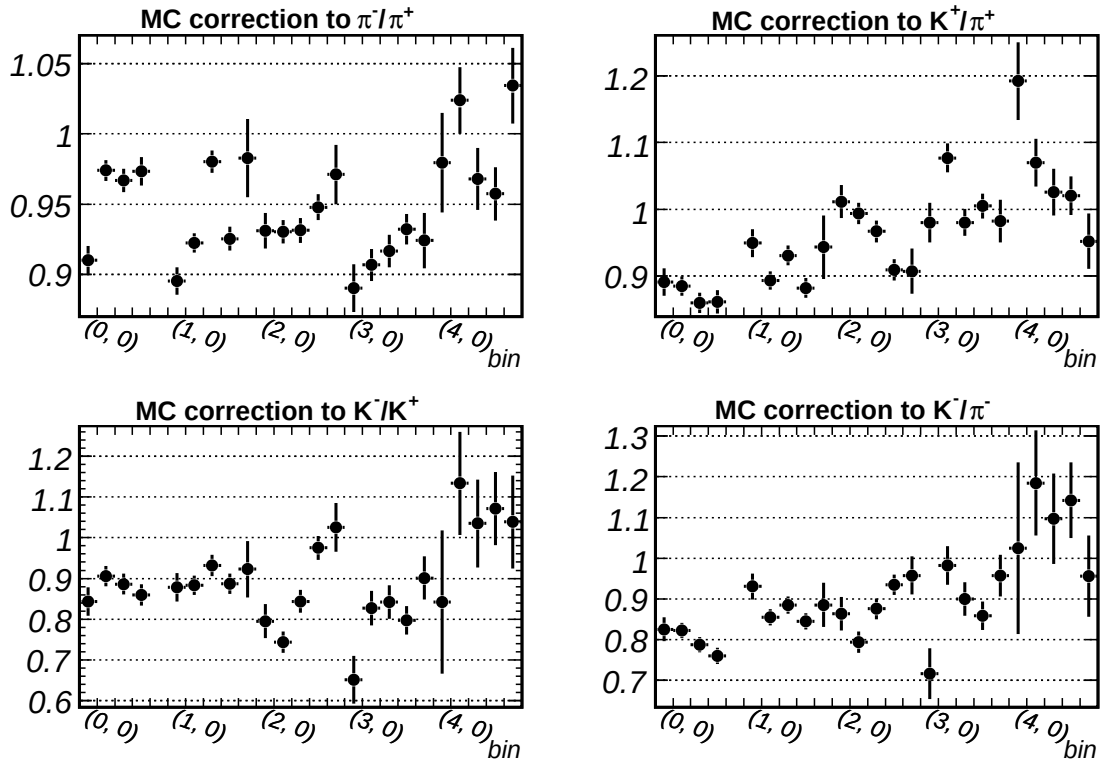

Figure 10.1: Shown are ratios of reconstructed Monte Carlo ratios and true Monte Carlo ratios. The error bars come from propagation of statistical errors on the ratios, which are correlated between the reconstructed and true ratios.

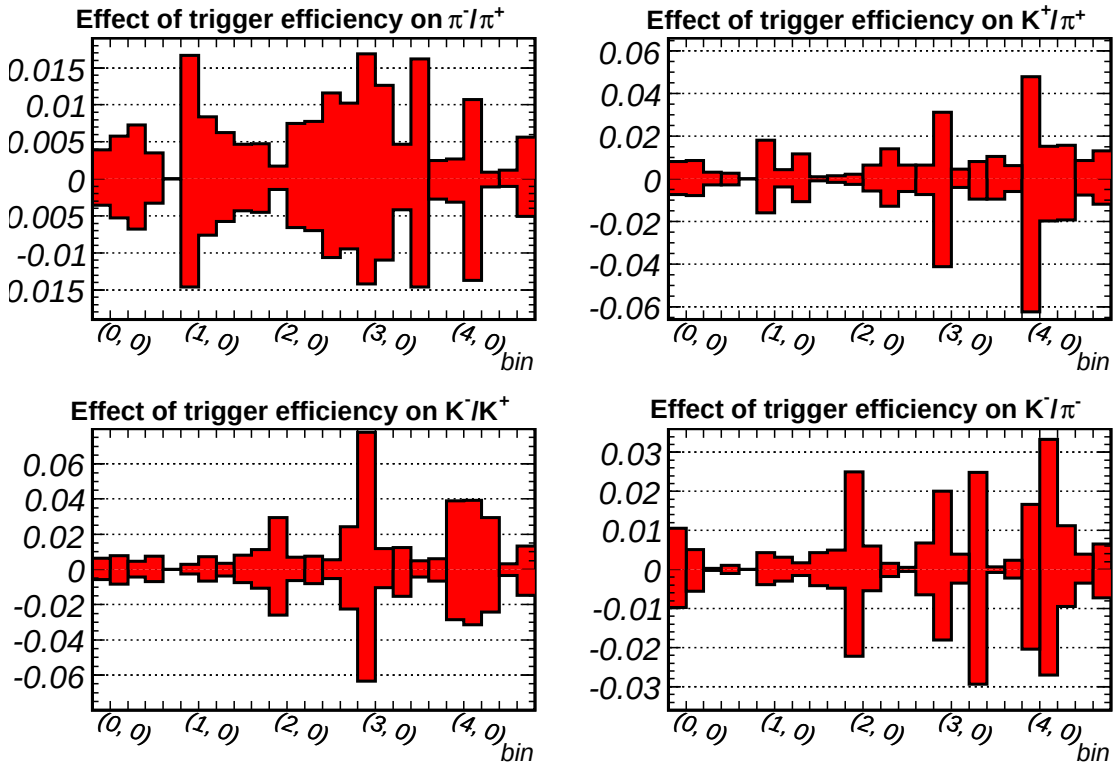

Figure 10.2: Effect of poor knowledge of interaction trigger efficiency on the ratio is quite small.

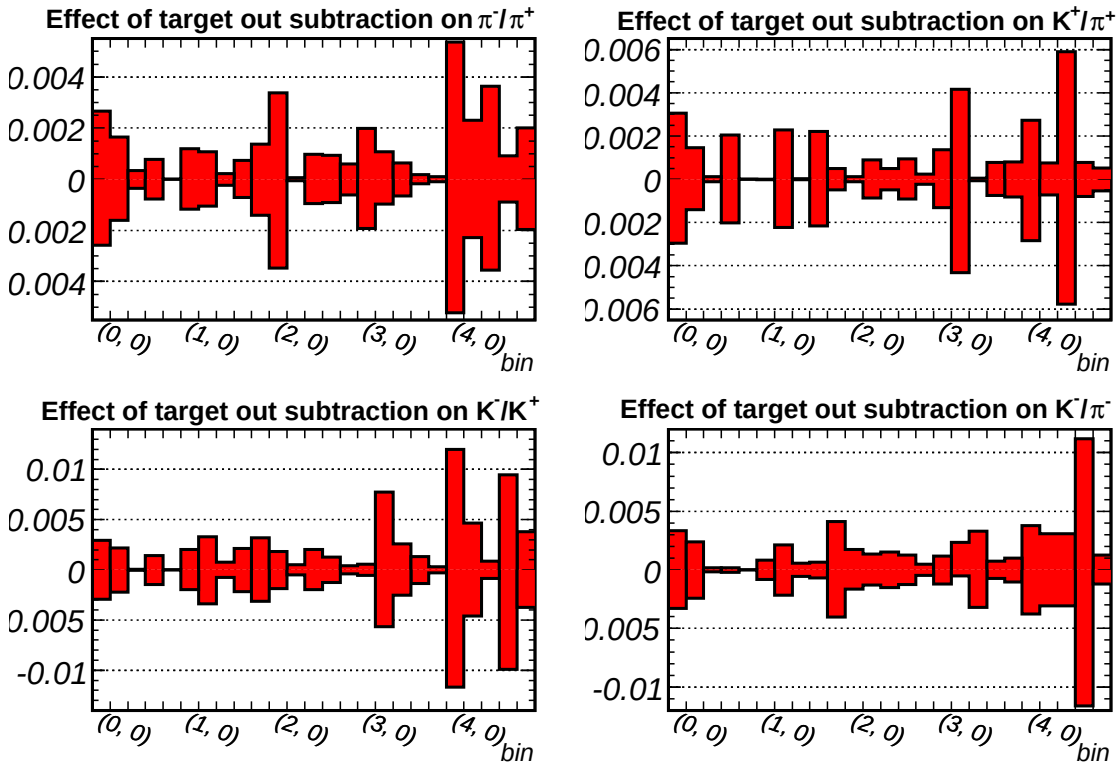

Figure 10.3: Effect on the ratio from 5% change in target out scale factor.

even if we assume a 5% uncertainty on the fraction, this affects the ratios by less than 0.5%.

The largest systematic error comes from modeling of background using the Monte Carlo. We judge the sensitivity to occupancy calculations by computing the ratios under two assumptions

1. Decreasing $(1 - o)$ in each bin where we expect to find signal by 10%;
2. Increasing $(1 - o)$ in each bin where we expect to find signal by 10%, making sure that $o > 0$.

We the plot the difference from ratios computed with nominal occupancy using Equation 10.1. Results shown in Figure 10.4 are consistent with expectations. The effect on π^-/π^+ ratio is minimal with exception of bin (3, 4) with low statistics. The effect on K^-/K^+ ratio stems in part from low statistics. By far the largest effect of background modeling is on $K^{+,-}/\pi^{+,-}$ ratios. The reason is that the level of background under the kaon peaks is significantly larger than under the pion peaks. Thus, decreasing $(1 - o)$ by

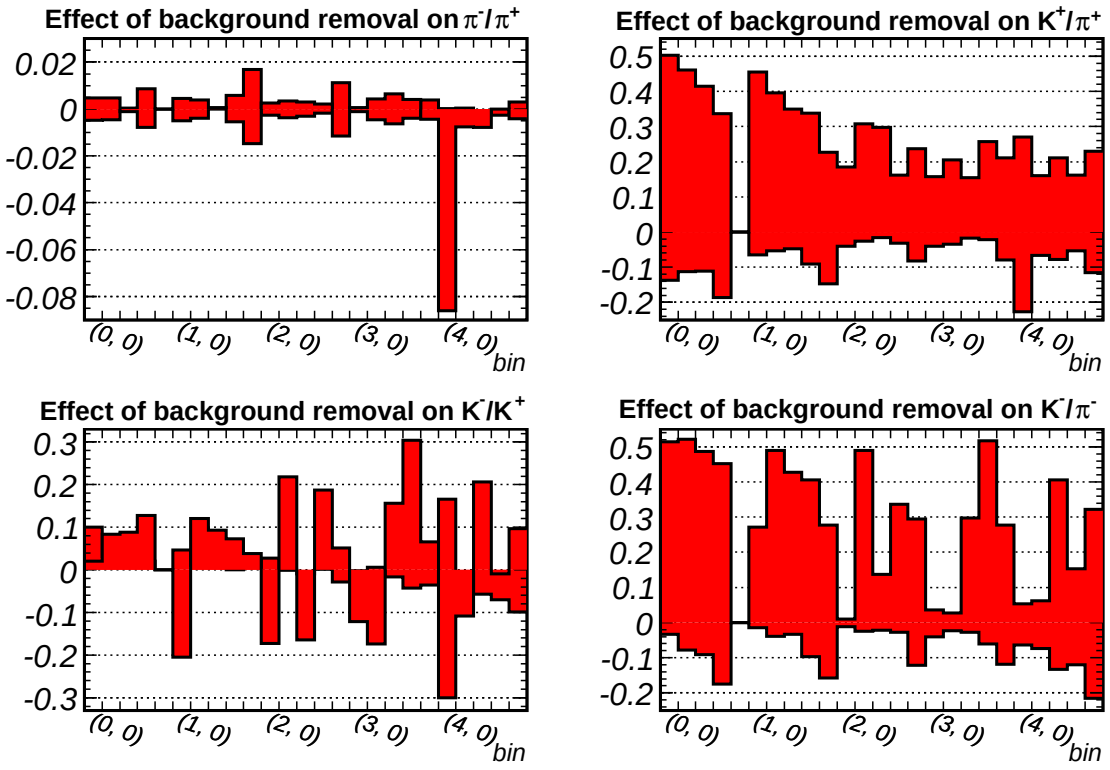

Figure 10.4: Systematic error from background subtraction. See text for explanation.

10% can boost the ratio by up to 50%.

10.2 Production Ratios

Equipped with Monte Carlo correction and errors described in the previous section, we derive the ratios which plotted in Figure 10.5 and tabulated in Tables 10.1, 10.2, 10.3, and 10.4. The ratio of like charges is mostly consistent with FLUKA-06 prediction, however the π^-/π^+ and K^-/K^+ are too high in FLUKA by as much as 50%, especially at lower momentum. From the standpoint of this measurement, it means that event topology and background in the Monte Carlo will be different from data, but is unlikely to introduce a significant bias. From the standpoint of the MINOS experiment, this is important, since anti-neutrinos are produced from decays of π^- and K^-.

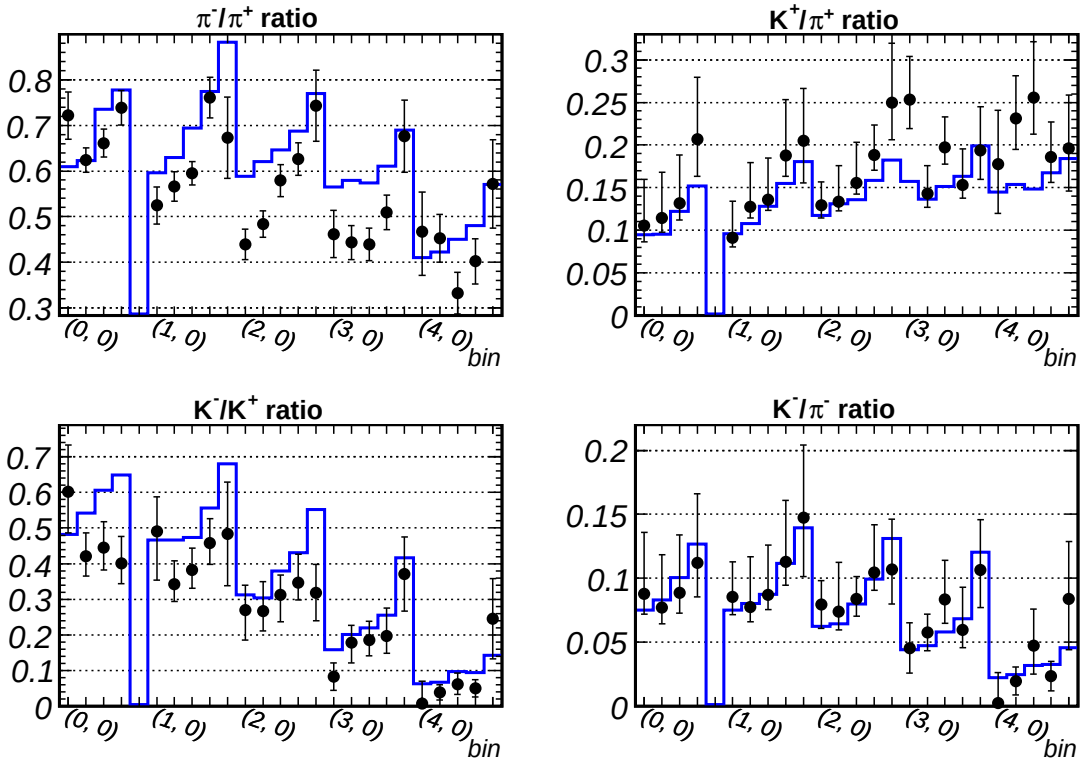

Figure 10.5: Measured ratios compared to particle production simulated with FLUKA-06 on 2% carbon target

Bin	p_z (GeV/c)	p_t (GeV/c)	π^-/π^+	Errors in percent: Statistical	Total systematic	MC Correction	Trigger efficiency	Target out subtraction	Background modeling
(0, 0)	21.9	0.13	$0.722^{+0.050}_{-0.050}$	5.2	$^{+4.7}_{-4.7}$	4.6	$^{+0.4}_{-0.4}$	$^{+0.3}_{-0.3}$	$^{+0.5}_{-0.5}$
(0, 1)	21.9	0.30	$0.624^{+0.025}_{-0.025}$	3.7	$^{+1.7}_{-1.7}$	1.5	$^{+0.6}_{-0.5}$	$^{+0.2}_{-0.2}$	$^{+0.5}_{-0.5}$
(0, 2)	21.9	0.50	$0.661^{+0.029}_{-0.029}$	3.9	$^{+2.0}_{-2.0}$	1.9	$^{+0.7}_{-0.7}$	$^{+0.0}_{-0.0}$	$^{+0.0}_{-0.1}$
(0, 3)	22.0	0.74	$0.739^{+0.035}_{-0.035}$	4.4	$^{+1.9}_{-1.9}$	1.7	$^{+0.4}_{-0.3}$	$^{+0.1}_{-0.1}$	$^{+0.9}_{-0.8}$
(1, 0)	27.1	0.13	$0.524^{+0.039}_{-0.039}$	4.9	$^{+5.6}_{-5.6}$	5.3	$^{+1.7}_{-1.5}$	$^{+0.1}_{-0.1}$	$^{+0.5}_{-0.5}$
(1, 1)	27.1	0.30	$0.566^{+0.031}_{-0.031}$	3.8	$^{+4.1}_{-4.0}$	3.9	$^{+0.8}_{-0.8}$	$^{+0.1}_{-0.1}$	$^{+0.4}_{-0.4}$
(1, 2)	27.2	0.49	$0.595^{+0.024}_{-0.024}$	3.8	$^{+1.4}_{-1.4}$	1.3	$^{+0.6}_{-0.6}$	$^{+0.0}_{-0.0}$	$^{+0.1}_{-0.0}$
(1, 3)	27.3	0.75	$0.761^{+0.043}_{-0.043}$	4.0	$^{+3.9}_{-3.9}$	3.8	$^{+0.5}_{-0.4}$	$^{+0.1}_{-0.1}$	$^{+0.6}_{-0.5}$
(1, 4)	27.5	1.08	$0.673^{+0.083}_{-0.083}$	11.8	$^{+3.5}_{-3.4}$	3.0	$^{+0.5}_{-0.4}$	$^{+0.1}_{-0.1}$	$^{+1.7}_{-1.5}$
(2, 0)	35.6	0.13	$0.439^{+0.032}_{-0.032}$	6.2	$^{+3.7}_{-3.7}$	3.7	$^{+0.2}_{-0.1}$	$^{+0.3}_{-0.3}$	$^{+0.3}_{-0.3}$
(2, 1)	35.5	0.30	$0.483^{+0.028}_{-0.028}$	4.4	$^{+3.7}_{-3.7}$	3.6	$^{+0.7}_{-0.7}$	$^{+0.0}_{-0.0}$	$^{+0.3}_{-0.4}$
(2, 2)	35.6	0.50	$0.579^{+0.033}_{-0.033}$	4.5	$^{+3.7}_{-3.6}$	3.6	$^{+0.8}_{-0.7}$	$^{+0.1}_{-0.1}$	$^{+0.3}_{-0.3}$
(2, 3)	35.6	0.76	$0.626^{+0.034}_{-0.034}$	4.5	$^{+3.0}_{-3.0}$	2.8	$^{+1.2}_{-1.1}$	$^{+0.1}_{-0.1}$	$^{+0.2}_{-0.2}$
(2, 4)	36.0	1.19	$0.743^{+0.073}_{-0.073}$	9.3	$^{+3.0}_{-3.0}$	2.6	$^{+1.0}_{-0.9}$	$^{+0.1}_{-0.1}$	$^{+1.1}_{-1.2}$
(3, 0)	48.6	0.13	$0.462^{+0.050}_{-0.050}$	8.9	$^{+6.1}_{-6.0}$	5.8	$^{+1.7}_{-1.4}$	$^{+0.2}_{-0.2}$	$^{+0.1}_{-0.1}$
(3, 1)	48.9	0.30	$0.443^{+0.036}_{-0.036}$	6.4	$^{+5.0}_{-5.0}$	4.8	$^{+1.3}_{-1.1}$	$^{+0.1}_{-0.1}$	$^{+0.4}_{-0.5}$
(3, 2)	49.2	0.50	$0.439^{+0.034}_{-0.034}$	6.5	$^{+4.4}_{-4.4}$	4.4	$^{+0.5}_{-0.4}$	$^{+0.1}_{-0.1}$	$^{+0.7}_{-0.6}$
(3, 3)	48.8	0.76	$0.509^{+0.036}_{-0.036}$	5.9	$^{+4.0}_{-3.9}$	3.6	$^{+1.6}_{-1.5}$	$^{+0.0}_{-0.0}$	$^{+0.4}_{-0.4}$
(3, 4)	49.0	1.25	$0.676^{+0.075}_{-0.075}$	10.1	$^{+4.4}_{-4.4}$	4.4	$^{+0.2}_{-0.3}$	$^{+0.0}_{-0.0}$	$^{+0.4}_{-0.4}$
(4, 0)	69.6	0.13	$0.467^{+0.082}_{-0.091}$	17.2	$^{+3.8}_{-9.4}$	3.8	$^{+0.3}_{-0.3}$	$^{+0.5}_{-0.5}$	$^{+0.0}_{-8.6}$
(4, 1)	69.1	0.30	$0.452^{+0.049}_{-0.050}$	10.5	$^{+2.8}_{-3.0}$	2.6	$^{+1.1}_{-1.4}$	$^{+0.2}_{-0.2}$	$^{+0.0}_{-0.8}$
(4, 2)	68.1	0.49	$0.332^{+0.044}_{-0.044}$	12.9	$^{+2.8}_{-2.9}$	2.8	$^{+0.1}_{-0.1}$	$^{+0.4}_{-0.4}$	$^{+0.0}_{-0.8}$
(4, 3)	68.8	0.77	$0.402^{+0.047}_{-0.047}$	11.4	$^{+2.9}_{-2.9}$	2.9	$^{+0.1}_{-0.1}$	$^{+0.1}_{-0.1}$	$^{+0.0}_{-0.3}$
(4, 4)	70.7	1.33	$0.572^{+0.092}_{-0.092}$	15.8	$^{+3.2}_{-3.2}$	3.1	$^{+0.6}_{-0.5}$	$^{+0.2}_{-0.2}$	$^{+0.3}_{-0.4}$

Table 10.1: π^-/π^+ production ratio and errors. Listed p_z and p_t are computed with π^+ spectrum.

Bin	p_z (GeV/c)	p_t (GeV/c)	K^-/K^+	Errors in percent: Statistical	Total systematic	MC Correction	Trigger efficiency	Target out subtraction	Background modeling
(0, 0)	21.9	0.13	$0.602^{+0.123}_{-0.107}$	15.5	$^{+13.4}_{-8.9}$	8.8	$^{+0.6}_{-0.6}$	$^{+0.3}_{-0.3}$	$^{+10.0}_{0.0}$
(0, 1)	21.9	0.30	$0.421^{+0.063}_{-0.052}$	11.1	$^{+10.0}_{-5.5}$	5.5	$^{+0.8}_{-0.8}$	$^{+0.2}_{-0.2}$	$^{+8.4}_{0.0}$
(0, 2)	21.9	0.50	$0.445^{+0.070}_{-0.058}$	11.4	$^{+10.9}_{-6.4}$	6.4	$^{+0.5}_{-0.4}$	$^{+0.0}_{-0.0}$	$^{+8.8}_{0.0}$
(0, 3)	22.0	0.74	$0.400^{+0.073}_{-0.052}$	10.5	$^{+14.9}_{-7.7}$	7.7	$^{+0.8}_{-0.7}$	$^{+0.1}_{-0.1}$	$^{+12.8}_{0.0}$
(1, 0)	27.1	0.13	$0.491^{+0.090}_{-0.133}$	16.2	$^{+8.6}_{-21.7}$	7.3	$^{+0.3}_{-0.3}$	$^{+0.2}_{-0.2}$	$^{+4.7}_{-20.5}$
(1, 1)	27.1	0.30	$0.343^{+0.062}_{-0.047}$	12.0	$^{+13.7}_{-6.5}$	6.4	$^{+0.7}_{-0.7}$	$^{+0.3}_{-0.3}$	$^{+12.0}_{0.0}$
(1, 2)	27.2	0.49	$0.382^{+0.059}_{-0.047}$	11.6	$^{+10.3}_{-4.4}$	4.4	$^{+0.3}_{-0.4}$	$^{+0.1}_{-0.1}$	$^{+9.3}_{0.0}$
(1, 3)	27.3	0.75	$0.458^{+0.065}_{-0.055}$	10.3	$^{+9.6}_{-6.4}$	6.3	$^{+0.8}_{-0.8}$	$^{+0.2}_{-0.2}$	$^{+7.2}_{-0.0}$
(1, 4)	27.5	1.08	$0.483^{+0.132}_{-0.130}$	25.6	$^{+9.3}_{-8.5}$	8.4	$^{+1.1}_{-1.1}$	$^{+0.3}_{-0.3}$	$^{+3.9}_{0.0}$
(2, 0)	35.6	0.13	$0.270^{+0.066}_{-0.080}$	21.2	$^{+12.2}_{-20.9}$	11.5	$^{+2.9}_{-2.6}$	$^{+0.2}_{-0.2}$	$^{+2.7}_{-17.2}$
(2, 1)	35.5	0.30	$0.267^{+0.080}_{-0.055}$	15.5	$^{+25.5}_{-13.3}$	13.3	$^{+0.7}_{-0.6}$	$^{+0.1}_{-0.1}$	$^{+21.8}_{-0.2}$
(2, 2)	35.6	0.50	$0.312^{+0.052}_{-0.073}$	14.4	$^{+8.5}_{-18.5}$	8.5	$^{+0.7}_{-0.8}$	$^{+0.2}_{-0.2}$	$^{+0.0}_{-16.4}$
(2, 3)	35.6	0.76	$0.346^{+0.078}_{-0.044}$	12.3	$^{+19.0}_{-3.3}$	3.3	$^{+0.6}_{-0.5}$	$^{+0.1}_{-0.1}$	$^{+18.7}_{0.0}$
(2, 4)	36.0	1.19	$0.318^{+0.073}_{-0.071}$	21.3	$^{+8.2}_{-7.0}$	5.9	$^{+2.4}_{-2.2}$	$^{+0.0}_{-0.0}$	$^{+5.1}_{-2.9}$
(3, 0)	48.6	0.13	$0.083^{+0.035}_{-0.037}$	37.0	$^{+21.1}_{-23.9}$	19.6	$^{+7.8}_{-6.3}$	$^{+0.1}_{-0.1}$	$^{+0.0}_{-12.1}$
(3, 1)	48.9	0.30	$0.179^{+0.045}_{-0.055}$	23.3	$^{+10.2}_{-20.1}$	10.0	$^{+1.2}_{-1.0}$	$^{+0.8}_{-0.6}$	$^{+0.6}_{-17.4}$
(3, 2)	49.2	0.50	$0.186^{+0.050}_{-0.041}$	20.0	$^{+18.2}_{-9.6}$	9.3	$^{+1.2}_{-1.5}$	$^{+0.3}_{-0.3}$	$^{+15.6}_{-1.6}$
(3, 3)	48.8	0.76	$0.197^{+0.076}_{-0.047}$	20.9	$^{+32.3}_{-11.8}$	11.0	$^{+0.5}_{-0.4}$	$^{+0.1}_{-0.1}$	$^{+30.4}_{-4.3}$
(3, 4)	49.0	1.25	$0.370^{+0.098}_{-0.096}$	24.3	$^{+10.1}_{-8.5}$	7.7	$^{+0.6}_{-0.7}$	$^{+0.0}_{-0.0}$	$^{+6.5}_{-3.6}$
(4, 0)	69.6	0.13	$0.006^{+0.063}_{-0.063}$	1000.1	$^{+28.0}_{-37.5}$	22.3	$^{+3.9}_{-2.9}$	$^{+1.2}_{-1.2}$	$^{+16.6}_{-30.0}$
(4, 1)	69.1	0.30	$0.038^{+0.019}_{-0.020}$	48.6	$^{+13.6}_{-17.2}$	13.0	$^{+3.9}_{-3.2}$	$^{+0.5}_{-0.5}$	$^{+0.0}_{-10.8}$
(4, 2)	68.1	0.49	$0.061^{+0.028}_{-0.026}$	39.8	$^{+23.4}_{-12.3}$	10.6	$^{+2.9}_{-2.4}$	$^{+0.1}_{-0.1}$	$^{+20.7}_{-5.7}$
(4, 3)	68.8	0.77	$0.050^{+0.023}_{-0.023}$	44.3	$^{+9.2}_{-11.5}$	9.1	$^{+0.3}_{-0.3}$	$^{+0.9}_{-1.0}$	$^{+0.0}_{-7.0}$
(4, 4)	70.7	1.33	$0.245^{+0.098}_{-0.098}$	37.2	$^{+14.8}_{-15.0}$	11.2	$^{+1.3}_{-1.5}$	$^{+0.4}_{-0.4}$	$^{+9.6}_{-9.9}$

Table 10.2: K^-/K^+ production ratio and errors. Listed p_z and p_t are computed using π^+ spectrum.

Bin	p_z (GeV/c)	p_t (GeV/c)	K^+/π^+	Errors in percent: Statistical	Total systematic	MC Correction	Trigger efficiency	Target out subtraction	Background modeling
(0, 0)	21.9	0.13	$0.105^{+0.054}_{-0.018}$	8.8	$^{+50.6}_{-15.0}$	5.9	$^{+0.8}_{-0.7}$	$^{+0.3}_{-0.3}$	$^{+50.2}_{-13.8}$
(0, 1)	21.9	0.30	$0.114^{+0.054}_{-0.016}$	6.1	$^{+46.5}_{-12.8}$	6.0	$^{+0.9}_{-0.8}$	$^{+0.1}_{-0.1}$	$^{+46.1}_{-11.3}$
(0, 2)	21.9	0.50	$0.132^{+0.056}_{-0.020}$	6.5	$^{+42.1}_{-13.3}$	7.3	$^{+0.3}_{-0.3}$	$^{+0.0}_{-0.0}$	$^{+41.5}_{-11.2}$
(0, 3)	22.0	0.74	$0.207^{+0.072}_{-0.043}$	6.1	$^{+34.4}_{-20.0}$	7.2	$^{+0.3}_{-0.3}$	$^{+0.2}_{-0.2}$	$^{+33.7}_{-18.6}$
(1, 0)	27.1	0.13	$0.091^{+0.042}_{-0.010}$	8.5	$^{+45.7}_{-7.6}$	3.4	$^{+1.8}_{-1.6}$	$^{+0.0}_{-0.0}$	$^{+45.5}_{-6.6}$
(1, 1)	27.1	0.30	$0.128^{+0.052}_{-0.013}$	6.1	$^{+39.9}_{-7.8}$	5.6	$^{+0.4}_{-0.4}$	$^{+0.2}_{-0.2}$	$^{+39.5}_{-5.4}$
(1, 2)	27.2	0.49	$0.136^{+0.049}_{-0.012}$	6.3	$^{+35.1}_{-6.2}$	3.8	$^{+1.2}_{-1.1}$	$^{+0.0}_{-0.0}$	$^{+34.9}_{-4.7}$
(1, 3)	27.3	0.75	$0.188^{+0.066}_{-0.024}$	6.1	$^{+34.4}_{-11.0}$	6.2	$^{+0.1}_{-0.1}$	$^{+0.2}_{-0.2}$	$^{+33.8}_{-9.2}$
(1, 4)	27.5	1.08	$0.205^{+0.058}_{-0.046}$	16.1	$^{+23.5}_{-15.8}$	5.8	$^{+0.1}_{-0.2}$	$^{+0.0}_{-0.0}$	$^{+22.7}_{-14.7}$
(2, 0)	35.6	0.13	$0.129^{+0.027}_{-0.014}$	9.5	$^{+18.6}_{-4.8}$	2.5	$^{+0.2}_{-0.3}$	$^{+0.0}_{-0.0}$	$^{+18.5}_{-4.1}$
(2, 1)	35.5	0.30	$0.133^{+0.042}_{-0.010}$	6.9	$^{+30.8}_{-3.2}$	1.6	$^{+0.6}_{-0.6}$	$^{+0.1}_{-0.1}$	$^{+30.8}_{-2.7}$
(2, 2)	35.6	0.50	$0.155^{+0.048}_{-0.012}$	7.1	$^{+29.8}_{-3.1}$	2.4	$^{+1.4}_{-1.3}$	$^{+0.1}_{-0.0}$	$^{+29.7}_{-1.6}$
(2, 3)	35.6	0.76	$0.189^{+0.034}_{-0.017}$	6.8	$^{+16.9}_{-5.9}$	4.9	$^{+0.7}_{-0.6}$	$^{+0.1}_{-0.1}$	$^{+16.1}_{-3.2}$
(2, 4)	36.0	1.19	$0.249^{+0.068}_{-0.040}$	12.4	$^{+24.4}_{-10.2}$	6.0	$^{+0.7}_{-0.7}$	$^{+0.0}_{-0.0}$	$^{+23.7}_{-8.2}$
(3, 0)	48.6	0.13	$0.253^{+0.049}_{-0.031}$	10.4	$^{+16.3}_{-6.6}$	3.2	$^{+3.1}_{-4.1}$	$^{+0.1}_{-0.1}$	$^{+15.7}_{-4.0}$
(3, 1)	48.9	0.30	$0.143^{+0.032}_{-0.015}$	8.7	$^{+20.9}_{-5.5}$	4.3	$^{+0.5}_{-0.4}$	$^{+0.4}_{-0.4}$	$^{+20.5}_{-3.4}$
(3, 2)	49.2	0.50	$0.197^{+0.035}_{-0.018}$	8.5	$^{+15.6}_{-3.0}$	2.3	$^{+0.8}_{-1.0}$	$^{+0.0}_{-0.0}$	$^{+15.4}_{-1.8}$
(3, 3)	48.8	0.76	$0.153^{+0.042}_{-0.015}$	9.0	$^{+25.9}_{-3.1}$	1.9	$^{+1.1}_{-0.9}$	$^{+0.1}_{-0.1}$	$^{+25.8}_{-2.2}$
(3, 4)	49.0	1.25	$0.194^{+0.050}_{-0.032}$	14.0	$^{+21.4}_{-8.6}$	3.4	$^{+0.6}_{-0.6}$	$^{+0.1}_{-0.1}$	$^{+21.1}_{-7.9}$
(4, 0)	69.6	0.13	$0.178^{+0.061}_{-0.056}$	17.9	$^{+29.5}_{-25.9}$	10.8	$^{+4.8}_{-6.2}$	$^{+0.3}_{-0.3}$	$^{+27.0}_{-22.7}$
(4, 1)	69.1	0.30	$0.231^{+0.048}_{-0.034}$	11.9	$^{+16.9}_{-8.5}$	4.8	$^{+1.5}_{-2.0}$	$^{+0.1}_{-0.1}$	$^{+16.1}_{-6.7}$
(4, 2)	68.1	0.49	$0.256^{+0.064}_{-0.040}$	12.9	$^{+21.4}_{-8.9}$	3.6	$^{+1.6}_{-1.9}$	$^{+0.6}_{-0.6}$	$^{+21.0}_{-7.8}$
(4, 3)	68.8	0.77	$0.186^{+0.040}_{-0.028}$	13.8	$^{+16.5}_{-6.2}$	3.0	$^{+0.9}_{-0.8}$	$^{+0.1}_{-0.1}$	$^{+16.2}_{-5.3}$
(4, 4)	70.7	1.33	$0.196^{+0.061}_{-0.047}$	20.2	$^{+23.5}_{-12.7}$	5.0	$^{+1.3}_{-1.2}$	$^{+0.1}_{-0.1}$	$^{+23.0}_{-11.6}$

Table 10.3: K^+/π^+ production ratio and errors. Listed p_z and p_t are computed with π^+ spectrum.

Bin	p_z (GeV/c)	p_t (GeV/c)	K^-/π^-	Errors in percent: Statistical	Total systematic	MC Correction	Trigger efficiency	Target out subtraction	Background modeling
(0, 0)	21.9	0.13	$0.088^{+0.048}_{-0.015}$	13.7	$^{+52.3}_{-10.1}$	9.4	$^{+1.1}_{-1.0}$	$^{+0.3}_{-0.3}$	$^{+51.4}_{-3.4}$
(0, 1)	21.9	0.30	$0.077^{+0.041}_{-0.012}$	10.1	$^{+52.9}_{-12.0}$	9.2	$^{+0.5}_{-0.6}$	$^{+0.2}_{-0.2}$	$^{+52.1}_{-7.8}$
(0, 2)	21.9	0.50	$0.089^{+0.045}_{-0.016}$	10.2	$^{+49.8}_{-14.2}$	10.9	$^{+0.0}_{-0.0}$	$^{+0.0}_{-0.0}$	$^{+48.6}_{-9.2}$
(0, 3)	22.0	0.74	$0.112^{+0.054}_{-0.026}$	9.6	$^{+46.8}_{-21.3}$	12.3	$^{+0.1}_{-0.1}$	$^{+0.0}_{-0.0}$	$^{+45.2}_{-17.5}$
(1, 0)	27.1	0.13	$0.086^{+0.027}_{-0.013}$	14.6	$^{+27.6}_{-5.1}$	4.9	$^{+0.4}_{-0.4}$	$^{+0.1}_{-0.1}$	$^{+27.2}_{-1.4}$
(1, 1)	27.1	0.30	$0.077^{+0.039}_{-0.011}$	11.0	$^{+49.5}_{-8.6}$	7.6	$^{+0.3}_{-0.3}$	$^{+0.2}_{-0.2}$	$^{+48.9}_{-4.0}$
(1, 2)	27.2	0.49	$0.087^{+0.039}_{-0.011}$	10.5	$^{+43.2}_{-7.0}$	6.2	$^{+0.2}_{-0.2}$	$^{+0.1}_{-0.1}$	$^{+42.8}_{-3.3}$
(1, 3)	27.3	0.75	$0.113^{+0.048}_{-0.018}$	9.2	$^{+41.4}_{-12.7}$	8.1	$^{+0.4}_{-0.4}$	$^{+0.1}_{-0.1}$	$^{+40.5}_{-9.8}$
(1, 4)	27.5	1.08	$0.147^{+0.055}_{-0.043}$	23.1	$^{+29.0}_{-17.9}$	8.4	$^{+0.5}_{-0.5}$	$^{+0.4}_{-0.4}$	$^{+27.8}_{-15.7}$
(2, 0)	35.6	0.13	$0.079^{+0.017}_{-0.017}$	20.0	$^{+8.8}_{-8.7}$	8.3	$^{+2.5}_{-2.2}$	$^{+0.2}_{-0.2}$	$^{+1.0}_{-1.1}$
(2, 1)	35.5	0.30	$0.074^{+0.039}_{-0.013}$	14.5	$^{+50.2}_{-11.1}$	10.8	$^{+0.6}_{-0.5}$	$^{+0.1}_{-0.1}$	$^{+49.0}_{-2.4}$
(2, 2)	35.6	0.50	$0.084^{+0.017}_{-0.013}$	13.3	$^{+15.3}_{-7.2}$	6.9	$^{+0.2}_{-0.2}$	$^{+0.2}_{-0.2}$	$^{+13.7}_{-2.2}$
(2, 3)	35.6	0.76	$0.104^{+0.037}_{-0.013}$	11.2	$^{+33.9}_{-5.1}$	4.2	$^{+0.1}_{-0.1}$	$^{+0.1}_{-0.1}$	$^{+33.6}_{-2.8}$
(2, 4)	36.0	1.19	$0.107^{+0.038}_{-0.025}$	19.7	$^{+30.0}_{-13.3}$	5.4	$^{+0.7}_{-0.6}$	$^{+0.0}_{-0.0}$	$^{+29.5}_{-12.2}$
(3, 0)	48.6	0.13	$0.045^{+0.018}_{-0.018}$	36.6	$^{+17.1}_{-17.2}$	16.6	$^{+2.0}_{-1.8}$	$^{+0.1}_{-0.1}$	$^{+3.5}_{-4.1}$
(3, 1)	48.9	0.30	$0.058^{+0.013}_{-0.013}$	22.5	$^{+5.6}_{-5.4}$	4.9	$^{+0.4}_{-0.3}$	$^{+0.2}_{-0.1}$	$^{+2.7}_{-2.3}$
(3, 2)	49.2	0.50	$0.083^{+0.030}_{-0.017}$	19.2	$^{+30.6}_{-7.9}$	6.8	$^{+2.5}_{-2.9}$	$^{+0.3}_{-0.3}$	$^{+29.7}_{-2.8}$
(3, 3)	48.8	0.76	$0.059^{+0.033}_{-0.013}$	19.8	$^{+52.4}_{-10.2}$	8.1	$^{+0.1}_{-0.1}$	$^{+0.1}_{-0.1}$	$^{+51.8}_{-6.1}$
(3, 4)	49.0	1.25	$0.106^{+0.038}_{-0.028}$	22.3	$^{+28.3}_{-13.2}$	5.7	$^{+0.2}_{-0.2}$	$^{+0.1}_{-0.1}$	$^{+27.7}_{-11.9}$
(4, 0)	69.6	0.13	$0.002^{+0.024}_{-0.024}$	1000.1	$^{+21.4}_{-21.7}$	20.6	$^{+1.7}_{-2.0}$	$^{+0.4}_{-0.4}$	$^{+5.4}_{-6.4}$
(4, 1)	69.1	0.30	$0.020^{+0.010}_{-0.010}$	48.3	$^{+15.9}_{-16.3}$	14.3	$^{+3.3}_{-2.7}$	$^{+0.3}_{-0.3}$	$^{+6.1}_{-7.4}$
(4, 2)	68.1	0.49	$0.047^{+0.027}_{-0.021}$	39.8	$^{+42.2}_{-17.5}$	11.2	$^{+1.1}_{-1.0}$	$^{+0.3}_{-0.3}$	$^{+40.6}_{-13.4}$
(4, 3)	68.8	0.77	$0.023^{+0.011}_{-0.011}$	43.6	$^{+18.8}_{-16.2}$	10.8	$^{+0.4}_{-0.3}$	$^{+1.1}_{-1.2}$	$^{+15.3}_{-12.0}$
(4, 4)	70.7	1.33	$0.084^{+0.041}_{-0.036}$	35.0	$^{+34.0}_{-24.0}$	10.6	$^{+0.6}_{-0.7}$	$^{+0.1}_{-0.1}$	$^{+32.2}_{-21.5}$

Table 10.4: K^-/π^- production ratio and errors. Listed p_z and p_t are computed with π^+ spectrum.

10.3 Comparison to Existing Data

Results presented here compare well with the existing data sets. The π^-/π^+ ratio in our highest momentum bin is significantly higher than the other data. At this time, the reason for this discrepancy is not known.

It is also interesting to compare our data to BMPT parametrization of 400 GeV/c protons on beryllium target[4]. Despite the fact that proton momentum is much higher, the parametrization does a good job describing behavior of ratios. The only exception is that in the parametrization π^-/π^+ ratio is independent of p_T. This measurement and the ratio from NA49 indicates that this is not exactly so in the highest p_T bin, which is not surprising as the model was derived using data with $p_T \leq 0.5$ GeV/c .

10.4 Discussion and Outlook

We presented the first measurement using the data from the MIPP spectrometer. Precision of the measurement is generally limited by statistics, although at this time our understanding of the background under the kaon peak is limited and is a significant source of systematic error. Better understanding of the Monte Carlo coupled with better data – Monte Carlo agreement will certainly reduce the systematic errors associated with the measurement.

The measurement is consistent with previously published data, but not all of the ratios are consistent with FLUKA-06 Monte Carlo. This is important to know for calculation of neutrino fluxes in MINOS, especially so for anti-neutrino fluxes.

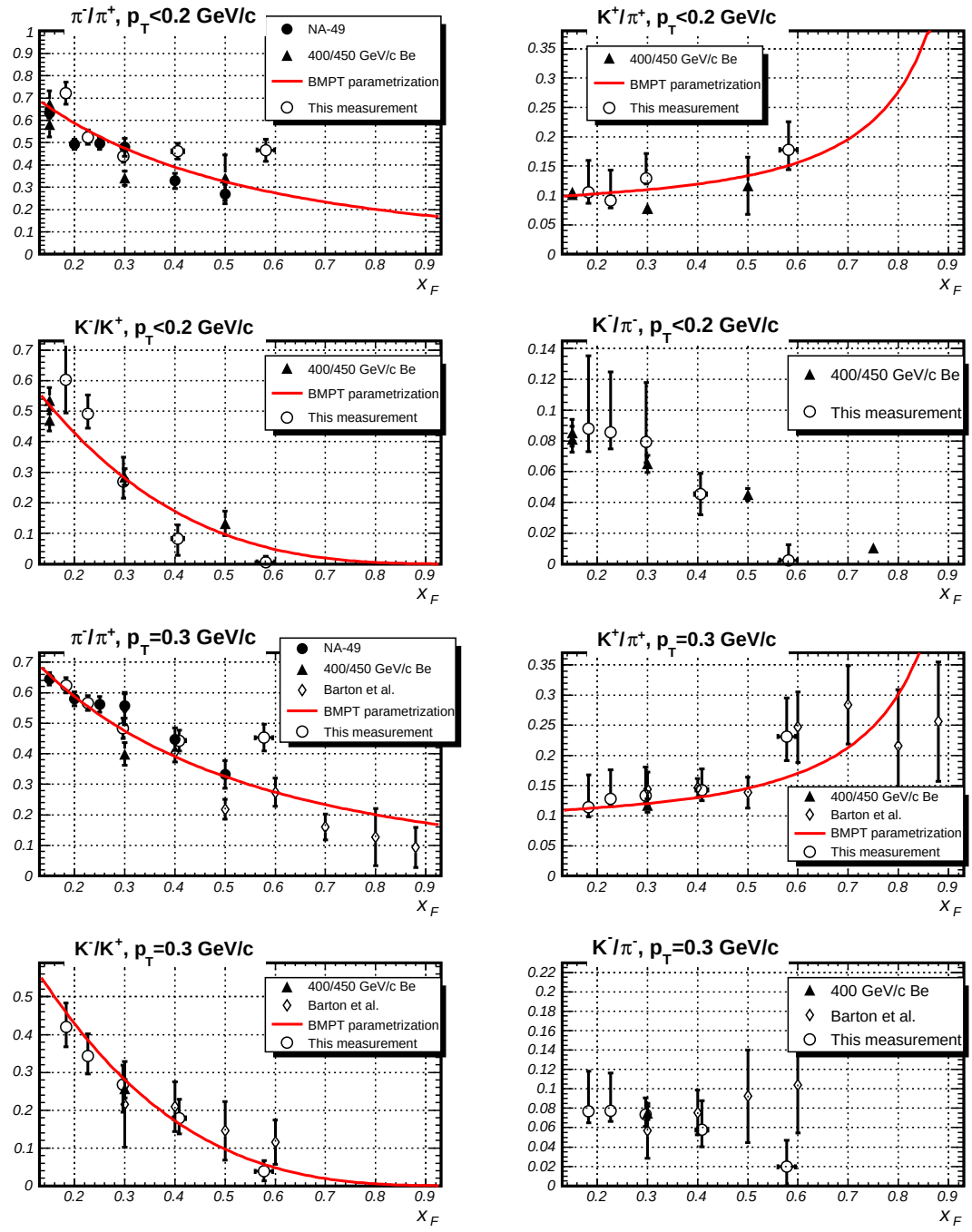

Figure 10.6: Comparison to existing measurements and parametrization of beryllium data.

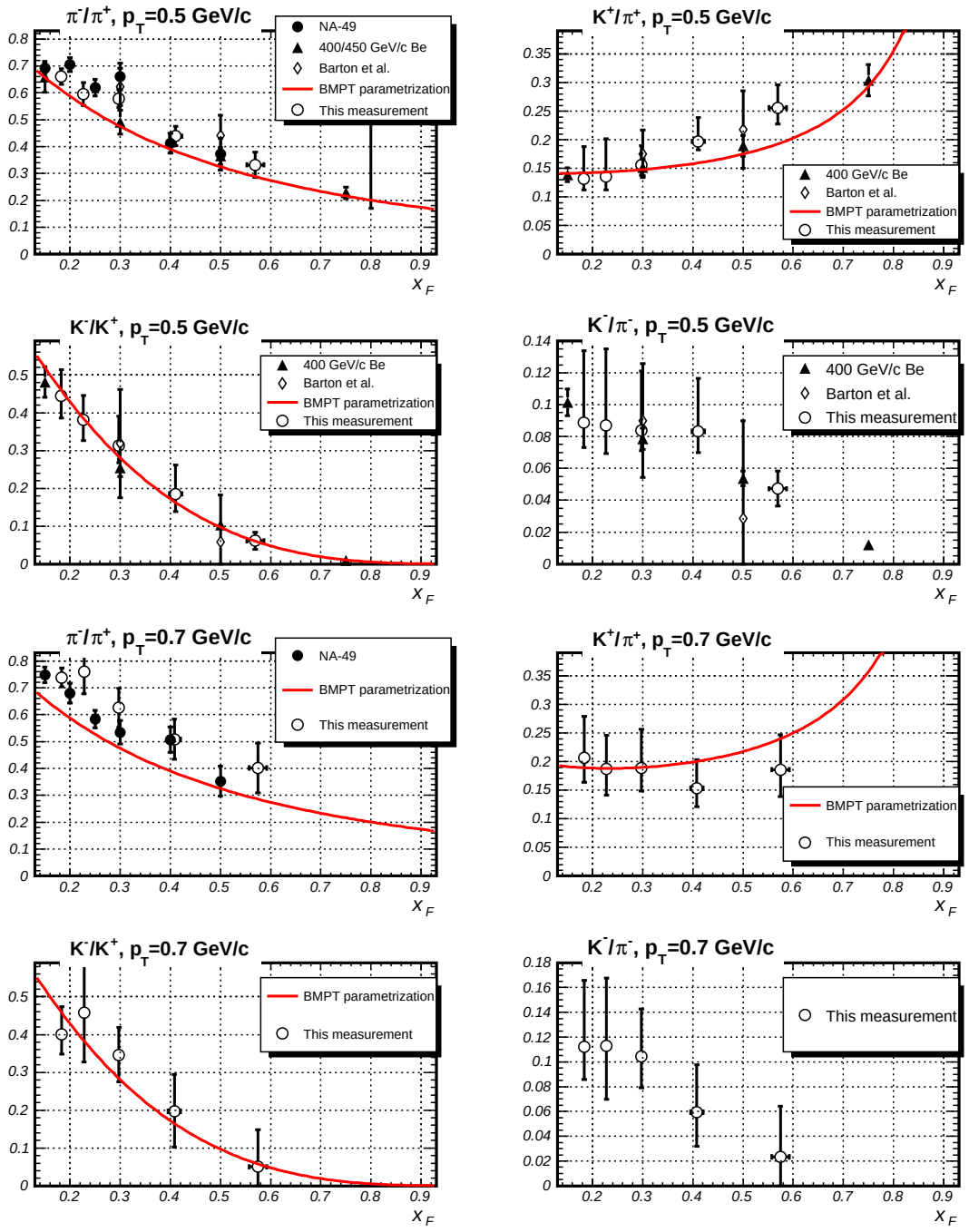

Figure 10.7: Comparison to existing measurements and parametrization of beryllium data.

Bibliography

[1] D. S. Barton et al. Experimental study of the A-dependence of inclusive hadron fragmentation. *Phys. Rev.*, D27:2580–2599, 1983.

[2] Gerard Beekmans. *Linux From Scratch Version 4.0-RC1.* Linux From Scratch Project, 2002.

[3] Fred Bieser, Ron Jones, , and Charles McFarland. Data links for the EOS TPC. *IEEE Trans. Nucl. Sc.*, **38**:335–336, 1991.

[4] M. Bonesini, A. Marchionni, F. Pietropaolo, and T.Tabarelli de Fatis. On particle production for high energy neutrino beams. *Eur.Phys.J.*, C20:13–27, 2001.

[5] C. Bower, N.Graf, M. D. Messier, and J. Paley. The Indiana trigger counter. *MIPP Note*, **55**, 2005.

[6] CERN, Geneva, Switzerland. *GEANT – Detector Description and Simulation Tool*, 1993.

[7] SPY Collaboration. *Eur. Phys. J. C*, 10:605, 1999.

[8] Creative Electronic Systems S.A. *CBD 8210 CAMAC Branch Driver*, July 1996.

[9] M. de Palma et al. A system of large multiwire proportional chambers for a high intensity experiment. *Nucl. Inst. and Meth.*, **216**:393–397, 1983.

[10] W.N. English and G.C. Hanna. *Canadian Journal of Physics*, 31:768, 1953.

[11] C. Alt et al. Inclusive production of charged pions in p+C collisions at 158GeV/c beam momentum. *arXiv:hep-ex/0606028*, 2006.

[12] D. G. Michael et al. Observation of muon neutrino disappearance with the MINOS detector in the NuMI neutrino beam. *Phys. Rev. Lett.*, 97, 2006.

[13] D.C. Christian et al. High rate drift chambers. *Nucl. Inst. and Meth.*, **A345**:62–71, 1994.

[14] G. Rai et al. A TPC detector for the study of high multiplicity heavy ion collisions. *IEEE Trans. Nucl. Sc.*, **37**:56–64, 1990.

[15] H. Wieman et al. A TPC detector for the study of high multiplicity heavy ion collisions. *Nucl. Phys.*, **A525**:617–620, 1991.

[16] H.W.Atherton et al. Technical Report 80-07, CERN Yellow Report, 1980.

[17] J. Engelfried et al. The E781 (SELEX) RICH detector). *Nucl. Inst. and Meth.*, **A409**:439–442, 1998.

[18] J. Engelfried et al. The RICH detector of the SELEX experiment. *Nucl. Inst. and Meth.*, **A433**:149–152, 1999.

[19] J. Engelfried et al. The SELEX phototube RICH detector. *Nucl. Inst. and Meth.*, **A431**:53–69, 1999.

[20] K. L. Lee et al. Analog-to-digital conversion using custom CMOS analog memory for the EOS time projection chamber. *IEEE Trans. Nucl. Sc.*, **38**:344–347, 1991.

[21] M.G.Catanesi et al. Proposal for hadron production measurements using the na49 detector for use in long-baseline and atmospheric neutrino flux calculations. CERN-SPSC-P-322, 2001.

[22] A. Fasso', A. Ferrari, J. Ranft, and P.R. Sala. Fluka: a multi-particle transport code. *CERN 2005-10, INFN/TC_05/11, SLAC-R-773*, 2005.

[23] A. Fasso', A. Ferrari, S. Roesler, P.R. Sala, G. Battistoni, F. Cerutti, E. Gadioli, M.V. Garzelli, F. Ballarini, A. Ottolenghi, A. Empl, and J. Ranft. The physics models of fluka: status and recent developments. *Computing in High Energy and Nuclear Physics Conference*, 2003.

[24] http://www.linuxfromscratch.org.

[25] Stuart A. Kleinfelder. A 4096 cell switched capacitor analog waveform storage integrated circuit. *IEEE Trans. Nucl. Sc.*, **37**:1230–1236, 1990.

[26] A. Lebedev. Chamber tuning and alignment. *MIPP Note*, 129, 2007.

[27] Valeri Lebedev. http://fnal.gov/optim.

[28] J. B. Lindsay, C. Millerin, J. C. Tarlé, H. Verveij, and H. Wendler. A fast and flexible data acquisition system for multiwire proportional chambers and other detectors. *Nucl. Inst. and Meth.*, **156**:329–333, 1978.

[29] MINERνA Collaboration. The MINERνA technical design report, 2006.

[30] N. Mokhov. MARS code system. http://www-ap.fnal.gov/MARS/.

[31] M. Nakamura, D.A. Landis, and G. Rai. Low power shaper amplifier for the EOS TPC detector. *IEEE Trans. Nucl. Sc.*, **38**:50–52, 1991.

[32] J. Paley, R. Soltz, P.D. Barnes, M. Heffner, J. Klay, and D. Miller. MIPP TPC reconstruction. *MIPP Note*, 129, 2006.

[33] Anna Peisert and Fabio Sauli. Drift and diffusion of electrons in gases: a compilation. Technical Report 84-08, CERN, July 1984.

[34] S.F.Biagi. Magboltz 2. http://ref.web.cern.ch/ref/CERN/CNL/2000/001/magboltz.

[35] S.F.Biagi. Monte Carlo simulation of electron drift and diffusion in counting gases under the influence of electric and magnetic fields. *Nucl. Inst. and Meth.*, A421:234–240, 199.

[36] Ron Soltz. Private communication.

[37] M. Staric and P. Krizan. An iterative method for the analysis of Cherenkov rings in the HERA-B RICH. *Nucl. Inst. and Meth.*, A 433:279–285, 1999.

[38] H. Wieman and the EOS Collaboration. Heavy ion reaction measurements with the EOS TPC (looking for central collisions with missing energy). In *Proceedings of the Tenth Winter Workshop on Nuclear Dynamics (Snowbird, Utah)*, January 14-21, 1994.

[39] Xihong Yang. *Centrality dependence of strangeness production in proton-nucleus collisions at AGS energies*. PhD thesis, Columbia University, 2000.